Structurally compatible embedded sensors for damage detection in glass fibre reinforced polymers

Vom Promotionsausschuss der
Technischen Universität Hamburg
zur Erlangung des akademischen Grades
Doktor-Ingenieurin (Dr.-Ing.)

genehmigte Dissertation

von
Christina Dorothea Buggisch

aus
Kiel, Deutschland

2022

Vorsitzender des Prüfungsausschusses:	Prof. Dr.-Ing. Benedikt Kriegesmann (Technische Universität Hamburg)
Gutachter:	Prof. Dr.-Ing. habil. Bodo Fiedler (Technische Universität Hamburg) Prof. Dr.-Ing. habil. Raimund Rolfes (Leibniz Universität Hannover)
Tag der mündlichen Prüfung:	13.07.2022

Technisch-Wissenschaftliche Schriftenreihe

Herausgeber:
Prof. Dr.-Ing. habil. Bodo Fiedler

Anschrift:
Technische Universität Hamburg
Institut für Kunststoffe und Verbundwerkstoffe
Denickestraße 15
21073 Hamburg

Band 42:
Structurally compatible embedded sensors for damage detection in glass fibre reinforced polymers
DOI: https://doi.org/10.15480/882.4557

Christina Dorothea Buggisch
https://orcid.org/0000-0002-8647-8923

1. Auflage
Hamburg 2022

ISSN 2625-6029

Bibliographische Information der Deutschen Nationalbibliothek:
Die deutsche Nationalbibliothek verzeichnet diese Publikation in der Deutschen Nationalbibliothek; detaillierte Informationen sind im Internet über dnb.de abrufbar.

Abstract

High-performance glass fibre reinforced polymer (GFRP) composites are used in numerous applications where a safe and reliable operation is crucial. However, composites exhibit a complex failure behaviour due to their multi-scale nature. Occurring damages often cannot be detected by visual inspection but severely influence the material performance.
Consequently, different in-situ structural health monitoring (SHM) methods have been developed to detect and evaluate damages and assure material integrity during operation. Many SHM methods require complex sensor networks, expensive measuring equipment and skilled personnel.
The electrical conductivity of carbon fibre reinforced polymers enables in-situ resistance measurements and allows monitoring of the material state during operation without additional sensor networks. However, such self-sensing, resistive SHM is not possible in unmodified GFRP composites like wind turbine rotor blades due to the lack of electrical conductivity. Resistive SHM of polymers or GFRPs can be achieved by modifying the matrix using conductive nanoparticles [1–4]. However, particularly for large structures, a modification of the entire matrix is expensive. Research on reliable, material-conform electrical SHM of GFRP composites is still limited. Therefore, the research hypothesis of this thesis is:

Real-time damage detection and evaluation of GFRP structures can be achieved using in-situ electrical measurements.

Two approaches of local, conductive, material-conform modification of GFRPs for electrical SHM are developed and presented. The first method describes a local matrix modification with fully-integrated pre-cured carbon nanotube (CNT)/epoxy thin-film sensors. The second technique outlines a local modification with conductive fibres as conductors for capacitance measurements.

The fully-integrated CNT/epoxy thin-film sensors enable strain and damage monitoring over large material sections or selectively in highly loaded areas without significantly influencing the mechanical performance of the parts. The in-situ resistance changes can reproducibly be correlated with the strains inside the material due to the CNT sensors' piezoresistive effect. Tensile stresses result in a resistance increase and compressive stresses in a resistance decrease. Remaining local strains due to damages like matrix cracks result in irreversibility of the resistance change during unloading. A suitable sensor design enables high sensitivities. First durability studies proved the integrity of the sensors during cyclic fatigue tests. Furthermore, critical buckling can be reliably detected, as it was proven during crippling tests on stringers.

Capacitance measurements on integrated carbon fibre (CF) bundles allow in-situ damage monitoring in GFRPs due to damage-induced material permittivity changes. Developing damages like matrix cracks and delaminations increase the amount of enclosed air which causes an overall lower permittivity and thus a drop in capacitance. Matrix crack evolution and capacitance decrease clearly correlate during tensile tests on cross-ply specimens. An analytical model allows the determination of matrix crack number from the measured capacitance change and therefore an in-situ evaluation of damage state. The CF bundles' distance influences the sensitivity of the measurements, and integration of the CF bundles in differently oriented laminate layers enables monitoring of the entire composite's failure process. In addition, a detection and size estimation of impact damages is demonstrated.

Both presented methods allow for user-friendly, real-time, in-situ SHM without significantly influencing the mechanical material properties. The sensor production and integration can be implemented into existing industrial manufacturing processes without major additional effort. A suitable, tailored sensor design allows for timely damage detection and an in-depth understanding of the composite's failure process. Therefore, this work contributes to a safer and more efficient use of lightweight GFRP composites.

Kurzfassung

Hochleistungs-Glasfaserverstärkte Kunststoffe (GFK) werden in zahlreichen Anwendungen eingesetzt, bei denen ein sicherer und zuverlässiger Betrieb unabdingbar ist. Aufgrund ihres multiskaligen Aufbaus weisen Verbundwerkstoffe jedoch ein komplexes Versagensverhalten auf. Auftretende Schäden können oft nicht durch eine visuelle Inspektion erkannt werden, beeinflussen aber die Leistungsfähigkeit des Materials erheblich.
Daher wurden verschiedene Methoden zur In-situ-Zustandsüberwachung (engl.: structural health monitoring (SHM)) entwickelt, um Schäden während des Betriebs zu erkennen und zu bewerten sowie die Materialintegrität während der gesamten Lebensdauer zu gewährleisten. Viele SHM-Methoden erfordern komplexe Sensornetzwerke, teure Messgeräte und qualifiziertes Personal.
Die elektrische Leitfähigkeit von kohlenstofffaserverstärkten Polymeren ermöglicht In-situ-Widerstandsmessungen und erlaubt die Überwachung des Materialzustands während des Betriebs ohne zusätzliche Sensornetzwerke. In unmodifizierten GFK-Verbundwerkstoffen, wie z. B. Rotorblättern von Windkraftanlagen, ist jedoch aufgrund der mangelnden elektrischen Leitfähigkeit des Materials ein solches sensorfreies, widerstandsbasiertes SHM nicht möglich. Widerstandsbasiertes SHM von Polymeren oder GFK kann durch eine Modifikation der Matrix mit leitfähigen Nanopartikeln erreicht werden [1–4]. Insbesondere bei großen Strukturen ist eine Modifikation der gesamten Matrix teuer. Die Forschung zum zuverlässigen und materialgerechten elektrischen SHM von GFK-Verbundwerkstoffen ist noch begrenzt. Die Forschungshypothese dieser Arbeit lautet daher:

Eine Echtzeit-Schadenserkennung und -bewertung von GFK-Strukturen kann durch elektrische In-situ-Messungen erreicht werden.

Es werden zwei Ansätze zur lokalen, leitfähigen, materialkonformen Modifikation von GFK für elektrisches SHM vorgestellt. Die erste Methode beschreibt eine

lokale Matrixmodifikation mit vollständig integrierten, vorausgehärteten Kohlenstoffnanoröhren (engl.: carbon nanotubes (CNTs))/Epoxidharz-Dünnschichtsensoren. Das zweite Verfahren skizziert eine lokale Modifikation mit leitfähigen Fasern als Elektroden für Kapazitätsmessungen.

Die vollintegrierten CNT/Epoxidharz-Dünnschichtsensoren ermöglichen die Überwachung von Dehnungen und Schädigungen über große Materialabschnitte oder selektiv in hochbelasteten Bereichen, ohne wesentlichen Einfluss auf die mechanischen Eigenschaften. Durch den piezoresistiven Effekt der CNT-Sensoren können die In-situ-Widerstandsänderungen reproduzierbar mit den Dehnungen im Material korreliert werden. Zugspannungen führen zu einer Widerstandserhöhung und Druckspannungen zu einer Widerstandsabnahme. Verbleibende lokale Dehnungen aufgrund von Beschädigungen wie Zwischenfaserbrüchen führen zu einer irreversiblen Änderung des Widerstands bei Entlastung. Ein geeignetes Sensordesign ermöglicht hohe Empfindlichkeiten. Erste Beständigkeitsstudien haben die Integrität der Sensoren bei zyklischen Ermüdungstests nachgewiesen. Kritisches Beulen kann bei Druckversuchen an Stringern zuverlässig erkannt werden.

Kapazitätsmessungen an integrierten Kohlenstofffaserbündeln (engl.: carbon fibres (CFs)) ermöglichen eine In-situ-Schadensüberwachung in GFK aufgrund von schadensbedingten Permittivitätsänderungen. Sich entwickelnde Schäden mit eingeschlossener Luft führen zu einer insgesamt niedrigeren Permittivität und damit zu einem Abfall der Kapazität. Zugversuche an Kreuzverbundproben zeigen eine klare Korrelation zwischen der Entwicklung von Matrixrissen und der Abnahme der Kapazität. Ein analytisches Modell ermöglicht die Bestimmung der Anzahl der Matrixrisse anhand der gemessenen Kapazitätsänderung und somit eine In-situ-Bewertung des Schädigungszustands. Die Empfindlichkeit der Messungen wird durch den Abstand der CF-Bündel beeinflusst und eine Integration der CF-Bündel in unterschiedlich orientierte Laminatschichten ermöglicht die Überwachung des gesamten Versagensprozesses des Verbundwerkstoffs. Darüber hinaus wird eine Erkennung und Größenabschätzung von Schlagschäden demonstriert.

Beide vorgestellten Methoden ermöglichen ein bedienerfreundliches In-situ-SHM in Echtzeit ohne signifikante Beeinflussung der mechanischen Materialeigenschaf-

ten. Die Sensorherstellung und -integration kann ohne großen Mehraufwand in bestehenden industriellen Fertigungsprozessen implementiert werden. Ein geeignetes, maßgeschneidertes Sensordesign ermöglicht eine rechtzeitige Schadenserkennung und ein tieferes Verständnis des Versagensprozesses von Verbundwerkstoffen. Daher trägt diese Arbeit zu einem sichereren und effizienteren Einsatz von Leichtbau-GFK-Verbundwerkstoffen bei.

Contents

List of Abbreviations

AC	Alternating current
AET	Acoustic emission testing
CF	Carbon fibre
CFRP	Carbon fibre reinforced polymer
CNP	Carbon nanoparticle
CNT	Carbon nanotube
CP	Cross-ply
CVD	Chemical vapour deposition
DC	Direct current
DIC	Digital image correlation
FBG	Fibre Bragg grating
FOS	Fibre optic sensor
FRP	Fibre reinforced polymer
GFRP	Glass fibre reinforced polymer
ILSS	Interlaminar shear strength
MWCNT	Muli-walled carbon nanotube
NDT	Non-destructive testing
OHT	Open-hole tensile
PTFE	Polytetrafluoroethylene
QI	Quasi-isotropic
SHM	Structural health monitoring
SWCNT	Single-walled carbon nanotube
UD	Unidirectional
VARTM	Vacuum-assisted resin transfer molding

1 Introduction

Glass fibre reinforced polymers (GFRPs) are used in numerous structural applications, where a reliable and safe operation is crucial. The high safety requirements demand detailed knowledge of the material's damage state and failure process. However, fibre reinforced polymer (FRP) composites exhibit a complex failure behaviour due to their multi-scale structure.
The E-glass GFRP laminates used throughout this thesis consist of stacked unidirectional (UD) plies with different fibre orientations. Each UD ply contains long, parallel load-bearing glass fibres with high stiffness and strength embedded in a polymer matrix, protecting the fibres and transferring the load between them. The failure process of composites includes different damage modes. In the polymer matrix, cracks occur intra-laminar parallel to the fibres as matrix cracks or interlaminar between two plies as delaminations. In general, matrix damages themselves do not lead to total laminate failure but severely influence the composite's mechanical properties and further failure process. Catastrophic failure is typically governed by fracture or kinking of fibre bundles - referred to as fibre failure. Typically, the failure modes influence each other as they do not arise separately. Furthermore, the failure process is strongly influenced by various factors, e.g. loading, laminate lay-up, environmental conditions, manufacturing flaws and pre-existing damages. Hence, no generally valid failure sequence can be defined for composite components. Detailed knowledge of the current failure progress is essential for the safe use of FRP structures. However, even severe damages like large delaminations and extensive matrix cracks that strongly influence the performance are often undetectable by visual inspection due to the complex failure behaviour, the layered structure and painted surfaces. Consequently, an inspection of structural parts using established non-destructive testing (NDT) methods is nowadays periodically performed to evaluate the current material state and avoid catastrophic failure. The maintenance intervals often require costly machine downtimes and can result in late damage detection. Many NDT methods, e.g. thermography or ultrasonic inspection, require expen-

sive equipment, trained personnel and can only be carried out in specific areas. Especially in large complex components, some parts of the structure might be difficult or impossible to access using NDT methods.
To increase reliability, cost-efficiency, and exploit higher potentials of lightweight design, various structural health monitoring (SHM) techniques based on different physical effects have been developed to continuously monitor the material integrity during operation. Requirements for an SHM system are manifold [5–7]:

1. Real-time monitoring
2. High reproducibility and reliability
3. Distinct measurement signal
4. No reduction of material properties
5. Simple operation and interpretation
6. Low weight and space requirements
7. Easy, large scale manufacturing
8. Monitoring of inaccessible locations

Many existing SHM methods require complex sensor networks of surface-mounted or embedded sensors that increase weight, are susceptible to environmental effects, or affect the material's mechanical properties.
Especially in conductive materials like carbon fibre reinforced polymers (CFRPs), electrical resistance measurements for strain and damage detection are an established SHM technique that allows monitoring of the whole structure without complex, additional sensors [1, 8–11]. Electrical measurements mainly do not require expensive equipment and can easily be performed during operation to achieve real-time monitoring and damage detection. The results can be transmitted wirelessly, enabling simultaneous, off-site evaluation of many parts. However, electrical monitoring is hardly possible in unmodified GFRP parts like wind turbine rotor blades due to the lack of material conductivity.

1.1 Aims and Scope

Following the presented requirements and challenges, this thesis focuses on establishing electrical SHM methods for damage and condition monitoring in GFRPs. Figure 1.1 schematically shows the aim of this work to enable simple, reliable electrical measurements that allow in-situ monitoring and external material state evaluation of GFRP components in real-time.

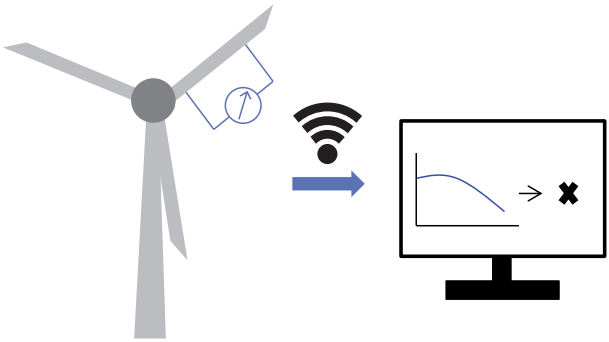

Figure 1.1: Electrical structural health monitoring on a wind turbine blade for in-situ damage detection

Therefore, the following global, central research hypothesis is assessed throughout this thesis:

Real-time damage detection and evaluation of GFRP structures can be achieved using in-situ electrical measurements.

Two types of modification of GFRPs with conductive materials are investigated. The first approach describes a local modification of the matrix, while the second includes a local substitution of the fibres. Both developed methods are evaluated concerning their suitability for damage monitoring and their influence on the material properties. The integrated sensors should not have a foreign body effect and thus not deteriorate mechanical properties. In addition, simple and cost-efficient integration in established manufacturing methods is desired.

Different researchers proved the ability of resistive SHM of polymers or GFRPs by modifying the matrix using conductive nanoparticles [1–4]. However, particularly for large structures, a modification of the entire matrix is expensive. Therefore, Chapter 4 introduces a method for local, conductive matrix modification using fully-integrated pre-cured carbon nanotube (CNT)/epoxy films to enable strain and damage monitoring by electrical resistance measurements. The following sub-research hypothesis is derived for Chapter 4:

The local matrix modification with fully-integrated sensor films allows strain and damage monitoring in GFRPs by electrical measurements.

To evaluate the sub-research hypothesis, first, the manufacturing and integration process of the developed pre-cured CNT/epoxy thin-film sensors is described. Afterwards, the strain and damage sensing capabilities are analysed for various quasi-static and step-wise load cases and different laminate lay-ups, considering the sensors' influences on the mechanical properties. The effect of local stress concentrations is studied in open-hole tensile (OHT) tests. Furthermore, the cyclic behaviour is evaluated in fatigue tests and first component tests on a stringer are performed.

In contrast to resistance measurements, electrical capacitance measurements can be performed on non-conductive materials using integrated or surface electrodes. Surface electrodes are, however, exposed to environmental influences. Hence, Chapter 5 describes a process of local integration of conductive fibres in GFRPs and deals with the following sub-research hypothesis:

The local integration of electrically conductive fibres enables in-situ damage detection in GFRPs.

For this purpose, glass fibre bundles are replaced at specific intervals by carbon fibre (CF) bundles, copper strands or solid copper wires. The foreign body effect of the integrated conductors is analysed, as the integration should not significantly reduce the mechanical properties. The integrated conductors are contacted to serve as capacitor walls. The detection capability of capacitance-based methods relies on a change of dielectric properties of the material due to induced damages. Matrix crack and impact damage detectability are evaluated,

and an analytical model correlating capacitance decrease and damage extent is developed.

1.2 Thesis Outline

The thesis consists of six chapters. After this introduction, Chapter 2 presents the state of the art, including a general and brief overview of different NDT and SHM methods. The focus is set on electrical SHM and conductive modification of polymers. In Chapter 3, the used materials, manufacturing and test methods are stated. More specific details are additionally explained within the respective chapters. As described above, Chapters 4 and 5 each discuss one of the two sub-research hypotheses, focusing on electrical SHM in GFRPs. The chapters can mostly be considered individually due to their structure consisting of 'Materials and Experimental Setup'-, 'Results and Discussion'- and 'Conclusion'-sections. Chapter 4 evaluates the sensing capabilities of local matrix modification with fully-integrated, conductive CNT/epoxy thin-film sensors. Chapter 5 describes a novel SHM method using capacitance measurements on integrated conductive fibres. Parts of this thesis have previously been published in journal articles [12–14].

2 State of the Art

2.1 Structural Health Monitoring of Composites

The assessment of the material state and integrity is essential for safe and reliable operation of composite structures. Therefore, a variety of NDT methods for detection of damages in composites have been developed, including ultrasonic methods, thermography, radiography, and eddy current methods [15–17]. Most NDT inspections can only be carried out locally and during maintenance, which can lead to late detection of damage, frequent maintenance intervals and expensive downtimes. Especially in large complex components, some parts of the structure can only be tested with difficulty or not at all using NDT methods.
In contrast to time-based examinations, condition-based monitoring during operation can significantly increase the composite structures' safety, reliability and cost-efficiency [7]. Material state assessment during operation is referred to as SHM [6, 7]. In particular, real-time, online SHM allows for immediate, in-situ damage detection and monitoring of the material integrity during service. SHM techniques allow for global monitoring such that in contrast to NDT methods, no single-point measurements are required [15].
Various SHM methods have been developed and are still part of ongoing research [7, 18–20]. SHM is based on the fact that material damage will significantly alter the material response and therefore the monitored property [7]. If the measured signal reaches a defined threshold, the operation of the structure is regarded as critical. Different measuring principles and signal processing methods can be used to find threshold values of the monitored properties up to which a satisfactory and safe operation is possible. [6]
In general, SHM monitors the material response as a result of different energy forms - mechanical waves, electromagnetic waves, electric excitation. Passive SHM methods require embedded or attached sensors. During active SHM, the structure is excited using actuators, and the system response is measured [19]. A suitable sensor design, including type and location of the sensors, is essential

for a reliable and accurate operation of SHM systems [6].
In the following, an overview of different SHM methods for damage monitoring in composites is presented. The focus lies on the methods and aspects that are important for this work. Further information can be found in the respective literature. Although many SHM methods exist and much research is performed in this field, considerable research is needed to safely implement and apply the developed methods in practice [20].

Strain gauges

Despite all advanced SHM methods, local strain measurements of composite components using surface-mounted resistance strain gauges in critical loading areas are still common as no expensive measuring equipment is required [19, 21]. Strain gauges are an established technique, and experience enables reliable interpretation of the results of the strain measurements [21]. However, surface-mounted strain gauges only monitor small areas, cannot provide information about internal strains and are susceptible to external influences. Furthermore, installation at many points requires long installation times and complex wire routing or more expensive wireless sensors.

Vibration-based methods

Different vibration-based methods exist for composite SHM. The methods are based on wave propagation of mechanical waves. Either the characteristics of wave reflection are monitored, or standing wave properties are analysed. [20] Hence, small damages that do not influence the physical parameters of the structures like stiffness, mass and damping are undetectable by vibration-based methods [22]. Often the measured phenomena are significantly influenced by environmental and operating conditions such that complex data evaluation and modal analysis is necessary to achieve reliable results [23, 24].
Active methods excite the structures using specific frequencies [25]. Damages inside the composite influence the propagation characteristics of the vibration response since geometrical or mechanical properties are changed [19]. Consequently, different parameters of the response like frequency, mode shape and power spectrum are analysed in comparison with the undamaged response [5, 23, 26]. Often, piezoelectric transducers are attached to the composite structure for wave introduction or sensing [19]. The piezoelectric effect results in a charge

response in a stress field (sensor), or inversely an electric field can lead to a strain response in the transducer (actuator) [27].
In 1917, Lamb [28] introduced the phenomenon of guided, elastic waves in thin-walled, homogeneous, isotropic structures nowadays referred to as Lamb waves. Lamb waves can propagate independently symmetrical or anti-symmetrical to the plate's neutral axis and enable thickness measurements [29], determination of the elastic constants [30], and damage detection [18, 20]. Damages inside the material influence the propagation of the Lamb waves and can be detected from the measurement signal [19]. Lamb waves show a higher sensitivity to local defects than other vibration-based methods like frequency response methods, enabling better classification and localisation of the damage [31].

Acoustic emission

Acoustic emission testing (AET) is a typical passive SHM method for damage detection. Surface-mounted piezoelectric transducers monitor transient, elastic sound waves propagating inside the material as a result of sudden stress release during damage evolution [32]. Therefore, AET requires loading and is not able to predict damage onset before occurrence or monitor strains [18]. Nevertheless, AET enables real-time detection of damage onset during loading even if only minor damage is present. By analysing the characteristics of the high-frequency waves, including amplitude, frequency and energy, a distinction between different failure mechanisms like matrix cracks, delaminations, and fibre fracture is possible. However, the classification of failure modes is complex and not generally valid for different materials. Consequently, a conscientious analysis of the waves' characteristics requires significant signal processing, pattern recognition and profound knowledge. [33] Additionally, the damage detection and localisation potential is highly depended on the sensor location [34].

Fibre optic sensors

Light-conducting fibres can be used as integrated fibre optic sensors (FOSs) and enable SHM of composite materials [20, 35]. FOSs are corrosion resistant, unaffected by electromagnetic fields, and are able to monitor temperatures and the curing process [15]. However, extensive optoelectronic equipment is required [20].
Optical fibres consist of a core with a high refractive index and an outer layer

with a low refractive index. The light inside the fibres is reflected at the interface between the core and outer layer and consequently guided along the fibre [15]. In simple FOSs, the intensity variation of the light resulting from length changes due to strain and transverse cracks is evaluated.
Fibre Bragg gratings (FBGs) are a commonly applied wavelength-based form of FOSs. Specific wavelengths of the light are reflected by the FBGs using the principles of Bragg reflection [36]. The FBGs consist of periodically arranged areas with higher and lower refractive indexes [15, 37]. As length variations of the fibre influence the distance of the gratings, the power spectrum of the reflected light changes [37, 38]. Consequently, strain monitoring is possible when taking into account suitable temperature compensation [37, 39]. Damages like transverse crack evolution in composites can also be monitored by FBGs [38, 40]. However, expensive, thin FOSs are required for implementation in composite materials to minimise the influence on the material properties [20, 40].

Electrical methods

Different electrical SHM methods exist. Both direct current (DC) and alternating current (AC) can be used to analyse the resistance and impedance change of the material due to loading and damage evolution. Electrical measurements on conductive materials enable global, real-time, in-situ measurements without expensive equipment. The material's intrinsic electrical conductivity permits direct resistance measurements on CFRPs without requiring further sensor networks. Damages like matrix cracks, delaminations, and fibre fracture alter the material resistance since conductive paths are interrupted. [1, 8] Therefore, electrical resistance measurements for strain and damage detection are an established SHM technique enabling monitoring of the whole structure [1, 8–11]. Materials with such self-monitoring capabilities are considered self-sensing materials [41, 42]. The material itself is able to detect deformations and damages without additional sensors. Self-sensing materials offer significant advantages for SHM as weight, labour, and costs can be saved [41].
Eddib et al. [43] proved that capacitance-based self-sensing is possible in conductive CFRPs with through-thickness and in-plane capacitance measurements. Artificial damage introduced by 1.1 mm big through-holes could be detected via capacitance measurements on CFRPs when using a thin isolating film between the material and the electrodes of the measurement system. Sorrentino et al. [44] used a similar method and showed that moisture intrusion in CFRPs can

be detected via capacitance measurements.
Furthermore, in-situ AC measurements showed a capacitance decrease during tensile tests on cross-ply (CP) CFRP specimens. Kupke et al. [1] illustrate a correlation of the measured capacitance and dissipation with applied loading, strain and damage state. Abry et al. [45] also performed in-situ AC measurements on CFRP specimens and found a capacitance decrease related to matrix cracks and intra-ply delaminations during flexural loading. However, a direct quantitative correlation between cracks and capacitance change in CFRPs still remains a challenge for many methods.
Unfortunately, resistance-based monitoring is not possible in electrically non-conductive polymers, or GFRPs without modification. This thesis focuses on enabling electrical SHM in GFRP composites. A broader literature review of electrical SHM in GFRPs is given in Section 2.1.1.

2.1.1 Electrical Structural Health Monitoring in GFRPs

Resistance measurements

Resistive monitoring is not possible in unmodified polymers or GFRPs due to a lack of material conductivity. Extensive research on carbon nanoparticles (CNPs) like carbon black, graphene and CNTs lead to exploiting the sensing potential of electrically conductive polymer nanocomposites. A conductive network is formed by dispersing CNPs in polymers when the filler content is above the percolation threshold. This piezoresistive network is susceptible to applied mechanical loads as conductive paths are influenced, formed, or dissolved with deformation. Therefore, resistive SHM of polymers or GFRPs can be achieved with modification of the matrix using conductive nanoparticles [1–4]. The theory and mechanisms will further be discussed in Section 2.2.
Carmona et al. [46] conducted an early study of the piezoresistive behaviour of nanocomposites with different CNP/polymer combinations by analysing the influence of hydrostatic pressure on resistance. Many researchers have proven the strain sensing ability of carbon nanocomposites for different filler types and under various load cases, as summarised in a review paper by Zhang et al. [47]. Advances regarding manufacturing, understanding, and sensitivity of the piezoresistive nanoparticle/polymer sensors are still part of ongoing research [48, 49]. Using modified polymers as matrix material permits the manufacturing of

GFRPs with conductive matrix and intrinsic strain and damage sensing properties. When first integrating CNPs in FRPs, the whole matrix material was modified with conductive CNPs. Kupke et al. [50] manufactured a conductive GFRP by modification of the epoxy matrix using carbon black. Different groups showed the strain and damage monitoring capability of FRPs with a fully modified matrix [2, 51–53]. An alignment of the CNPs in a fully modified matrix improves the fracture toughness and damage-detection sensitivity [54]. Especially for large structures, however, fully modifying the matrix is expensive, and no localised strain monitoring is possible.

Local reinforcements with conductive fillers are part of ongoing research [55–60]. Many promising results have been published about surface-mounted carbon nanotube/polymer sensors on different substrates [56, 61–66]. Therefore, premanufactured thin-films or CNT buckypapers have been adhesively bonded to the surface or deposited directly on different substrates by layer-by-layer deposition or spray coating and tested under various load cases. Similar to classical metal strain gauges, the surface-mounted sensors or conductive coatings are susceptible to external influences and damage.

Research on integrated local modification of GFRPs for resistive strain monitoring via fibre coating, partial modification of the matrix, or embedding of CF, CNT fibres, or CNT film strain gauges in GFRPs is still limited. Alexopoulos et al. [55] suggested a process with direct placement of CNT fibres, manufactured in an elaborate coagulation process, on dry glass fibre fabrics, which were infused in a vacuum infusion process. The mechanical tensile properties of the samples with embedded CNT fibres were found to be equal to non-modified specimens. In tensile and flexural tests, the authors correlated the electrical resistance change with the applied strain. Furthermore, Forintos et al. [67] proved the possibility of resistive strain monitoring on embedded CF bundles in GFRP.

A modification of the fibre interphase of glass fibres with CNTs by the doctor knife method [68, 69] or direct chemical vapour deposition (CVD) [70] showed promising results for strain sensing ability. However, these methods require many manufacturing steps and are hard to automate or realise on a large scale. Gao et al. [71] showed the possibility of strain, temperature, and relative humidity sensing in GFRPs via electrical resistance measurements when dipping entire dry glass fibre fabrics in various aqueous multi-walled carbon nanotube (MWCNT) dispersions and infusing the dried fabrics with epoxy. More advanced methods for applying CNTs directly on dry glass fibre fabrics are layer-by-layer deposi-

tion or spray coating [72–75]. The methods showed promising results regarding piezoresistive strain and damage sensing under different load cases and offered possibilities for local tensile or compressive strain monitoring in flexural tests. However, spray application of CNTs requires many safety precautions and some effort to produce homogeneous and reproducible layer thicknesses.

Another possibility to locally integrate CNTs in GFRPs is using CNT buckypapers or CNT sheets. Aly et al. [59, 76] suggested a method to implement aligned CNT sheets in the interlaminar region of GFRP prepreg laminates and proved the strain sensing capabilities under various forms of tensile [76] and flexural loading [59]. Kravchenko et al. [77, 78] embedded CNT buckypapers in the large areas of the interlaminar region using frictional roller sliding on glass fibre fabrics in a wet hand lay-up process. They found an increase in mode I and mode II interlaminar fracture toughness as well as a strain and damage monitoring capability through resistance measurements. The manufacturing process using wet hand lay-up is hard to automate and susceptible to manufacturing deviations. Especially on an industrial scale, GFRP parts as wind turbine rotor blades are manufactured in a vacuum infusion process. In a study by Wu et al. [79], a commercial buckypaper with randomly oriented CNTs manufactured in a CVD process was used as a conductive interlayer in GFRP composites. The buckypaper was placed directly on a dry glass fibre fabric and then infused by vacuum infusion. During high strain rate compressive loading using a Hopkinson bar, the in-situ electrical resistance was measured, and the resistance increase provided information about strain and damage inside the specimen. CNT buckypapers require a high caution during handling as they can easily break. Slobodian et al. [80] integrated entangled MWCNT buckypaper manufactured with vacuum filtration on a polyurethane membrane in GFRP laminates during vacuum infusion. They showed a resistance change during infusion as well as during bending over a cylindrical surface. When including the filter membranes, e.g. polyurethane, in the final composite, the influences on the bonding with the used matrix polymer have to be considered. Despite all research, an automatable technique enabling reliable, easy, fast, and safe large-scale production of fully-integrated sensors to measure strain and damage in GFRPs without significant loss of mechanical properties is still desired [65].

Capacitance measurements

In contrast to resistance measurements, electrical capacitance or impedance measurements offer the possibility of electrical SHM even in non-conductive composites using integrated or surface electrodes. The detection capability of capacitance-based methods relies on a change of dielectric properties of the material. In general, all effects that lead to a permittivity change within the material - like e.g. damages and moisture - can be detected using capacitance-based SHM. In concrete structures, impedance or capacitance measurements are applied for the detection of voids and damages [81–83], rebar reinforcement corrosion and localisation [84, 85], as well as detection of moisture [86, 87] (review: [88–90]). Coplanar electrode pairs without surface contact are used during capacitive imaging to scan across a surface, measuring changes in charge for given voltages resulting in a map of electrical property changes enabling detection of cracks, voids or moisture [91].

However, for polymers or GFRPs, research on capacitance or impedance measurements for damage detection is limited. Chakraborty et al. [92, 93] used capacitance measurements for stress and interlayer defect detection in 3D-printed polymers. As in concrete, capacitative imaging with coplanar non-contact electrodes can also be used for moisture or damage detection and localisation in different FRP composites as CFRPs [94–97], honeycomb structures [95], and GFRPs [95, 98].

Asmatulu et al. [99] have shown a method for non-destructive detection of drilled holes and moisture influence in GFRP using a capacitance bridge. At certain test intervals, the GFRP plates were placed between two round electrodes on top and bottom. An increasing void and water content resulted in measurable changes in the material's relative permittivity.

Raihan et al. [100] developed an in-situ dielectric property measurement method for damage detection in tensile tests on woven GFRP composites using surface-mounted electrodes. Evaluating the impedance at different frequencies, known as electrical impedance spectroscopy, offers the possibility for moisture intrusion monitoring [101, 102] and damage detection [101, 103, 104] in GFRPs. The specimens in the studies were fully covered with metal foil electrodes on both sides or regularly placed between contact plates for measurements.

Most of the presented methods are hardly eligible for in-situ monitoring of parts in the described ways as they require measurements using non-contact measurement electrodes or complete covering of the samples with contact plates.

Furthermore, the surface-mounted electrodes are prone to measurement errors due to environmental influences and have a high risk to be damaged. Integrated electrodes could overcome some of the problems, but can result in a foreign body effect that reduces the mechanical performance.
Recently, piezoelectric sensors embedded in GFRPs have also been used as capacitance sensors [105, 106] instead of just as acoustic emission [107, 108] or voltage sensors [109, 110] as established by many research groups (review in [111]). It was shown that capacitance measurements on embedded piezoelectric transducers are in good agreement with loading and unloading trends in different tensile tests on GFRPs [106]. Salas et al. [112] successfully used integrated commercial capacitance sensors for moisture monitoring in epoxy and CFRPs. However, the sensors' influence on the mechanical properties and durability is a concern and should be subject to further analysis. The intrusiveness of the sensors depends on the material combination and size of the sensors and should be considered. Especially when using sensor networks with multiple sensors for monitoring of larger areas and localisation of damages, the influence on the mechanical properties could be significant. [111, 112] Therefore, integrated electrodes that do not significantly influence the mechanical material behaviour are desired. Furthermore, additional research is needed to gain a comprehensive understanding of dielectric material changes.

2.2 Carbon Nanoparticle Modified Polymers

By modification of insulating polymers with various conductive fillers, electrically conductive polymers can be achieved. A conductive network is formed when the filler content is above the percolation threshold (see Section 2.2.2). In general, conductive fillers can consist of different materials. Nevertheless, the enhancement of polymer matrices with CNPs has gained particular research interest [113]. CNPs, like carbon black, few-layer graphene or CNTs, are a material-conform and advantageous filler choice for lightweight polymer composites due to their chemical structure and high specific mechanical properties. Carbon black consists of spherical particles with diameters of 10 to 100 nm that tend to agglomerate. Few-layer graphene consists of a small number of atomic layers with sp^2-hybridised carbon. CNTs have a hollow, cylindrical structure and consist of rolled-up graphene layers with sp^2- hybridised carbon atoms. Due to the high aspect ratio of CNTs, lower filler contents are sufficient to produce con-

ductive polymers compared to carbon black and few-layer graphene [114–116]. Hence, CNTs are used as conductive fillers throughout this thesis.

2.2.1 Carbon nanotubes

CNTs gained a great deal of attention through the work of Iijima [117], demonstrating the arc discharge method for the synthesis of CNTs without catalysts. Other typical synthetisation methods for CNTs are CVD or laser ablation [118–120]. Depending on the number of rolled-up graphene layers, different types of CNTs can be distinguished. Single-walled carbon nanotubes (SWCNTs) are formed by a single graphene layer and typically have diameters between 0.4 and 3 nm. MWCNTs consist of more than one concentric cylinder. The properties of CNTs are significantly influenced by the number of walls, the dimensions and the chirality. The chirality vector C is composed of integer multiples m and n of the basis vectors a_1 and a_2 [121] according to Equation (2.1).

$$C = m \cdot a_1 + n \cdot a_2 \tag{2.1}$$

Three different geometric arrangements of CNTs are distinguished according to the chirality - zigzag, armchair, and chiral [119]. Figure 2.1 shows a schematic of the classification using the angle ϑ between the basis vectors a_1 and a_2. The electrical properties of the CNTs are influenced by the chirality. CNTs can have metallic (conductive) or semiconductive properties [122–125]. All armchair CNTs (m=n=3) and CNTs that fulfil $|n - m| = 3 \cdot z$ with z being an integer are conductive. All other CNTs are considered semiconductive and do not reach their full conductivity at room temperature. Different chiralities can be included in one MWCNT, which leads to the fact that the conductivity properties of MWCNTs are difficult to predict. In addition, the electrical properties of CNTs are significantly influenced by defects of the carbon network like defects in the crystal lattice, topological defects, or hybridisation effects [126, 127]. Thus, the electrical properties of CNTs can vary considerably and cannot be given in general terms [113].

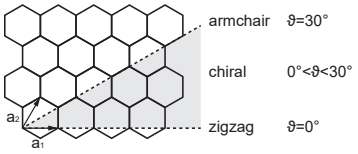

Figure 2.1: Classification of CNTs with angle between basis vectors of chirality vector

2.2.2 Percolation Theory

Due to their low conductivity in the range of 10^{-10} to 10^{-15} $\mathrm{S\,m^{-1}}$, polymers are considered electrical insulators [128]. The addition of electrically conductive particles in polymers can result in conductive polymers. However, a certain filler content has to be present to obtain a conductive network. The filler content for which the polymer changes from isolating to conductive is known as the percolation threshold [129]. Figure 2.2 shows schematics of three filler contents and the respective electrical conductivity as a function of the filler content. No conductive network is formed for a filler content below the percolation threshold, and the filled polymer's conductivity is similar to the unmodified matrix. At the percolation threshold, the conductivity increases several orders of magnitude. Within the polymer, the first continuous electrical network paths have formed, which are responsible for the increased conductivity. A further increase of the filler content leads to the formation of more electrical network paths, but these only result in a slight conductivity increase. [130]

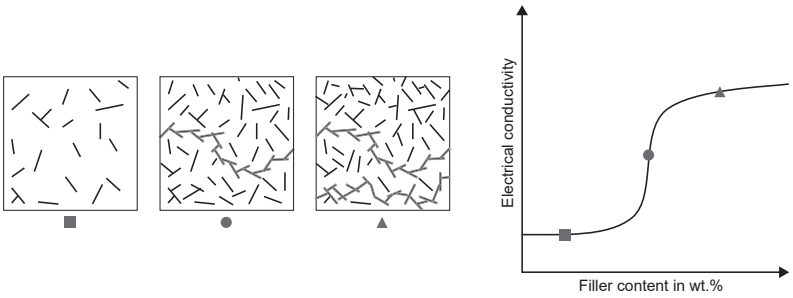

Figure 2.2: Percolation threshold in CNT/epoxy systems - Schematic network for three different filler contents and electrical conductivity versus filler content

Various theoretical models for the percolation of filled polymers exist [129]. In its simplest form, the percolation theory is a statistical description where the network is regarded as a lattice. The lattice points have two different states - they are either occupied or unoccupied by a conductive particle. With a higher filler content, the probability of connected electrical paths and thus percolation increases. The scaling law in Equation (2.2) states the electrical conductivity σ_c as a function of the filler content p according to the classical percolation theory, where c is a constant and p_c is the percolation threshold [129].

$$\sigma_c = c(p - p_c)^t \tag{2.2}$$

The exponent t varies with the geometry of the particles [129, 131]. An ideal shape and random, homogeneous distribution of nanoparticles is assumed for the purely statistical description. Furthermore, no diffusion, particle movements and interactions like agglomeration are considered. However, the actual percolation threshold is highly dependent on the filler type, distribution and particle interaction [132–134].

The geometry of the fillers has a significant influence on the percolation [135]. The percolation threshold of two- and three-dimensional objects can be described using the excluded volume considering CNTs as homogeneously distributed, rigid rods [114]. As a resulting approximation, the percolation threshold p_c for particles with a high aspect ratio η can be calculated with Equation (2.3) [114].

$$p_c = \frac{1}{\eta} \tag{2.3}$$

However, in reality, the high aspect ratio and the entanglements of the CNTs favour a lower percolation threshold than theoretically calculated [114, 128, 136–138].

Furthermore, purely statistical percolation models are usually not very accurate, as the significant influence of chemical particle interactions is not taken into account. The nanoparticles tend to agglomerate. The agglomeration of CNPs is influenced by attractive and repulsive forces like coulombic interactions and Van-der-Waals-forces [139, 140]. During manufacturing of CNT/polymer composites, high shear forces are necessary to break up the agglomerates since, for small particle distances, the attractive Van-der-Waals-forces prevail, and a stable energy minimum is obtained by agglomeration [136, 141]. The potential barrier has to be overcome to separate the agglomerates [139, 142]. Therefore,

three-roll mill or ultrasonication methods are used during the manufacturing of filled polymers to achieve a homogeneous distribution of nanoparticles [115, 136, 143–145].
The conductivity of the filled polymers is influenced by the intrinsic resistance of the CNTs and the interparticle resistance. Interparticle resistances consist of direct contact resistances between two particles and tunnelling resistances. Some particles are not in direct contact, but instead, a thin polymer film is present between them. However, a conductive network can still be formed as electrons can pass through the gap by quantum tunnelling [146]. The conductivity of these particle-particle contacts with a thin insulating polymer film is described with the tunnelling model by Simmons [147–150] and has a significant influence on the overall material conductivity [151, 152]. To enable tunnelling, the particle separation must be smaller than the material-specific tunnelling distance and thus only amount to a few nanometres [153–155].

2.2.3 Piezoresistivity

Load application results in a modification of the filler particles' network. Therefore, the conductive CNT/polymer composites exhibit a piezoresistive behaviour, as the resistance changes as a consequence of loading. Particle contacts, distances and therefore tunnelling resistances change, and conductive paths can be formed or resolved [130, 156–160]. Furthermore, deformation of the CNTs also induces an intrinsic piezoresistive effect [61, 63, 130, 157]. The intrinsic resistance changes substantially for small strains [157]. However, the overall influence of the CNTs' inherent piezoresistive effect is small as the absolute value of contact and tunnelling resistances is significantly larger [157, 158].
The piezoresistive effect enables self-sensing of the material. Strains can be detected by resistance changes without requiring additional sensors. Self-sensing materials allow for cost-efficient and material-conform SHM. Hence, the piezoresistive behaviour of filled polymers has extensively been studied in the last few years [49, 63, 116, 156, 160–164]. In a simple manner, tensile loads result in higher particle distances and consequently a higher resistance. Compressive loads show the opposite trend as particles are moved closer together. Nevertheless, the deformation of the material perpendicular to the applied load, known as the Poisson's effect, also influences the filler network. [160, 163]
Material damages like matrix cracks can result in significant, irreversible resistance changes when the particle network is permanently destroyed [165].

Sensors with a filler content close to the percolation threshold experience the highest sensitivity, as few conductive paths exist, and a loss of contact of the CNTs thus has higher effects on the resistance [130, 166–168]. Furthermore, filler aspect ratio, dispersion state, and alignment of the CNTs influences the sensitivity [116, 169, 170].

In general, all environmental conditions like moisture, temperature and pressure, resulting in a volumetric material change and therefore a modification of the particle network, induce resistance changes [170]. Hence, environmental conditions should be considered when evaluating sensor performance [130].

3 Materials and Methods

This chapter gives general information about the materials, the manufacturing processes and the experimental methods. Thus, duplication of descriptions of the same manufacturing methods in the individual chapters is avoided. More detailed information for manufacturing methods, laminate lay-ups, sample preparation, and test procedures, which only apply to specific sample types, are given directly in the 'Materials and Experimental Setup'-sections of Chapters 4 and 5. For simplicity and readability, materials and equipment introduced in this chapter will occur using the material name without stating the manufacturer in the further course of this thesis, as all information can be found in this chapter.

3.1 Materials

3.1.1 Glass Fibres

Different E-glass fibre fabrics with polymer stitching yarns were used throughout this thesis. Mostly, UD, non-crimp E-glass fibre fabrics UT-E250 and UT-E500 (Gurit Holding AG, Switzerland) were utilised. The fabrics consist of the same fibres and differ regarding their aerial weight. UT-E250 has an aerial weight of $250\,\mathrm{g\,m^{-2}}$ and UT-E500 has an aerial weight of $500\,\mathrm{g\,m^{-2}}$. Additionally, a UD glass fibre fabric U-V-E-926 (SAERTEX GmbH & Co. KG, Germany) consisting of SE1500 E-glass fibres with glass fibre aerial weight of $904\,\mathrm{g\,m^{-2}}$ and a bidiagonal $\pm 45^\circ$ glass fibre fabric B320E-H (HP-Textiles GmbH, Germany) with an aerial weight of $320\,\mathrm{g\,m^{-2}}$ were used for some tests. Details about the used fabrics and their lay-ups are given for all sample types in the 'Materials and Experimental Setup'-sections of Chapters 4 and 5.

3.1.2 Epoxy Resin

The amine-based two-component epoxy system EPIKOTE™ Resin MGS™ RIMR 135 and EPIKURE™ Curing Agent MGS™ RIMH 137 (Hexion Inc, USA) was used throughout this thesis. A mixing ratio of 100:30 weight shares was applied according to the manufacturer's specifications. Prior to infusion, the matrix system was mixed and degassed in a vacuum stirrer at 200 min^{-1} for approximately 30 minutes.

3.1.3 Carbon Nanotubes

In this thesis, Tuball™ SWCNTs by OCSiAl were used. According to the manufacturer's analysis, the carbon content is 86 ± 1 wt.% and the CNT content 81 ± 1 wt.%. The remaining parts consist of metal impurities. The lengths of the CNTs are larger than 5 µm, and the outer mean diameter is given as 1.6 ± 0.4 nm.

3.1.4 Carbon Fibre Rovings

In some experiments, untwisted CF rovings FT300B 6000-50B (Toray, Japan) were used. The fibre diameter is 7 µm, according to the manufacturer's datasheet. One roving consists of 6000 individual fibres and has a cross-sectional area of 0.23 mm^2. The electric resistivity in fibre direction is given as $1.7 \cdot 10^{-3}\ \Omega\,\text{cm}$.

3.1.5 Silver Paint

For manual contacting of the specimens, conductive silver paint Acheson 1415 (PLANO GmbH, Germany), consisting of approx. 57 % silver and a thermoplastic resin as a binder, was used.

3.2 Manufacturing Processes

3.2.1 GFRP Plates

All GFRP laminates were manufactured in a vacuum-assisted resin transfer moulding (VARTM) process and had fibre volume fractions around 50%. Therefore, a rectangular, closed mould aluminium mould with frames of different thicknesses was used. The release agent XTEND 1110EP (Axel Plastics, USA) was

applied on all mould surfaces. The dry fibre fabrics were stacked on the bottom part of the mould in the desired lay-up. Around the edges of the fabrics, 1 cm wide fleece strips were placed to prevent resin channelling and secure the fabrics against movement. After closing the mould with screws, infusion with the epoxy resin took place in a heat press. Therefore, a vacuum was applied on the trap side, and a clamp on the source side controlled the resin flow. After infusion, a pressure of 2 bar was applied to the source side to compensate for shrinkage during curing. Curing was performed in the heat press at 50 °C for 16 h. Post-curing was carried out for 16 h at 80 °C in an oven.

3.2.2 Specimen Preparation

The manufactured plates were cut into specimens according to the respective dimension given in the test standards using an ATM Brillant 265 saw (ATM Qness GmbH, Germany) with a diamond blade. Table 3.1 shows the performed tests, including respective standards and dimensions. The compression specimens were equipped with 1 mm-thick GFRP loading tabs before cutting. Therefore, the respective areas were ground using 600 grit sanding paper and cleaned using isopropanol. The tabs were bonded using a two-component UHU® Endfest 300 (UHU GmbH & Co. KG, Germany) adhesive, which was cured for 60 minutes at 60 °C and 20 kN in a heat press. To minimise manufacturing effects in the test results, specimens for each test were manufactured from at least two different plates.
Electrical contacting took place on the specimens' edges using Acheson 1415 (PLANO GmbH, Germany) conductive silver paint and LiFy cables with 0.25 mm^2 cross-section. The exact contacting positions are discussed within each chapter.

3.3 Experimental Methods

3.3.1 Mechanical Tests

The following sections describe the performed mechanical tests. All tests were performed at ambient room temperature of 20 ± 1 °C and relative humidity of $50 \pm 10\%$. The tests were carried out according to the test standards specified in Table 3.1.

Table 3.1: Test standards and specimen dimensions for performed tests [171–175]

Test	**Standard**	**Dimension** LxWxH in mm^3
Tension	DIN EN ISO 527-4	250x25x2
Three-Point Bending	DIN EN ISO 14125	100x15x2
Compression	ASTM D3410	130x30x4 130x10x4
Interlaminar Shear Strength	ASTM D2344	24x8x4
Open-Hole Tesion	ASTM D5766	250x36x4

Tensile Tests

Quasi-static tensile tests according to DIN EN ISO 527-4 [171] were performed on a 400 kN universal testing machine (ZwickRoell GmbH & Co. KG, Germany) using mechanical, 100 kN pre-tensioned wedge grips. The displacement was measured using a multiXtens contact extensometer (ZwickRoell GmbH & Co. KG, Germany) or an ARAMIS 4M digital image correlation (DIC) system (GOM GmbH, Germany). Quasi-static tests up to final failure and force-controlled step-wise tests were performed. Specific setup details are described in the respective chapters. The tensile stress σ_t was calculated according to Equation (3.1) with force F, specimen's width w and thickness t.

$$\sigma_t = \frac{F}{wt} \tag{3.1}$$

Open-Hole Tensile Tests

A 400 kN universal testing machine (ZwickRoell GmbH & Co. KG, Germany) with mechanical, 100 kN pre-tensioned wedge grips, was used for OHT tests. The tests were carried out following ASTM D5766 [175]. The near field stress σ_{nf} was calculated with force F, hole diameter d, specimen's width w and thickness t according to Equation (3.2).

$$\sigma_{nf} = \frac{F}{(w-d)t} \tag{3.2}$$

Fatigue Tests

The tension-tension fatigue tests were performed on a servo-hydraulic 100 kN test machine 8800PL100K (Instron, USA). A contact pressure of 40 bar was used to fix the samples in the hydraulic wedges. Specimens were subjected to a force-controlled, constant amplitude, sinusoidal wave with a frequency of 5 Hz and a load ratio of R=0.1. The software WaveMatrix™ was applied for test definition and data acquisition.

Three-Point Bending Tests

Three-point bending tests were performed using a Z10 universal test machine (ZwickRoell GmbH & Co. KG, Germany) following DIN EN ISO 14125 [172]. The test speed was 2 $\mathrm{mm\,min^{-1}}$. The upper roller diameter was set as 15 mm, the lower diameter as 10 mm, and the support distance was 60 mm. The bending stress was calculated following Equation (3.3) using force F, support distance L, specimen's width w and thickness t.

$$\sigma_b = \frac{3FL}{2wt} \tag{3.3}$$

A schematic setup is shown in Figure 3.1.

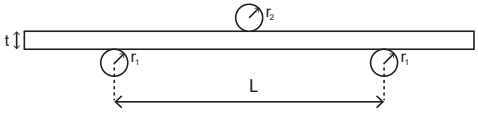

Figure 3.1: Schematic setup of three-point bending tests

Interlaminar Shear Strength Tests

The interlaminar shear strength (ILSS) tests were performed according to ASTM D2344 [174] using a Z10 universal test machine (ZwickRoell GmbH & Co. KG, Germany). The diameter of the lower rollers was chosen as 3 mm, the diameter of the upper roller as 6 mm, and the support distance as 16 mm. The test speed was 1 $\mathrm{mm\,min^{-1}}$. Stress calculation and setup are similar to the three-point bending tests shown in Figure 3.1.

Compression Tests

A 400 kN universal testing machine (ZwickRoell GmbH & Co. KG, Germany) with a hydraulic combined loading fixture (IMA Dresden, Germany) was used during compression tests. The load was applied in shear loading setup following ASTM D3410 [173]. The compressive stress was obtained from Equation (3.4) using the applied force F and the specimen's width w and thickness t.

$$\sigma_c = \frac{|F|}{wt} \tag{3.4}$$

Impact Tests

Impact damages were introduced on an uninstrumented drop tower (Ceast, Italy) using a semi-spherical impactor with a tip diameter of 20 mm. An anti-rebound system prevented double impacts. The specimens were pneumatically clamped.

3.3.2 Electrical Measurements

The following sections describe the performed electrical measurements. All measurements were performed at ambient room temperature of 20±1 °C and relative humidity of 50±10%. All mechanical test machines were electrically grounded to avoid influences on the electrical measurements. For each combination of simultaneous electrical and mechanical measurements, the devices' relative starting times were determined to achieve the closest agreement between the results. The settings were then reproducibly applied for all respective measurements.

Resistance Measurements

DC resistance measurements were performed in a four-wire setup using a one-channel Keithley 2601A or a two-channel Keithley 2602 (Tektronix GmbH, Germany) for two simultaneous measurements within each sample. A constant voltage of 1 V was applied to the specimens, and the current was measured. The measuring frequency of the devices was approximately 2 Hz. The resistance R was calculated following Equation (3.5):

$$U = RI \tag{3.5}$$

using the applied voltage U and measured current I.

Capacitance Measurements

Electrical capacitance was measured with a four-wire setup using a Peaktech® P 2170 LCR meter (PeakTech Prüf- und Messtechnik GmbH, Germany). The measuring frequency was 10 kHz, and the sampling frequency was 2 Hz. In a sensitivity study between 100 Hz and 100 kHz, using the relevant specimens, the measuring frequency of 10 kHz achieved the best compromise between high sensitivity and low scattering of the measurement signal compared to all measuring frequencies possible with the Peaktech® P 2170 LCR meter. To minimise the influence of external factors on the capacitance measurements, the cables of the measuring device were secured against movement.

3.3.3 Digital Image Correlation

To measure the three-dimensional deformation of the specimens during loading, digital image correlation (DIC) was used during some tests. Measurements were taken with an ARAMIS 4M DIC system (GOM GmbH, Germany) in stereoscopic setup with 50 mm or 100 mm objectives. To enable calculation of the three-dimensional displacements with the ARAMIS Professional 2016 software, a random, high contrast speckle pattern was applied to the specimens before testing, using satin Dupli-Color Platinum spray paint in white (RAL 9010) and black (RAL9005).

3.3.4 Micro-sections

As preparation for microscopic evaluation of the microstructure of failed and intact specimens, the samples were embedded into the thermoset compound KEM 15 plus (ATM Qness GmbH, Germany). Afterwards, the surface was polished using an automatic Saphir 550 polishing table (ATM Qness GmbH, Germany). Three polishing steps were performed using sandpaper with 320, 800, and 2500 grit. Then, the samples were polished with diamond suspension with 9 µm, 6 µm, 3 µm, and 1 µm. The specimens were cleaned in an ultrasonic bath for 7 minutes between each polishing step.

3.3.5 Light Microscopy

Quality assurance and investigations of micro-sections were performed using a VHX-6500 digital microscope (Keyence Corporation, Japan).

4 Integrated Epoxy CNT Films

A precise knowledge of the strain state of composite materials during loading offers valuable insights into the material and damage state, which allows for safer use of composite structures. Compared to traditional, surface-mounted strain gauges, integrated sensors are less exposed to environmental influences and can provide information about local effects. However, many integrated sensors act as foreign bodies inside the material and negatively influence the mechanical properties or require extensive manufacturing efforts. The investigations on fully-integrated CNT/epoxy sensor films presented within this chapter aim to provide a solution to this problem. The following research hypothesis governs the investigations:

The local matrix modification with fully-integrated sensor films allows strain and damage monitoring in GFRPs by electrical measurements.

At first, the manufacturing and embedding process of the partially pre-cured CNT/epoxy resin films in GFRPs is described. Afterwards, the suitability of the films as integrated sensors in GFRPs is validated. Therefore, the films' influence on the mechanical properties is investigated for various lay-ups and loading scenarios. Furthermore, the sensor's ability to measure strain and damage behaviour during load application is monitored and evaluated.

4.1 Materials and Experimental Setup

4.1.1 Manufacturing of CNT/Epoxy Films

At first, a masterbatch of 1 wt.% OCSiAl Tuball™ CNTs and EPIKOTE™ Resin MGS™ RIMR 135 was manufactured using an 80E Plus three-roll mill (EXAKT Advanced Technologies, Germany). The same resin system was used for the films and the surrounding composite matrix to achieve good chemical bonding. The

process parameters of the three-roll mill process are given in Table 4.1. A more detailed description of the process is given by Meeuw et al. [145, 176]. The desired filler content of 0.5 wt.% CNTs in the films was adjusted by mixing the masterbatch with the required amounts of EPIKOTE™ Resin MGS™ RIMR 135 and EPIKURE™ Curing Agent MGS™ RIMH 137. The weight ratio of resin and curing agent was 100:30, as defined by the manufacturer. The filler content of 0.5 wt.% was found in pre-tests and provided a good processing behaviour and a reasonable absolute resistance range for low-cost measuring systems. The materials were premixed using a wooden spatula, and final mixing was performed at 3000 min^{-1} for 3 minutes using a speed mixer™ DAC 150.1 FVZ (Hauschild GmbH & Co. KG, Germany).

Table 4.1: Process parameters of three roll mill during masterbatch manufacturing

Step	Back gap	Front gap	Speed
1	120 µm	40 µm	300 min^{-1}
2	40 µm	13 µm	300 min^{-1}
3-7	13 µm	5 µm	300 min^{-1}

Films were manufactured with a thickness of 6 mils (152.4 µm) using a manual square film applicator BYK 5358 (BYK-Gardner GmbH, Germany) on a polished steel plate covered in Polytetrafluoroethylene (PTFE) foil. Prior to integration in GFRP plates, the films were cured under lab conditions at room temperature for pre-curing times between 18 h and four weeks.

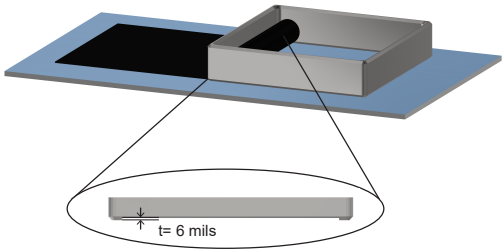

Figure 4.1: Schematic of manual film application process

4.1.2 Manufacturing of GFRP Plate and Specimens

Before placing, the pre-cured CNT films were removed from the PTFE foil, and the films were cut to the desired, specimen specific shapes. While stacking the dry glass fibre fabrics, the CNT films were placed in the desired locations (shown in Figure 4.2). Laminates with UD and CP lay-ups (compare Table 4.2) were manufactured using UT-E250 UD non-crimp glass fibre fabrics. For OHT tests, a quasi-isotropic (QI) lay-up (compare Table 4.2) was set up from bidiagonal ±45° glass fibre fabric B320E-H and UD glass fibre fabric UVE 926. Bending specimens with films placed over the lowest glass fibre fabric, in the symmetry plane, and directly under the upper fabric were manufactured, as stated in Table 4.2. In the ILSS and tensile/fatigue specimens, the films were only placed in the symmetry plane. Three configurations of $[\pm 45_2/90/0]_s$ OHT film specimens were manufactured - including films between the ±45°-layer and the 90°-layer, between the 90°-layer and the 0°-layer, and in the middle of the laminate between the 0°-plies. The infusion was performed according to the standard process described in Section 3.2.1. The holes in the OHT specimen were milled using a EuroMod®-MP CNC mill (Isel Germany AG, Germany) with a 1.8 mm diamond milling head. The specimens were contacted as described in Section 3.2. The contacting positions for each specimen setup are shown in Figure 4.2. Furthermore, the edges of some tensile samples were painted with a speckle pattern for DIC measurements as described in Section 3.3.3.

Table 4.2: Lay-ups and film positions of GFRP specimens

Test	Lay-up	Film position
ILSS	UD: $[0_{16}]$	Middle
Bending	UD: $[0_{10}]$ CP: $[0/90_4/0]_s$	Middle, Under top ply Over bottom ply
Tensile	UD: $[0_{10}]$ CP: $[0/90_4]_s$	Middle
OHT	QI: $[\pm 45_2/90/0]_s$	Between ±45° and 90° Between 90° and 0° Middle

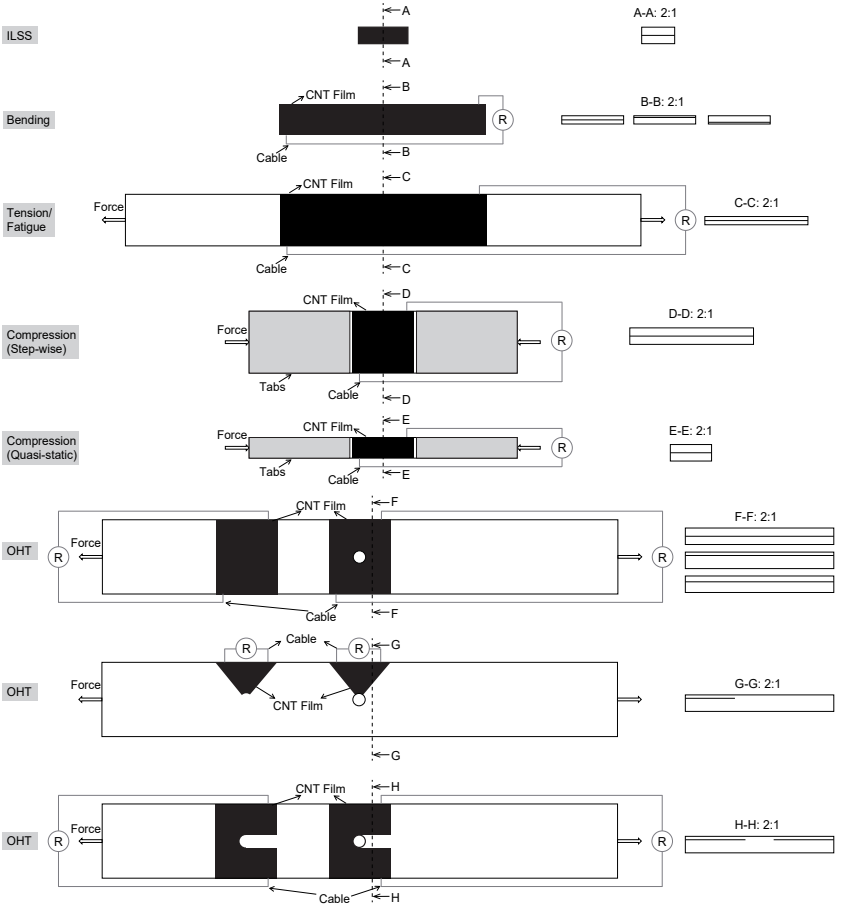

Figure 4.2: Schematic representation of specimens (from top to bottom: ILSS, bending, tension/fatigue, compression, and OHT) including film and contacting positions

4.1.3 Manufacturing of Stringers

The stringers were manufactured in an open-mould vacuum infusion process. Therefore, pre-cut layers of bidiagonal ±45° glass fibre fabric B320E-H and UD UT-E250 non-crimp glass fibre fabric were stacked as $[\pm 45/0_3]_s$ lay-up on a polished aluminium positive mould. Before stacking, the mould was treated with Mikon® W-64+ (Münch Chemie International GmbH, Germany) release

agent. Films were integrated under the top ±45°-layer. A vacuum bag was built to apply vacuum during the infusion process. Curing took place for 48 h under lab conditions. Post-curing was performed for 16 h at 80 °C in an oven. As a backing plate, a 2 mm thick plate with $[0_2/90/0_2]_s$ lay-up was manufactured from UT-E250 fabrics with the standard process described in Section 3.2.1. After post-curing, the stringer and backing plate were cut to a size of 245x127 mm^2 using an F45 ProDrive saw (Wilhelm Altendorf GmbH & Co. KG, Germany) with a diamond blade. The backing plate and the stringer were adhesively bonded using the two-component adhesive UHU® Endfest 300. Prior to the application of the adhesive, the respective areas were sanded using sanding paper with 600 grit and cleaned using isopropanol. The adhesive was cured in an oven at 60 °C for 60 min. Next, the edges were ground to be flat and right-angled. As load introduction elements, the ends of the stringer were cast 30 mm deep in epoxy resin. For this purpose, the ends of the stringers were ground and cleaned using isopropanol, and the stringer was aligned straight in a wooden mould prepared with PTFE foil. For the infusion and the casting of the load introduction elements, EPIKOTE™ Resin MGS™ RIMR 135 and EPIKURE™ Curing Agent MGS™ RIMH 137 was used. The flat backplate was painted with a random speckle pattern for DIC as described in Section 3.3.3.

Figure 4.3: Photographs of reference stringer specimen without integrated film sensors

Figure 4.3 shows photographs of the reference stringer manufactured from neat GFRP without integrated film sensors. A schematic representation of the stringer, including film sensors and contacting positions, is shown in Figure 4.4.

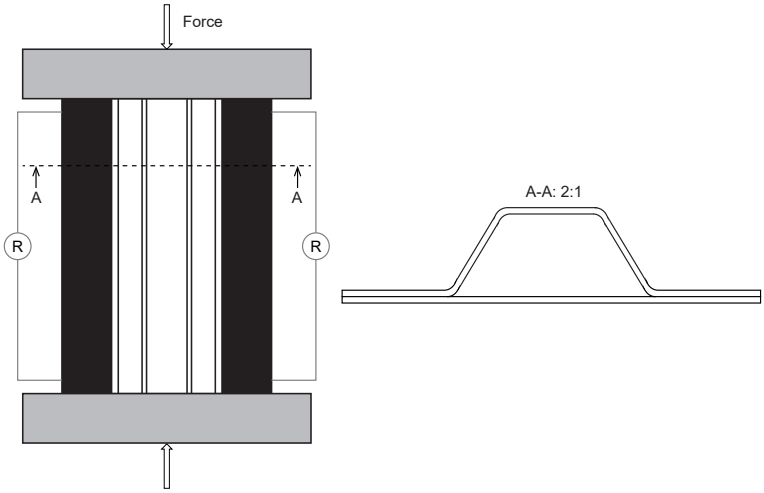

Figure 4.4: Schematic representation of stringer specimen including CNT/epoxy film sensors and contacting positions

4.1.4 Test Setup

Quasi-static tests until final failure and force-controlled step-wise tests for tensile and bending loads were carried out on UD and CP specimens following the procedures described in Section 3.3.1. Table 4.3 includes the force levels of the force-controlled step-wise tests. Furthermore, quasi-static OHT tests until final failure were conducted. The strain during the tensile tests was measured using a multiXtens contact extensometer. During some tensile tests, the local strain distribution was monitored on the specimens' edge using an ARAMIS 4M DIC system. For crack counting in CP tensile specimens, no speckle pattern was applied. Instead, only one camera of the DIC system was used for recording the specimens using backlighting with an LED. The OHT tests were performed following ASTM D5766 [175]. The local strain distribution in the OHT samples was monitored with DIC. During all tests of specimens including CNT films, the in-situ electrical resistance was measured. The resistance measurements on

bending, tensile and compression specimens were performed using a Keithley 2601A. A constant voltage of 1 V was applied, and the current was measured. In OHT tests, the resistance change was similarly evaluated using a two-channel Keithley 2602 for simultaneous measurements of two films included in the same specimen. One film was placed directly around the hole, and the other film was integrated in the near field - close to the clamping area furthest away from the hole, as depicted in Figure 4.2.

Table 4.3: Force levels during force-controlled step-wise tests for unidirectional (UD) and cross-ply (CP) specimens

Step	**Bending**		**Compression**	**Tension**	
	UD	CP	UD	UD	CP
1	40 N	40 N	10000 N	5000 N	2600 N
2	150 N	100 N	20000 N	10000 N	3000 N
3	250 N	150 N	30000 N	15000 N	3400 N
4	350 N	200 N	35000 N	25000 N	4000 N
5	450 N	250 N		35000 N	6800 N
6	550 N	300 N			

Crippling tests were performed on the stringers. Therefore, the stringers were tested under quasi-static compression with a speed of 0.25 $\mathrm{mm\,min^{-1}}$ until final failure on a Z400 universal test machine. The displacement of the flat backplate was monitored using an ARAMIS 4M DIC system. Like for the OHT specimens, a two-channel Keithley 2602 was used for simultaneous resistance measurements on two integrated CNT/epoxy film sensors.

4.2 Results and Discussion

4.2.1 Micrographs of Integrated Films

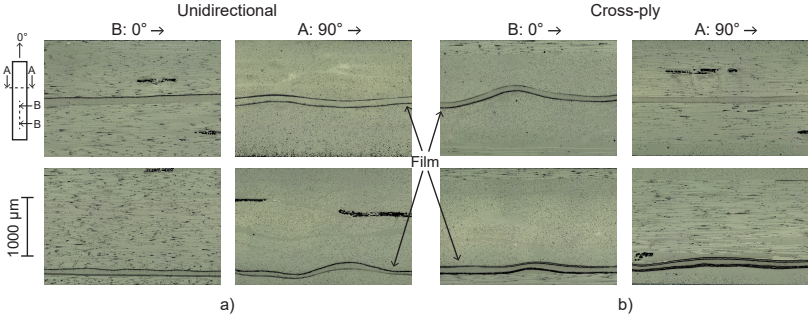

Figure 4.5: Micrographs of a) UD specimens (left: parallel to the 0°-fibre direction, right: transverse to the 0°-fibre direction, upper: film in the middle of the laminate, lower: film over the lower ply) and b) CP specimens (left: parallel to the 0°-fibre direction, right: transverse to the 0°-fibre direction, upper: film in the middle of the laminate, lower: film over the lower layer)

Figure 4.5 shows micrographs of undamaged UD and CP specimens with films in the middle of the laminate and over the lower ply (similar to those under the upper ply). Micrographs for two cutting directions are depicted for each configuration - parallel and transverse to the 0°-fibres. For all configurations, the films in specimens cut parallel to the fibre direction of the upper and lower film surrounding plies are straight. Looking at an edge oriented transverse to the surrounding layers' fibre direction, the films have a certain waviness. The waviness results from the adaption of the films to the fibre bundles of the dry glass fibre fabrics during vacuum infusion. Due to the adaption to the structure of the glass fibre fabric, no resin-rich regions are present directly at the films. The dark areas in the micrographs show the stitching yarns. During the discussion of the results, the influence of the waviness on the mechanical properties and sensing capabilities will be analysed.

4.2.2 Interlaminar Shear Strength Tests

An evaluation of different curing times of the films before integration in laminates was performed considering ease of handling during manufacturing and ILSS. The

tested pre-curing times varied between 18.5 and 21.5 h, two days, one week, two weeks, three weeks, and four weeks. Table 4.4 shows the evaluation of handling during manufacturing. For a pre-curing time of less than 18.5 h, the films were still tacky and therefore, removing the PTFE foil was not possible. The films had a good adhesion with the dry fibres after a pre-curing time between 18.5 and 21.5 h, but removing the PTFE foil required much attention and cooling the film with an icepack. Afterwards, the films have no adhesion to the dry fibres but can easily be removed from the PTFE foil. Thus, pre-curing times of more than 21.5 h result in the easiest handling which is beneficial for process automation.

Table 4.4: Pre-curing times of CNT/epoxy film sensors before integration

Time	Curing state
1-18.5 h	Adhesion to fibres: very strong Adhesion to PTFE foil: not removable
18.5-21.5 h	Adhesion to fibres: strong Adhesion to PTFE foil: removable only with icepack
From 21.5 h	Adhesion to fibres: no adhesion Adhesion to PTFE foil: easily removable

The second important factor for choosing a pre-curing time is impact on the composites' ILSS. Figure 4.6 shows a box plot of the ILSS of neat GFRP specimens and specimens with CNT/epoxy films centrally integrated after different pre-curing times. The ILSS of neat GFRP specimens and the GFRP specimens with integrated CNT films are similar up to a pre-curing time of two days. Here, the standard deviations fully overlap, and no significant difference is visible. The box plots show the median of the test values as horizontal lines, while the numbers resemble the decrease of the average value. Compared with neat GFRP samples, the average ILSS of the film specimens after a pre-curing time of 48 h is marginally lower (-0.88 %). The failure behaviour of representative specimens is shown in Figure 4.7. The neat GFRP specimens fail with delaminations in the laminate's midplane starting at the indention of the upper roller. The delaminations do not reach the end of the specimen. The failure behaviour of all specimens with pre-curing times of less than one week does not reveal any delaminations directly at the CNT film, similar to the behaviour for a specimen with a pre-curing time of 48 h shown in Figure 4.7b). The delaminations occur

cohesively, slightly above the film inside the GFRP, proving a sufficient bonding between the pre-cured CNT/epoxy films and the surrounding matrix material. Specimens with film pre-curing times of one, three, and four weeks show a significantly lower average ILSS (one week: −22.53%, three weeks: −15.78% and four weeks: −22.98%) than neat GFRP. The ILSS's scatter is high for specimens with films integrated after three or four weeks. Some specimens have ILSS in the range of neat GFRPs' scatter, and others show a large loss of ILSS. No correlation is possible between manufacturing and strength loss, as some specimens from the same film show high and others low ILSS. Specimens with a pre-curing time of two weeks before integrating the films show high strengths in the range of neat GFRP specimens and a small scatter. However, the smallest number of specimens was tested for this configuration.

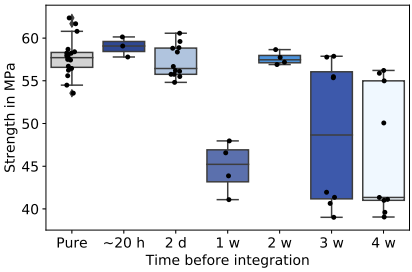

Figure 4.6: Box plot including results of ILSS tests on neat GFRP and specimens with CNT film integrated after different pre-curing times (approx. 20 h, 2 days, 1 week, 2 weeks, 3 weeks, 4 weeks) in the middle plane

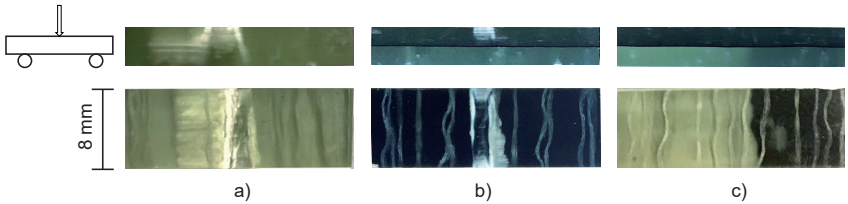

Figure 4.7: Photographs of representative ILSS specimen from the side and top or bottom - a) neat GFRP specimen, b) GFRP specimen with film integrated after 48 h pre-curing, and c) GFRP specimen with film integrated after 3 weeks pre-curing resulting in a lower ILSS

Considering the large scatter for pre-integration times of three and four weeks and the low strength for a pre-curing time of one week, it can be assumed that a higher number of samples could also result in lower strengths after two weeks of pre-curing. The failure behaviour of the specimens with lower strength changes drastically. As shown in Figure 4.7c), specimens with high pre-curing times and low strength show large delaminations starting in the specimens' middle and spanning until one end. The delamination occurs adhesively, directly at the film proving an insufficient bonding between the film and the surrounding epoxy matrix.

A pre-curing time of 48 h at room temperature before integration was chosen for all further experiments. 48 h pre-curing allow for easy, automated manufacturing on an industrial scale without significant influence on the ILSS. The scatter of the strength is in the same order of magnitude as neat GFRP specimens' strength, and the specimens show a reproducible failure behaviour. The films can easily be removed from the PTFE foil, cut to the desired shapes and placed on the dry glass fibre fabrics.

4.2.3 Three-point Bending Tests

In three-point bending specimens, the films were placed under the top ply, in the middle of the laminate and over the bottom ply - theoretically resulting in three different local stress scenarios as schematically shown in Figure 4.8. Placing the CNT sensors above the lowest ply result in tensile and below the top ply in compressive loads inside the films. When perfectly integrating the films in the middle and therefore in the neutral axis, theoretically, only shear is applied to the films, and no volume change occurs.

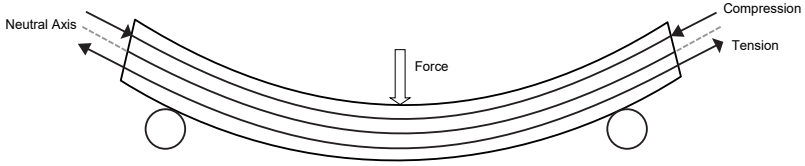

Figure 4.8: Schematic representation of loading in three-point bending specimen - top film: compression, middle film: neutral axis, bottom film: tension

The influence of the integrated films on bending strength and modulus in comparison with neat GFRP UD bending specimens is shown in the boxplot in Figure 4.9. The horizontal lines resemble the medians, while the numbers describe the change of the average values. The average strength values decrease slightly for the UD specimens with films under the upper (-2.72%) and over the lower ply (-2.92%), while the average modulus values increase slightly (upper: $+1.16\%$, lower: $+1.11\%$). However, as the results of the specimens with films under the upper and over the lower ply lie within the standard deviation of the results for neat UD GFRP specimens, the slight changes are not significant. A significant increase of strength ($+8.16\%$) and modulus ($+13.27\%$) is visible for the UD bending specimens with films integrated in the middle plane. In this case, all 0°-plies are pushed further out relative to the centre plane of the laminate, leading to a higher bending stiffness. The trend is also visible for the upper and lower case, where the modulus increase is smaller. In this case, only one single 0°-ply is pushed further outwards, leading to a small, not significant increase of the modulus.

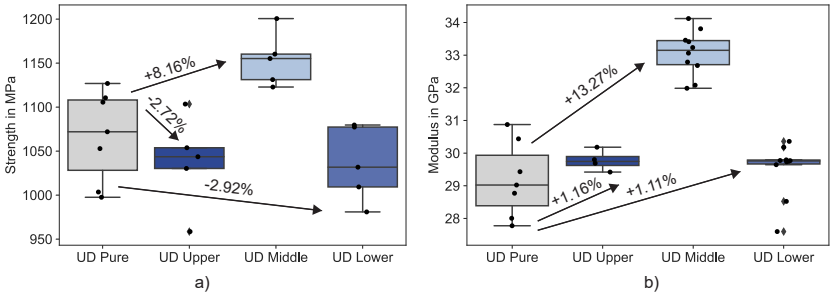

Figure 4.9: Box plot including results of bending tests on UD neat GFRP and specimens with CNT film in different layers and percent change of the average value - a) strength, b) modulus

Figure 4.10 shows the results of quasi-static three-point bending tests until failure and step-wise three-point bending tests for representative UD specimens with films under the upper ply, including stress and resistance change curves. The electrical resistance change ΔR in percent is calculated according to Equation (4.1) with the initial resistance R_0 and the current resistance R.

$$\Delta R = \frac{R - R_0}{R_0} 100 \tag{4.1}$$

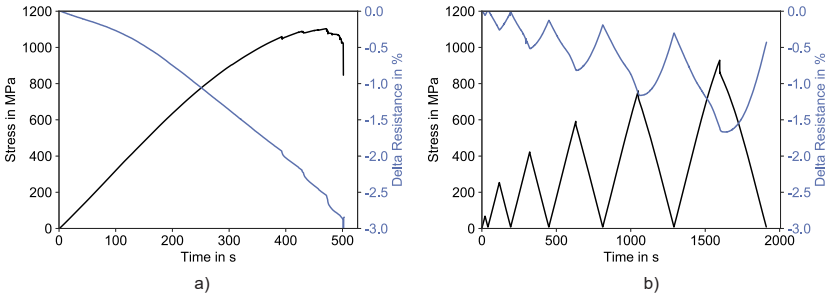

Figure 4.10: Representative results of a) quasi-static and b) step-wise three-point bending tests on UD specimens with films under the upper ply, including stress and resistance change

The resistance change is negative throughout the entire bending test. At first, the resistance decrease has a lower slope, and after the initial phase, the slope increases. Shortly before the final failure, small steps in the resistance change are visible, resembling steps in the stress curve due to the failure of the first fibre bundles. The resistance change at final failure has an average value of $-2.72 \pm 0.31\%$. During step-wise tests, the same stress-anti-proportional resistance change is measurable, resulting in decreasing resistance during loading and increasing resistance during unloading. Up to 250 MPa, the resistance change is fully reversible during unloading. Afterwards, the irreversibility of the resistance change increases with higher stresses. When comparing the quasi-static and step-wise curves, it is evident that similar loads lead to similar resistance changes. Furthermore, the stresses leading to fully reversible resistance changes in step-wise tests are in the same range as the stresses before the slope transition towards the higher slope of the resistance change at the beginning of the quasi-static tests. The decreasing resistance is a consequence of the compressive loading state above the midplane of the laminate. The piezoresistive effect is known for CNT polymer composites and results from their heterogeneous structure (see Section 2.2.3). A compressive strain leads to a reduction of the tunnelling resistance or the formation of new conductive paths inside the CNT films as CNTs are moved closer together [46, 116, 159, 160]. The irreversibility of the resistance change is caused by irreversible changes in the CNT network, as not all of the formed paths are dissolved. One reason might be the visible indention due to the upper roller that leads to local compression of the film. Overall, however, pre-

dicting the applied stress or strain is possible via the measured resistance change.

Representative results for UD bending specimens with films in the middle are presented in Figure 4.11. In theory, the middle film lies in the neutral axis of the specimens and therefore only exposed to shear. In the ideal case, no volumetric change of the film is expected. Consequently, the influence on the CNT network and the resulting resistance change is expected to be minimal. The magnitude of the resistance change at final failure ($-0.73 \pm 0.14\%$) is smaller than in the films under the upper and above the lower ply. However, a small resistance change is still measurable. The films have a certain thickness, a slight deviation to the neutral axis due to the manufacturing process, and a waviness transverse to the surrounding fibres' direction, as can be seen in the micrographs in Figure 4.5. These effects lead to small resistance changes and influence the shape of the curve. The resistance change at the beginning of the quasi-static tests is small. During the test, the slope becomes more negative, resulting in a linear decrease. As visible in the representative resistance curve for the step-wise tests, a mixed positive and negative behaviour occurs during the test. The point at which the behaviour reverses is slightly different for all samples, but qualitatively the curves are similar. The changes are very small in terms of magnitude, making the curves appear more jagged than for the upper and lower film sensors. The mixed behaviour is likely caused by a change of tensile and compressive local stresses inside the film due to slight deviation to the neutral axis. Possibly the waviness leads to specimens with parts of the film being slightly above and other bits being slightly below the neutral axis.

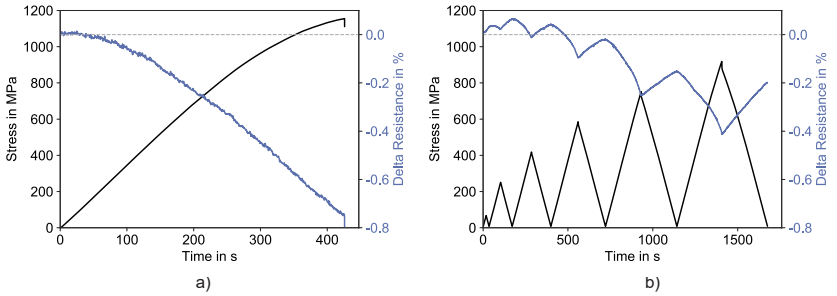

Figure 4.11: Representative results of a) quasi-static and b) step-wise three-point bending tests on UD specimens with films in the middle, including stress and resistance change

As depicted in Figure 4.12, films integrated over the lower ply of UD bending specimens show a resistance increase during loading. The resistance increase is in very good agreement with the applied stress following all observable trends in the stress curve. As a consequence of the tensile strain, conductive paths within the films dissolve because CNTs move apart that were previously very close or in contact (see Section 2.2.3). This reduction of the conductive paths leads to a resistance increase. The measured resistance change at final failure has a magnitude of $2.31 \pm 0.17\%$ and has a similar absolute value as the resistance decrease measured in specimens with films under the upper ply. Step-wise tests show full reversibility of the resistance change up to 600 MPa. The reversible region corresponds with the linear region of the stress curve in the quasi-static tests. For unloading after exposure to higher stresses, the resistance change reaches a slightly negative value in the unloaded state at zero stress indicating more conductive paths inside the CNT film than at the beginning of the test.

In summary of the UD bending tests, the low standard deviations in resistance change before final failure show that the manufacturing process of the integrated CNT film sensors is not only easy and automatable but also generates reproducible results even for specimens manufactured in different plates using several, separately produced films. In the bending tests on UD GFRP composites with films under the upper or over the lower ply, knowledge of the strength and resistance change at failure allows setting a threshold value that must not be exceeded to ensure a safe and reliable operation. The threshold should take into account the design specifications and allowable stresses in the material and could for example be set at the end of the fully elastic regime.

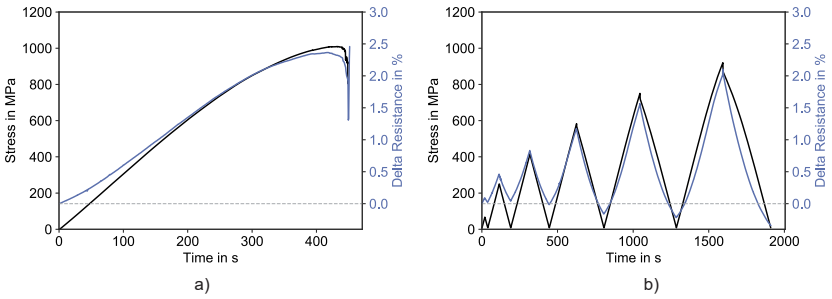

Figure 4.12: Representative results of a) quasi-static and b) step-wise three-point bending tests on UD specimens with films over the lower ply, including stress and resistance change

Similar tests have been performed on CP specimens. Median strength and modulus of the CP bending specimens increase for all configurations including CNT films compared to neat GFRP specimens, as shown by the horizontal lines in the box plot in Figure 4.13. The standard deviations of the strength values overlap for all configurations. Nevertheless, the average values increase (depicted as numbers in the figure) is significant. An average strength increase of 4.72% is measured for the CP specimens with films under the upper layer. The lowest average strength increase (+2.89%) is measured for the specimens with film in the middle, and the highest average strength increase of 9.46% for specimens with films integrated over the lower layer. The average modulus increase is more significant as there is almost no overlap of the standard deviations (+8.25% for upper films, +7.24% for films in the middle, and +4.58% for films integrated over the lower layer). The median value for lower films is higher than for middle films, but the average values show an opposite trend.

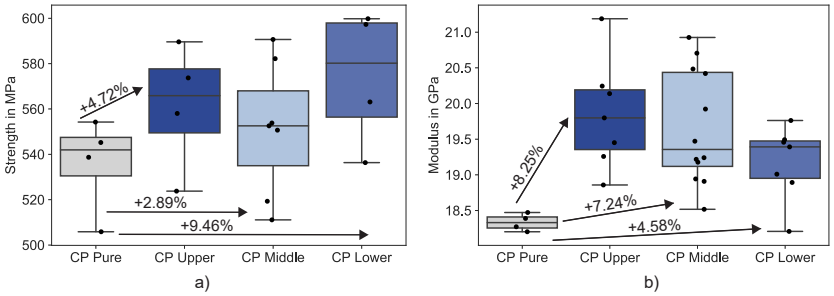

Figure 4.13: Box plot including results of bending tests on CP neat GFRP and specimens with CNT film in different layers - a) strength, b) modulus

The stress and resistance curves of representative CP specimens shown in Figures 4.14, 4.15, and 4.16 qualitatively show similar trends as the UD specimens. Therefore, the description is less detailed.

A local compressive strain inside the film under the upper layer leads to a negative resistance change (see Figure 4.14). The average maximum resistance change before final failure is $-1.33 \pm 0.06\%$ and therefore approximately half of the measured resistance change in the UD bending specimens with films under the upper layer. The strength of the specimen is also approximately half of the UD specimens' strength. Full reversibility of the resistance change is given up to around 300 MPa, which resembles the entirely linear region of the quasi-static stress-

time curve and the part of the resistance change curve with the initial slope. Some irreversible deformation is present in the specimens and films for higher stresses.

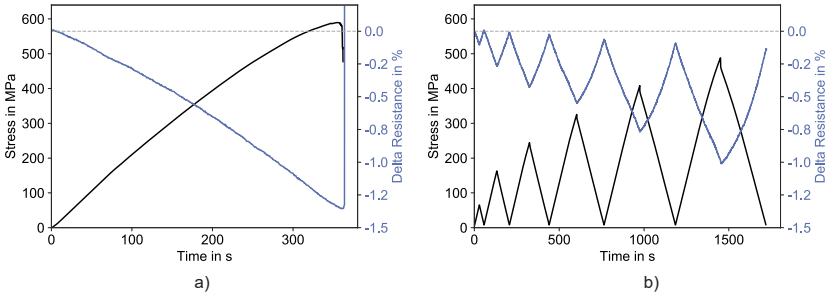

Figure 4.14: Representative results of a) quasi-static and b) step-wise three-point bending tests on CP specimens with films under the upper layer, including stress and resistance change

Nearly no resistance change is measurable for CP specimens with the film in the middle (see Figure 4.15). The maximum resistance change is $0.12 \pm 0.04\%$. The noticeable noise in the measurement is a scaling effect and only appears because of the small scale. The resistance increases linearly until the stress curve flattens at around 300 MPa. Then, the resistance change also starts to flatten and decreases. Similar behaviour is visible in the step-wise tests. In the beginning, the resistance increases without clear evidence of the unloading. For higher stresses, the steps become more pronounced, and the maxima of the resistance change correspond to the maxima of the stress as for films with local tensile stress. The resistance change stays positive during unloading. Only during the final unloading, the initial resistance is reached, and at the end of the unloading, the resistance is lower than in the beginning. As in the UD specimens, the change between increasing and decreasing trends can be attributed to changing local stresses inside the film due to deviations to the neutral axis. However, the changes are small and neglectable as the scaling of the resistance change-axis shows.

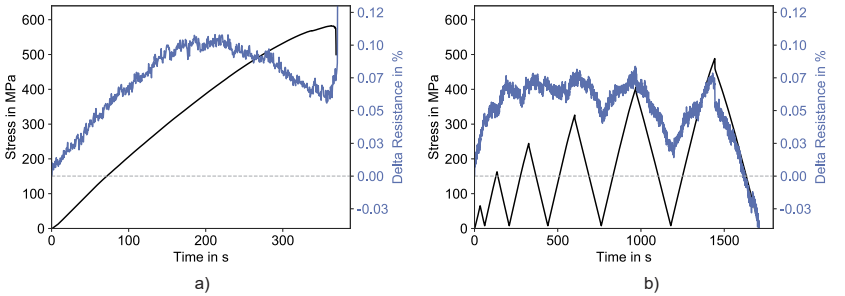

Figure 4.15: Representative results of a) quasi-static and b) step-wise three-point bending tests on CP specimens with films in the middle, including stress and resistance change

Resistance change in films over the lower layer of CP specimens shows an excellent agreement with the stress (see Figure 4.16). Step-wise tests reveal a nearly fully reversible resistance change up to the highest load step. Unlike in the UD samples, no drop below the initial resistance is detectable when the CP specimens are fully unloaded. Therefore, a correlation between applied stress and measured resistance change is feasible. The waviness of the films in the lengthwise direction of the CP bending specimens does not have a noticeable influence on the resistance change.

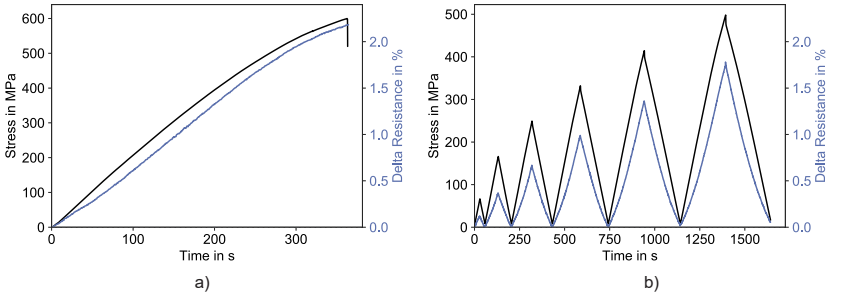

Figure 4.16: Representative results of a) quasi-static and b) step-wise three-point bending tests on CP specimens with films over the lower layer, including stress and resistance change

In summary, the three-point bending tests on UD and CP specimens show that localised strain monitoring inside GFRP structures is obtainable by inserting the

CNT films in different positions. Local compressive (film under the upper layer) and tensile (film over the lower layer) stresses can be detected and monitored by negative and positive resistance changes using the piezoresistive effect of the CNT films. A correlation between stress or strain and resistance change is possible and reproducible for upper and lower films, as the comparison between different specimens as well as quasi-static and step-wise tests shows. However, films in the middle layer show small, mixed-mode resistance changes resulting from deviations to the neutral axis due to the film's placement, thickness and waviness. Due to the mixed-mode nature, a certain resistance change cannot clearly be attributed to a specific stress. Mechanically, integration of the film sensors in bending specimens has no significant or, in many cases, even a beneficial effect. The integrated films increase strength and modulus for all CP configurations and for UD specimens with middle films. The strength and modulus of UD specimens with upper and lower films do not show a significant change as they are within the standard deviation of the neat GFRP specimens.

4.2.4 Compression Tests

Figure 4.17 shows representative results of quasi-static and step-wise compression tests on UD specimens, including strain and resistance change. The quasi-static compression tests show a linear stress-time behaviour with a slight slope decrease from 10 seconds onwards. In the beginning, the resistance change curve is decreasing linearly due to a negative piezoresistive effect as expected and observed for UD three-point bending specimens with the film under the upper layer.

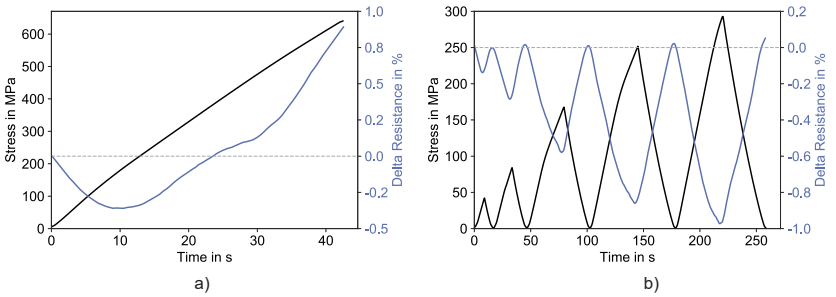

Figure 4.17: Representative results of a) quasi-static and b) step-wise compression tests on UD specimens, including stress and resistance change

After 10 seconds, the resistance starts to increase. The increase correlates with the slight change of slope observable in the stress-time curve and can be attributed to buckling of the sample that was observable during the test. Due to the buckling, the film is no longer subjected to a pure compressive load. The results of the bending samples show that bending can lead to a tensile load on the film, which explains the increase of resistance. The compression specimens were tested in a shear loading setup without end loading. The specimen geometry of 130x30x4 mm^3 tested in step-wise tests slipped before failure in quasi-static tests. To cause failure at a lower load and prevent slipping, thinner specimens with a geometry of 130x10x4 mm^3 were tested until failure. Due to the smaller width, the specimens buckled. No buckling was observed for the wider specimens and lower loads during the step-wise tests. Over the whole course of the step-wise tests, the resistance change shows a negative piezoresistive behaviour that correlates well with the applied load. The resistance change is fully reversible during unloading. Due to the buckling, no boxplots of strength and modulus are given. However, the stress-time curves of neat and film specimens were similar. Hence, it can be concluded that the integrated films do not significantly influence the compression modulus or strength. Strain monitoring during compression tests is possible by evaluating the resistance change of the films. An unexpected resistance increase can detect an unwanted buckling of the specimens.

4.2.5 Tensile Tests

Unnotched Tensile Tests

Figure 4.18 shows box plots of tensile strength and Young's modulus of UD neat GFRP specimens and specimens including CNT/epoxy films in the middle of the laminate. The average strength of the specimens is decreasing 7.79%, while the Young's modulus is increasing 4.97%. The standard deviations slightly overlap for strength and modulus. The failure behaviour of failed neat UD GFRP specimens and specimens including films is similar. As structures often are designed concerning the modulus, the modulus increase can provide a positive design perspective considering the strength decrease.

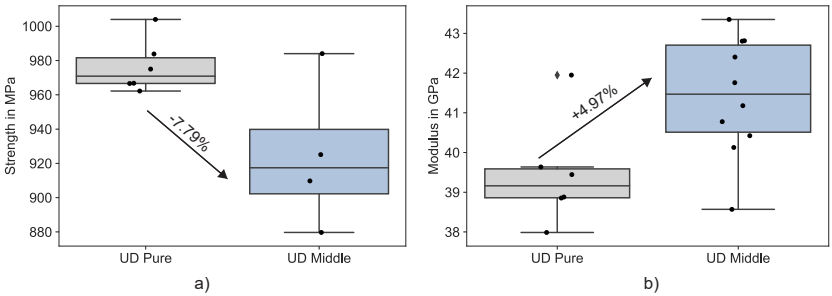

Figure 4.18: Box plot including results of tensile tests on UD neat GFRP and specimens with CNT film in the middle plane - a) strength, b) Young's modulus

Figure 4.19 presents the stress and resistance change curves of quasi-static and step-wise tensile tests on representative UD specimens. Mechanically, the specimens exhibit a linear stress increase until brittle failure. The measured resistance change inside the UD specimens' films is positive and shows an excellent agreement with the stress up to failure. Similar to the local tensile stresses in bending, the applied strain under tensile load leads to higher distances of the CNTs. Consequently, the resistance increases as conductive paths within the films dissolve. The specimens' maximum resistance change at failure is $5.71 \pm 0.65\%$. The step-wise tests reveal that the resistance change is fully reversible and follows the applied loading.

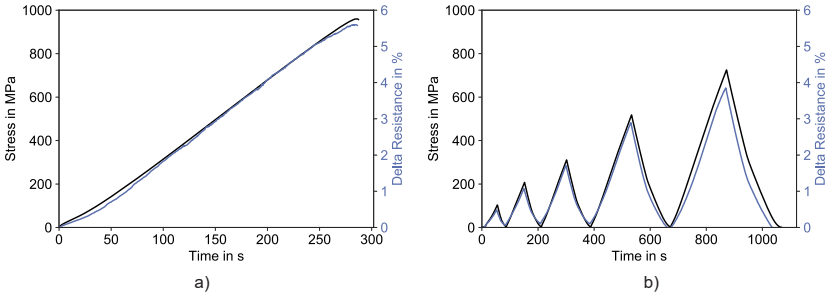

Figure 4.19: Representative results of a) quasi-static and b) step-wise tensile tests on UD specimens, including stress and resistance change

The sensitivity of the film sensors is defined by the gauge factor k as the relative change of the electrical resistance over strain according to Equation (4.2).

$$k = \frac{\Delta R}{\epsilon} \tag{4.2}$$

Similar to the Young's modulus, the gauge factor is evaluated between 0.05% and 0.25% strain. The gauge factor for the UD tensile specimens is 2.01 ± 0.1. The sensitivity is comparable with standard, commercial metal foil strain gauges [128, 130, 156, 166, 177, 178]. In literature, a range of gauge factors ranging from lower [179–181] to higher factors [166, 178, 182] have been reported for CNT sensors. In general, higher sensitivity can be obtained for filler ratios close to the percolation threshold where a small applied strain causes significant network changes [63, 130, 166, 178, 183]. However, filler ratios close to the percolation threshold may result in non-linear resistance change behaviour for a bigger strain range [156, 180]. Within this study, the filler content of 0.5 wt.% is higher than the percolation threshold, which was found between 0.02 wt.% and 0.05 wt.%. The higher filler content was chosen to result in a stable and reversible resistance change behaviour over the whole course of the performed tests. The sensors' sensitivity is suitable for the applications and tests within this work. The sensitivity optimisation was not the focus of this study. Thus, the analysis of the gauge factors is limited to the UD tensile specimens. An optimisation of the filler content regarding the conductivity, sensitivity, and measurement stability offers the potential for higher sensitivities.

For CP specimens, the average tensile strength with integrated films decreases 1.89% compared to neat GFRP and the average Young's modulus increases 4.74% (see Figure 4.20). The standard deviation of the strength overlaps with the neat GFRP specimens' results. The average modulus increase lies within the standard deviation of the neat GFRP samples. Therefore, it can be concluded that the effect of the films on tensile strength and Young's modulus of CP specimens is small and mostly neglectable.

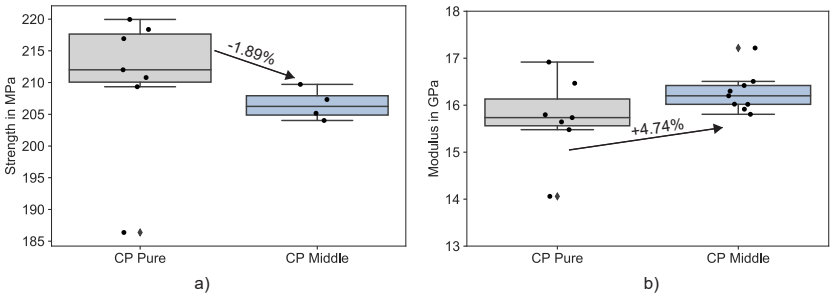

Figure 4.20: Box plot including results of tensile tests on CP neat GFRP and specimens with CNT film in the middle plane - a) strength, b) Young's modulus

Tensile tests on CP specimens (representative results see Figure 4.21) show a clear knee point in the stress curve with a stiffness decrease due to developing matrix cracks.

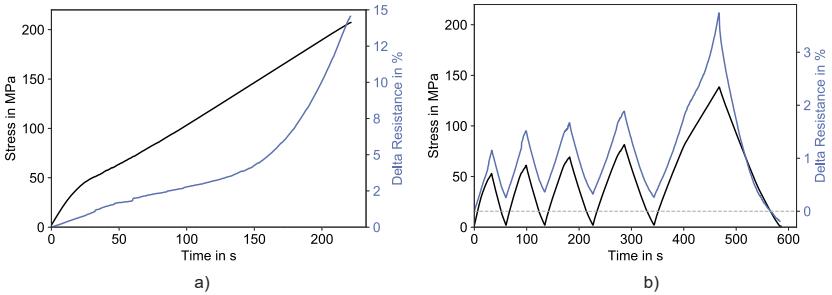

Figure 4.21: Representative results of a) quasi-static and b) step-wise tensile tests on CP specimens, including stress and resistance change

The film stays intact until final failure, and the cracks are developing on both sides of the film, as explained in further detail later. The crack spacing and failure behaviour of specimens including films and reference specimens are similar. Therefore, an in-situ crack counting in reference specimens can be seen as representative for development in film specimens.

As visible in Figure 4.22, the depicted curve of the counted cracks shows a steep increase around the knee point and slower crack development with higher strain.

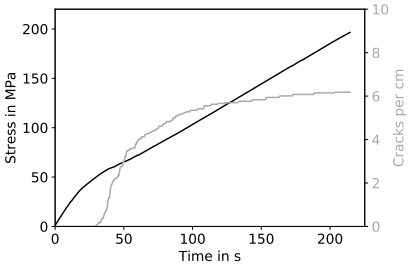

Figure 4.22: Representative crack development in CP reference specimen without integrated CNT/epoxy film sensor

The resistance change during tensile tests on CP specimens shows a three-step behaviour (see Figure 4.21). At first, there is a linear increase in resistance. The increase's slope is slightly smaller after the knee point. Towards the end, when the crack curve reaches saturation, a strong increase in resistance is visible. The resistance change at failure is 15.32±3.9% and therefore approximately 2.7 times higher than for the UD specimens. However, the global fracture strain of the specimens only shows a small deviation between UD and CP specimens (UD: $2.35 \pm 0.12\%$, CP: $2.69 \pm 0.03\%$). The non-linear resistance increase in the CP specimens as opposed to the linear increase in the UD specimens results from the different failure behaviour due to developing matrix cracks. In step-wise tests, the maxima and minima of the resistance change and stress correspond well, increasing stress leading to an increasing resistance change. The knee is visible in the stress and in the resistance change. However, during unloading, the resistance change is not fully reversible for the CP specimens, in contrast to the UD specimens, as cracks are not closing completely during unloading, which is explained in more detail using DIC images of the specimen edges. The DIC images in Figures 4.23 and 4.24 show a high increase of local strain due to the cracks, especially during crack opening towards the end of the tests.

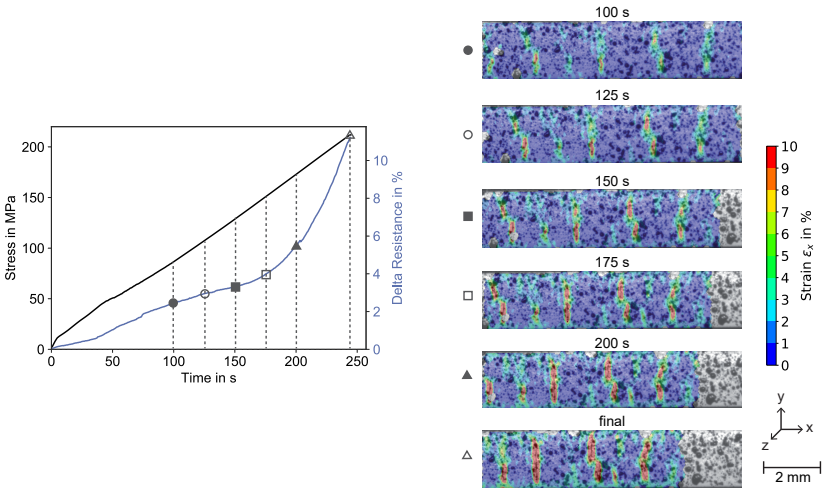

Figure 4.23: Results of a quasi-static tensile test on a CP specimen and corresponding DIC pictures for six specific time-steps

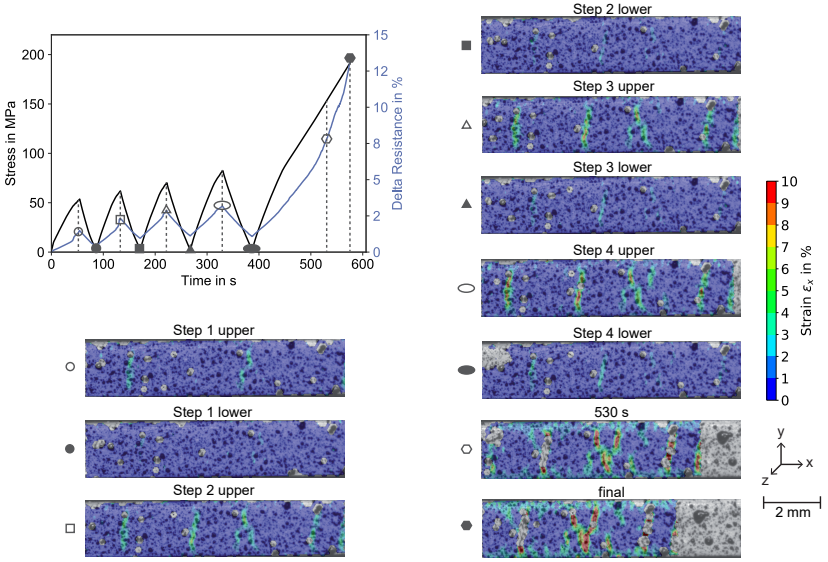

Figure 4.24: Results of a step-wise tensile test on a CP specimen and corresponding DIC pictures for ten specific time-steps

The film is located in the middle, parallel to the long edge of the image. The cracks form on both sides of the CNT film and do not span the whole thickness of the specimens. During a higher rate of crack formation, the local strains are smaller. With fewer cracks developing, the increasing stress leads to an opening of the existing cracks, and the local strains at the film increase in intensity, amount, and area. Therefore, the high resistance increase towards the end of the tensile tests on CP specimens can be attributed to high local strains in the CNT film due to crack opening. DIC of step-wise tests shows the crack development at lower stresses. At the maximum of step one, the visible section includes two cracks. During unloading, the cracks close, but some local strain remains in the cracked areas, visible as slightly turquoise areas. For comparison, the scale is the same for all images. With a re-scaling, however, the remaining strain would become more visible. After the first load step, the remaining strain is small compared to the remaining strains for further unloadings. The irreversibility of the resistance change during unloading results from the remaining local strains in the films and is influenced by the value of the remaining strain. New cracks form during the second loading step. Although some new cracks are still formed in the specimen for higher stresses, as the crack development in Figure 4.22 shows, within the depicted area, mostly the existing cracks open, and the local strains increase. A new crack develops during the fourth loading step. During the resistance's strong gain towards the end of the test, the crack opening and therefore the local strains drastically increase in many cracks.
The CP tensile tests show the films' ability to monitor local strain increases inside the specimens due to the cracks. The damage-induced local strains due to crack opening towards the end of the tensile test result in a drastic resistance increase. Therefore, a localised SHM via resistance measurements is possible. Threshold values of the resistance change can be defined for UD and CP specimens to avoid a final failure of the material.

Open-Hole Tensile Tests

Since the tensile tests on CP specimens have revealed the ability to monitor local strain peaks inside GFRPs, the films are inserted around the holes in OHT specimens. An SHM in the vicinity of holes is desired, especially in large structures, as the stress concentrations around holes promote early failure. Figure 4.25 shows the results of representative OHT specimens for each of the three tested configurations (films between the $\pm 45°$-layer and the $90°$-layer, between

the 90°-layer, and the 0°-layer and in the middle of the laminate between the 0°-plies) including stress and resistance change curves for film around the hole and in the near field.

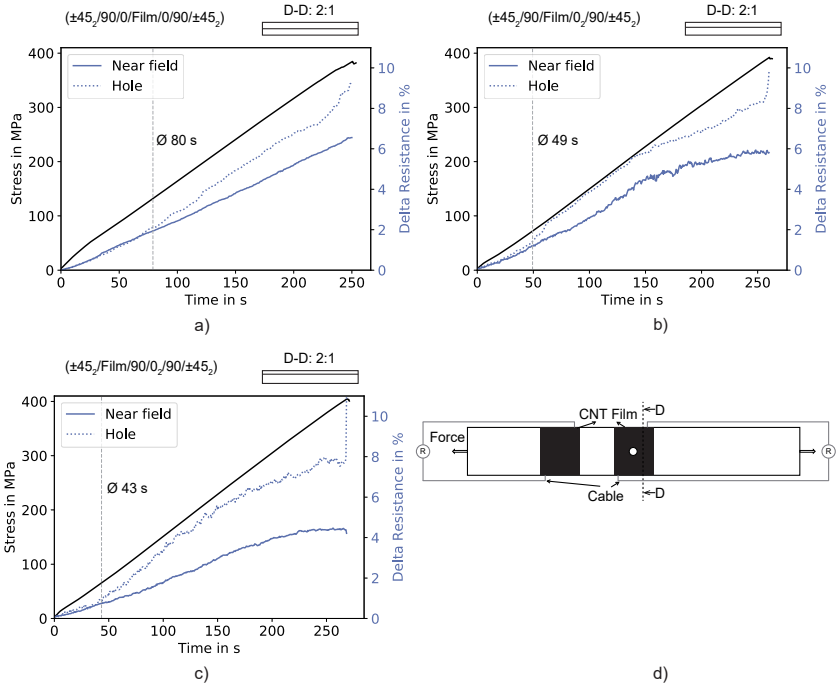

Figure 4.25: Representative results of OHT tests on quasi-isotropic GFRP specimens with CNT films in different layers - a) between 0°-plies in the middle of the laminate, b) between the 90°-layer and the 0°-layer, c) between the ±45°-layer and the 90°-layer. The resistance changes are shown for the film in the vicinity of the hole and in the near field.

All stress-time curves have a linear behaviour until sudden, brittle failure. The resistance change curves are different for the three configurations. However, for all configurations, the films at the hole exhibit a higher resistance change than the near field films. For films in the middle of the laminate between the 0°-plies, the resistance change of the near field film is linear until final failure and reaches a maximum value of $6.11 \pm 0.38\%$. Qualitatively, the course of the change in resistance is thus similar to tensile tests on UD specimens. In the beginning,

the resistance change of the film at the hole is equal to that of the near field film. In samples with film between the 0°-plies, the resistance change in the film at the hole is bigger than in the near field film from an average of 80 seconds onwards, which is also marked with the dashed line in the diagram (see Figure 4.25). After that, the resistance change of the films at the hole has a higher slope but still a mostly linear shape. Shortly before failure, a stronger increase of the resistance change at the hole is measured. The absolute value of final resistance change at the hole varies between the specimens as the strain in the film is influenced by the damage state around the hole. For films located between the 90°-layer and the 0°-layer, the resistance change in the near field is linear only at the beginning and then flattens out noticeably. The absolute maximum resistance change for the near field films is similar to that with films between the 0°-plies. However, the difference between hole and near field films' resistance changes is visible much earlier than for films between the 0°-plies. In samples with films between the 90°-layer and the 0°-layer, the film at the hole shows a larger resistance change than the near field film after an average of 49 seconds as shown with the dashed line in Figure 4.25. Although the resistance change is bigger, the resistance change's shape at the hole is qualitatively similar to that of the near field and shows the same flattening. In specimens with films between the ±45°-layer and the 90°-layer, the deviation between resistance at the hole and in the near field starts at 43 seconds (dashed line in Figure 4.25) and shows the highest deviation of all configurations. The resistance change in the near field qualitatively has a similar shape as the near field films integrated between the 90°-layer and the 0°-layer, but the maximum value is lower. The deviation between near field resistance change and resistance change at the hole is attributed to local strains around the hole. Flattening of the resistance change curve (in the case of films between the ±45°-layer and the 90°-layer as well as between the 90°-layer and the 0°-layer) shows a decrease of local strain due to local damage, e.g., in the form of delaminations. This behaviour is in agreement with the expected failure process in QI OHT samples.

Figures 4.26 and 4.27 show representative results for OHT tests with triangular- and U-shaped films. The geometries were chosen in a way that resembles the highly strained areas in the hole's vicinity, as depicted in the DIC images in Figures 4.26 and 4.27. The geometry change significantly increases the sensitivity of the measurements towards the end of the test.

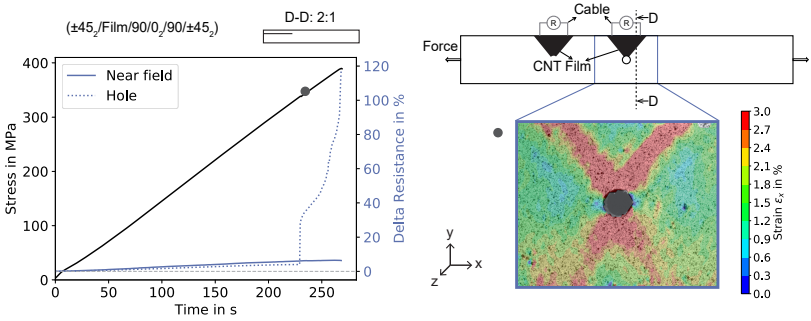

Figure 4.26: Representative results of OHT tests on quasi-isotropic GFRP specimens with triangular CNT films between the ±45°-layer and the 90°-layer. Resistance change is shown for the film in the vicinity of the hole and in the near field.

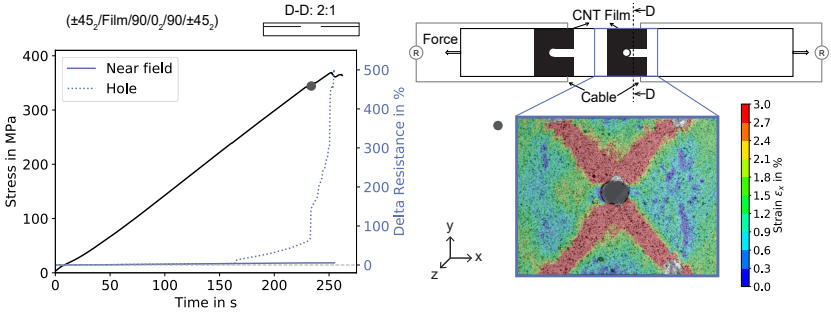

Figure 4.27: Representative results of OHT tests on quasi-isotropic GFRP specimens with U-shaped CNT films between the ±45°-layer and the 90°-layer. Resistance change is shown for the film in the vicinity of the hole and in the near field.

At the end of the test, the resistance change is at least one order of magnitude higher than for OHT specimens with square films. The U-shaped films measure the highest resistance change. The triangular-shaped films monitor a highly strained area on one side of the hole, while the U-shaped films cover the highly strained areas on both sides of the hole. Compared to the square films, the U-shaped films offer fewer alternative, small resistance current paths in lower strained areas. Before the drastic increase, the resistance change of the trian-

gular and U-shaped films is similar to the square films. The drastic resistance increase towards the end of the test allows for a more distinct definition of a resistance threshold marking a critical material state. By visual inspection no premature failure of the sensors was observed before specimen failure.
In summary, the OHT tests showed that the CNT strain sensors are able to monitor local strains around the hole in different layers, revealing valuable insights into the material's failure process. Local delaminations can be detected by a flattening of the resistance change curve. A prediction of failure using threshold resistance change values is possible. A change of the film's shape, e.g., to a triangular or U-shape resembling the highly loaded areas even better, drastically increases the sensitivity.

4.2.6 Fatigue Tests

Fatigue tests were performed to investigate the sensor performance under cyclic loads. Figure 4.28 shows a Wöhler curve of the results (black symbols) and maximum resistance changes before final failure (blue symbols). Symbols denoted with an arrow show specimens stopped after more than 10^6 cycles before failure and therefore defined as run-out specimens. Filled squares depict the results from the first laminate manufactured for this study, and unfilled circles resemble the second laminate.

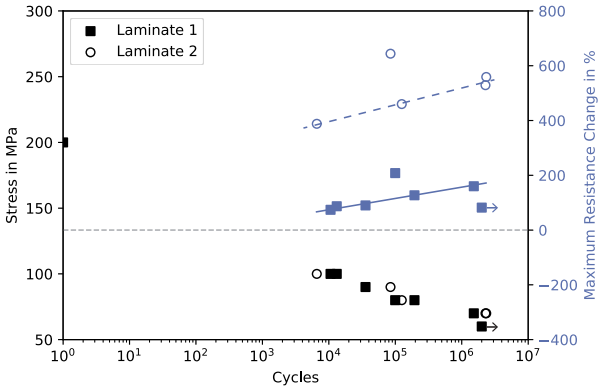

Figure 4.28: Results of fatigue tests on $[0/90_8/0]$ specimens with CNT film integrated in the middle showing stress in MPa and maximum resistance change shortly before failure in % over number of cycles

Mechanically, the two laminates behave similarly. However, the resistance change values before final failure show significant differences. While the first laminate shows final resistance changes between 74% and 208% for different load levels, the resistance changes measured for samples from the second plate vary between 388% and 644%. For all specimens, a resistance change was measurable until final failure. Thus, even under cyclical load conditions, the film sensors do not fail prematurely and enable measurements over the entire service life. The same qualitative trends are visible for the resistance changes of samples from both laminates when neglecting the absolute values. When plotted over the logarithmic number of cycles, the resistance change before failure is increasing linearly with decreasing load level and therefore increasing cycles before failure. Consequently, the highest final resistance change is measured for the lowest load level and highest lifetime. The slopes of the resistances' linear regressions are similar for both laminates. A more detailed analysis of the resistance profile during fatigue testing is given in Figure 4.29, which shows the stiffness and the resistance change for two representative samples loaded at 40% ultimate tensile strength. Each sample was taken from a different laminate - 4.29a) from laminate 1 and 4.29b) from laminate 2. The stiffness of both specimens drops throughout the test and exhibits a more drastic decrease in the beginning. The stiffness drop can be attributed to the development and growth of matrix cracks and delaminations inside the specimen. The unsteady course of the stiffness is caused by measurement inaccuracies in the stiffness measurements of the individual cycles. Nevertheless, the overall trend is visible. The resistance plots appear as filled areas since the individual cycles, as in the step-wise tensile tests, exhibit an increase in resistance during loading and a decrease during unloading. The envelopes of the maxima and minima of the resistance change have the inverse behaviour of the stiffness with a similar shape. A drop of stiffness results in an increase of maximum and likewise minimum resistance change. The trends and characteristics of stiffness and resistance change for specimens from both laminates are equal. The absolute stiffness values are similar, which corresponds to the mechanical behaviour depicted in the Wöhler curve in Figure 4.28. Therefore, the absolute values of resistance change seem to be the only observable difference in the results of the two laminates. The two laminates were manufactured from different resin batches. The second batch had a noticeably higher glass transition temperature in differential scanning calorimetry measurements, and the manufactured films were more brittle. After consultation with

the manufacturer, the behaviour could be attributed to a different reactive diluents' amount in the resin formulation of the second batch.
Concluding, the integrated CNT/epoxy sensors proved to withstand cyclic loading and did not fail prematurely before specimen failure. Resistance change can be correlated with load and overall stiffness. However, finding threshold values for critical resistance changes requires knowledge about the load level and a one-time determination of the respective critical values for each load level.

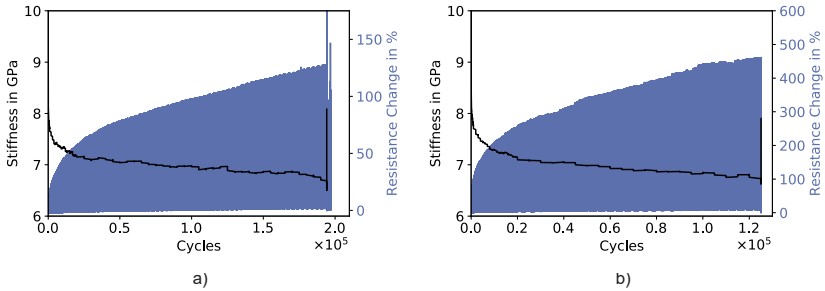

Figure 4.29: Results of fatigue tests on two $[0/90_8/0]$ specimens with CNT film integrated in the middle taken from different laminates - a) laminate 1, b) laminate 2 - showing stiffness in GPa and resistance change in % over number of cycles tested at 40% ultimate tensile strength

4.2.7 Component Test

To evaluate the behaviour of the sensors in a larger structure, crippling tests were performed on stringers as described in Section 4.1.4. The strength, modulus, and failure behaviour were similar for the stringer with two integrated CNT/epoxy sensor films and reference stringer manufactured from neat GFRP. Consequently, no significant influence of the films on mechanical performance was observed. Photographs of the failed stringer with integrated CNT/epoxy film sensors are shown in Figure 4.30. The failure behaviour consists of a wide crack that extends across the entire width of the stringer and delaminations throughout large parts of the stringer (recognisable by the slight milky discolouration). The delaminations are particularly pronounced in the vicinity of the crack. The delaminations occur in different planes and not only directly on the films as visible in the side view. In the backplate, no failure damaging the DIC paint is apparent.

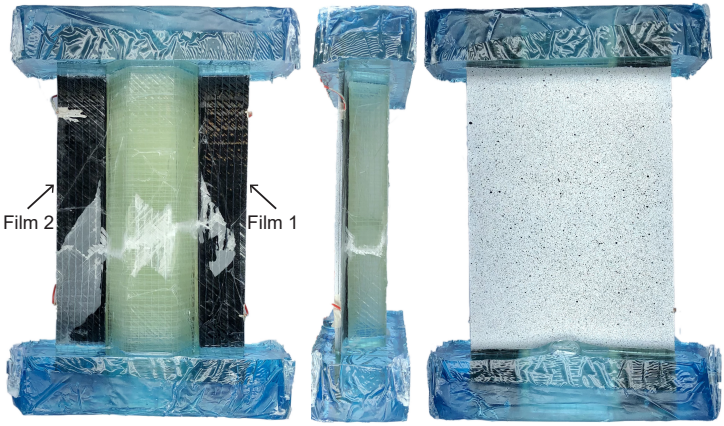

Figure 4.30: Photographs of stringer with integrated film sensors after failure

Figure 4.31 shows force and resistance change measured on the two integrated film sensors during the crippling test, including DIC images for certain interesting times. In general, changes in the force curve are visible in the resistance curves. The resistance change measured on film 2 is decreasing linearly up to approx. 400 seconds with a slight slope change after 100 seconds, where the force curve also shows a slope change. After 400 seconds, the resistance of film 2 starts increasing. This behaviour is similar to the observations on the compression specimens described in Section 4.2.4. The quasi-static compression specimens showed a resistance increase when buckling occurred. The third DIC image, depicting the z-displacement of the backplate at the transition point between resistance decrease and increase, reveals a z-displacement in the area of film 2 visible as a yellow area. From that point onwards, the film experiences no pure compressive load due to the buckling and the resistance increases. The z-displacement grows stronger until the end of the test resulting in a further resistance increase. Film 1 measures almost no resistance change in the beginning of the test, and the further course of the curve is time-shifted with regard to the resistance change of film 2. This behaviour can be attributed to an inhomogeneous, not perfectly symmetrical load transfer, that is also apparent in the DIC images. A z-displacement in the area of film 1 is not measurable in the first three DIC images. In the fourth DIC image, the z-displacement of film 1 is similar to the z-displacement of film 2 in the third DIC image resulting in a similar effect

on the resistance change - the resistance increase in film 1 is measurable as a result of the buckling.

Consequently, the film sensors are suitable for the observation of strains in larger components and can precisely detect the material behaviour. Reliable detection of undesirable buckling and effects of inhomogeneous load introduction is possible.

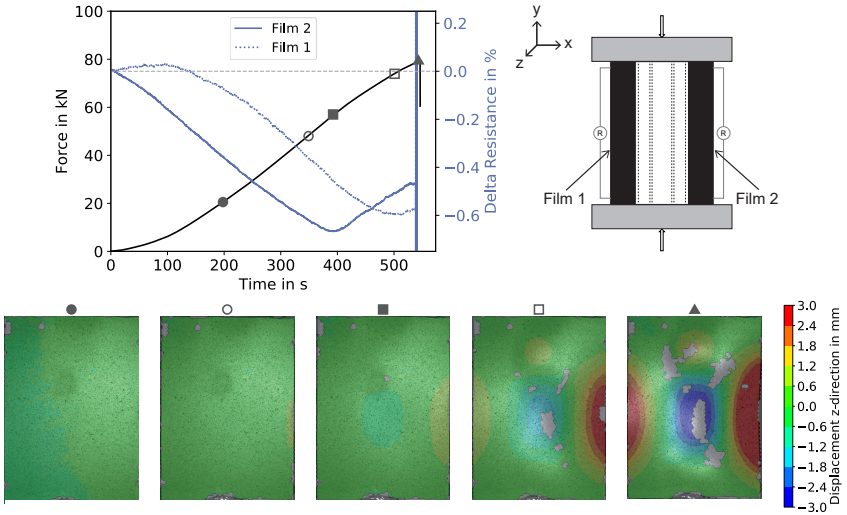

Figure 4.31: Results of a crippling test on a stringer with two integrated films including resistance change and corresponding DIC images showing displacement in z-direction

4.3 Conclusion

The presented results prove that the integrated SWCNT/epoxy films can monitor strains inside GFRPs for different load cases and lay-ups over large material sections or selectively in highly loaded areas, mainly with no significant or even positive effects on the mechanical properties and therefore confirm the working hypothesis:

The local matrix modification with fully-integrated sensor films allows strain and damage monitoring in GFRPs by electrical measurements.

Since the same epoxy system is used during film manufacturing and vacuum infusion process of the laminates and no additional membranes are needed, a chemical crosslinking between the films and the surrounding epoxy resin is achieved. ILSS tests prove a sufficient bonding of the sensors with the surrounding matrix for pre-integration times of up to two days.
The CNT-films' piezoresistive effect enables the correlation of measured resistance change and stress or strain. Local compressive stresses lead to a resistance decrease which is anti-proportional to the applied stress. In contrast, tensile strains induce a strain-proportional increase in resistance. During unloading, damages like matrix cracks, that result in remaining local strains, result in irreversible resistance changes. Drastic resistance increases after crack saturation in CP tensile specimens can be attributed to high local strains due to crack opening, as DIC images reveal.
OHT tests illustrate the ability to monitor local strains in highly loaded areas and at different material depths, gaining valuable insights into the failure process, including local delaminations. Higher strains around the hole can reliably be monitored. The sensitivity can significantly be increased by adapting the film geometry to the expected stress concentration area. The correlation between resistance change and strain as well as the knowledge of the effects of certain damages on the resistance change offers the possibility of detecting critical loads and defining a resistance threshold shortly before final failure.
Fatigue tests proved the durability of the film sensors and showed no premature sensor failure before material failure. Further long-term studies are necessary to fully understand the effects and the influence of combined cyclic and quasi-static loading on the resistance change.
The films can also be used in larger structures as sensors for monitoring strain,

material condition and component deformation as the crippling tests on stringers showed. Critical component buckling can be reliably detected by an increase in resistance, which represents an apparent deviation from pure compressive stress in the film.

In general, the film sensors allow for a highly tailored SHM in GFRPs with low manufacturing and installation effort, as the method of embedding pre-cured CNT/epoxy films offers an easy and automatable way of manufacturing that can be performed on an industrial scale. The flexible thin-film sensors provide easy handling during placement on dry glass fibre fabrics, even on complicated or curved shapes. After placing the sensors, a standard infusion process can be performed. Integrating the films in specific layers or locations offers high design flexibility and provides the means for localised strain and damage monitoring. Therefore, the strain measurements on integrated CNT films offer significant advantages compared to classic surface-mounted strain gauges. Overall, the chosen filler content of 0.5 wt.% results in clearly detectable piezoresistive behaviour and allows for local strain sensing with sufficient sensitivity. Nevertheless, higher sensitivities might be achieved with a filler content closer to the percolation threshold, as applied strain would result in bigger changes in the CNT network. Furthermore, localised monitoring of CFRP structures with this method may be conceivable when embedding the CNT films between isolating epoxy layers.

5 Integrated Carbon Fibre Bundles

Instead of local matrix-modification using CNT/epoxy films, this chapter demonstrates a local modification of glass fibre fabrics with conductive materials. The following research hypothesis is derived for this chapter:

The local integration of electrically conductive fibres enables in-situ damage detection in GFRPs.

To verify this hypothesis, a novel, in-situ SHM technique for damage detection and state estimation in GFRPs using integrated conductive fibres for measuring the capacitance changes due to dielectric material changes introduced by evolving matrix damage is established. The suitability and sensitivity of the method will be evaluated considering different lay-ups, load cases, and damage modes.

5.1 Materials and Experimental Methods

5.1.1 Specimen Preparation

Individual rovings of dry, non-crimp UD UT-E250 glass fibre fabric were replaced with conductors at regular intervals to form walls of integrated capacitors. To analyse various effects, the conductor's type, distance, thickness, and the laminate lay-up were changed. Three conductor types were used to gain insights into the influences of conductor material and the effects of fibrous conductor composition on mechanical and electrical properties. The conductors consisted of CF rovings FT300B 6000-50B, copper wires with an approximate diameter of 1.5 mm and copper strands. The choice of conductors was made according to the geometric specifications of the glass fibre roving, the fabric, and the laminate thickness. Figure 5.1 shows the steps performed during roving replacement with CF roving exemplary for all roving types. First, the stitching yarns were detached from the glass fibre roving, and the roving was removed. Afterwards,

the CF roving was threaded into the fabric in the same manner as the glass fibre rovings. For the copper strands, the replacement process was similar. In the case of the solid copper wire, the wire was inserted in the middle 90°-fabric, and in all other 90°-fabrics, only the glass fibre rovings were removed.

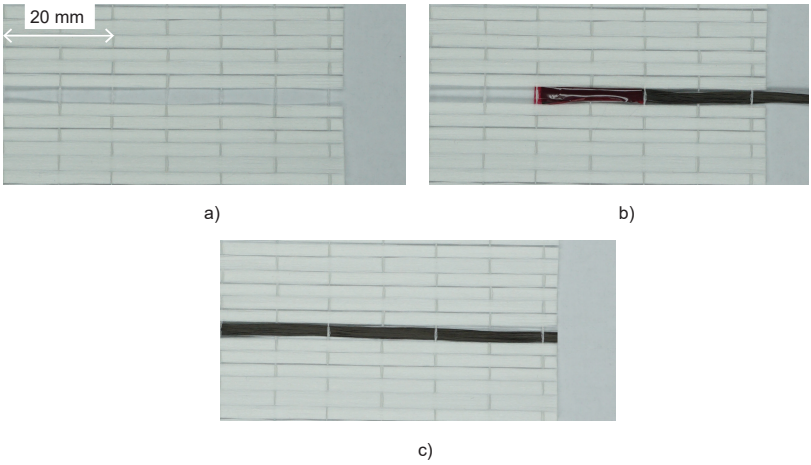

Figure 5.1: Integration process of CF bundles - a) glass fibre fabric with removed glass fibre roving, b) exemplary replacement of glass fibre roving with CF roving, c) glass fibre fabric with replaced CF roving

When stacking the plies, special care was taken to ensure a consistent alignment of the conductive rovings. All plies (modified and unmodified) consisted of the same fabrics. After preparation and stacking of the plies, the standard infusion process described in Section 3.2.1 was applied. Table 5.1 shows the tested tensile specimen configurations, including different conductor materials, conductor distances, conductor thicknesses and two laminate lay-ups. The subscript C denotes a modification of the respective layers with conductors, including material and distance in the remaining columns. Specimens with conductor spacings of 13 mm, 18 mm, 39 mm, and 46 mm were manufactured to understand the influence of the conductor spacing. The CF conductors thickness was changed by integration in four or eight modified 90°-plies. Two configurations of $[90_2/0/45_2]_s$ specimens with conductors either in the 90°-plies or in the 45°-plies were manufactured to investigate the influence of conductor orientation.

Table 5.1: Lay-ups of the tested tensile specimens, including layers modified with conductors denoted by a subscript C, conductor materials and conductor distances

Lay-up	Conductor Material	Distance in mm
$[0/90_{C_4}]_s$	Carbon fibre	13, 18, 39, 46
	Stranded copper	13, 18
	Solid copper	13, 18
$[0/90_2/90_{C_2}]_s$	Carbon fibre	39, 46
$[90_2/0/45_{C_2}]_s$	Carbon fibre	18
$[90_{C_2}/0/45_2]_s$	Carbon fibre	18

After manufacturing of the laminates and cutting of the specimens (see Section 3.2.1), the conductors inside the tensile specimens were contacted to form interleaved capacitors, as shown in Figure 5.2. Electrical contacting was realised at the samples' edges using Acheson 1415 conductive silver paint and LiFy cables with a cross-section of 0.25 mm^2. Few CF roving conductors were short-circuited due to single fibres touching the adjacent roving after the infusion process. These parts of the specimen were not included when contacting the interleaved capacitor leading to different amounts of capacitor walls.

Furthermore, impact tests were conducted on specimens with a $[0/90_{C_4}]_s$ lay-up and a conductor distance of 39 mm following the same manufacturing process. The samples had a size of 75x100 mm^2 and included two conductors each, which were contacted to form a capacitor. Figure 5.3 shows the specimen setup, including the contacting. In order to minimise the influences of the cables and cable movement on the measurements, short wires were used and taped to the sample.

Additionally, neat GFRP specimens of different lengths were cut for relative permittivity measurements. The specimens for the relative permittivity determination were fully contacted at the face sides using Acheson 1415 conductive silver paint. All three contacting directions (in thickness direction, transverse to the fibre direction, and in fibre direction) were tested.

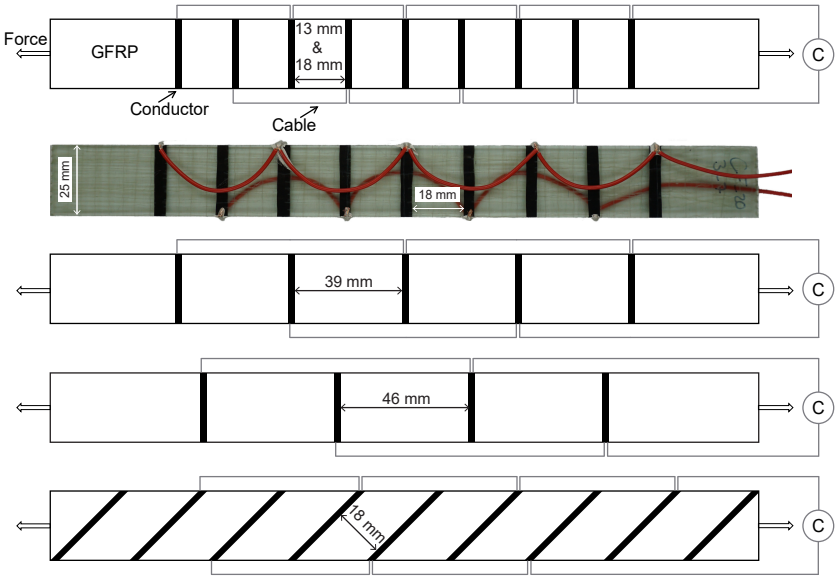

Figure 5.2: Specimen setup and contacting for tensile specimens with different conductor distances and orientations

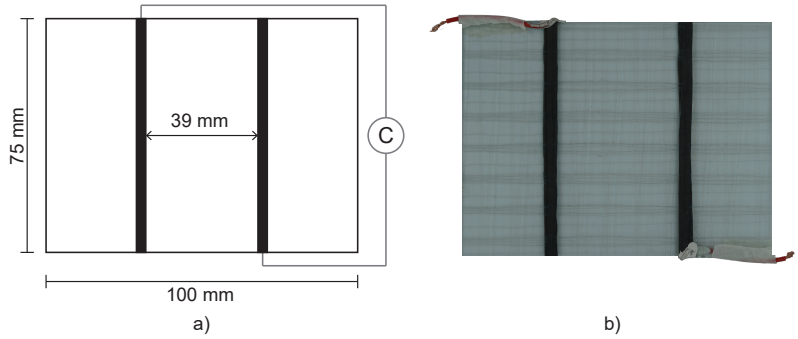

Figure 5.3: Specimen setup and contacting of impact specimens - a) Schematic representation and b) Photograph of representative specimen

5.1.2 Test Setup

Tensile Tests

Tensile tests were performed according to the procedure described in Section 3.3.1. The strain was measured using a multiXtens contact extensometer. The free gauge length and distance between the extensometers were modified from the norm values as shown in Table 5.2 so that all conductors of the interleaved capacitor were located within the free gauge length.

Table 5.2: Free gauge lengths and extensometer distances

Lay-up	Configuration	Gauge length in mm	Extensometer distance in mm
$[0/90_4]_s$	13 mm spacing	155 mm	120 mm
	18 mm spacing	195 mm	150 mm
	39 mm spacing	195 mm	150 mm
	46 mm spacing	185 mm	130 mm
$[90_2/0/45_2]_s$	18 mm spacing	195 mm	150 mm

Quasi-static tensile tests up to failure were performed on all configurations. Additionally, force-controlled step-wise tensile tests were performed on all CP specimens. The five force levels shown in Table 5.3 were applied during the step-wise tests, approximately corresponding to strains of 0.3%, 0.4%, 0.5%, 0.7%, and 1.5%. Between three and ten specimens were tested for all setups and tests. During all tensile tests, the capacitance was measured in-situ with a four-wire sensing setup using a Peaktech® P 2170 LCR meter as described in Section 3.3.2. The tensile machine was grounded electrically to minimise the influence of external factors on the capacitance measurements. Additionally, a video of each specimen was taken for crack evolution monitoring using one camera of the DIC system. The force was synchronised between DIC and the test machine via an analogue output. An LED providing backlight was used to make the cracks more visible in the video. The cracks were counted manually.

Table 5.3: Force levels during force-controlled step-wise tensile tests on $[0/90_4]_s$ specimens

Step	Force in N	Strain in %
1	2600	0.3
2	3000	0.4
3	3400	0.5
4	4000	0.7
5	6800	1.5

Impacts

Impacts with 7 J, 11 J, and 16 J were introduced using a drop tower and an impactor weight of 1.96 kg. Four to eight specimens were impacted for each impact energy. In-situ measurements of the capacitance during impacting were not possible due to safety regulations, as the cables could not be routed out of the drop tower. Therefore, capacitance measurements were performed before and after impacting using a Peaktech® P 2170 LCR meter with similar settings as during the tensile tests (see Section 3.3.2). Five measurements were performed on each sample before and after the impact. To reduce influences from connecting and disconnecting the LCR meter, the clamps were disconnected and reconnected between each measurement. A customised Matlab program was used to determine the delamination size within each sample. The program distinguished impacted and non-impacted areas in each specimen via fixed thresholds in the HSV (hue, saturation, value) colour space.

5.2 Results and Discussion

5.2.1 Permittivity Determination

To determine the relative permittivity of the CP material ϵ_r in thickness direction, transverse to the 0°-fibre direction and in 0°-fibre direction (longitudinal), capacitance measurements were carried out. For longitudinal relative permittivity, samples of different lengths were measured, and the inverted values of the measured capacitance C_m were plotted over the respective sample lengths, as shown in Figure 5.4.

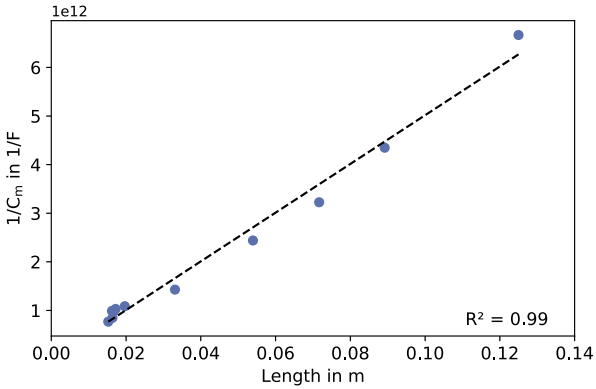

Figure 5.4: Plot for the determination of relative permittivity in 0°-fibre direction of $[0/90_4]_s$ GFRP

The relative permittivity is calculated following Equation (5.1) [92] from the slope of the linear regression fit, which depicts the measured values well.

$$\text{slope} = \frac{1}{\epsilon_0 \epsilon_r A} \tag{5.1}$$

The calculated longitudinal relative permittivity of the material $\epsilon_{\text{r,GFRP}}$ is 46. This value is relatively high compared to different values of GFRPs in the literature [184, 185]. Various reasons might be the cause. Thinking of the specimen as an ideal plate capacitor, the plate area formed by conductive silver paint on two edges of the sample is small compared to the distance of the capacitor plates given by the length of the specimen. Therefore, a strongly curved and reoriented electric field is present in the air around the edges of the specimen. This fringing

electric field leads to a higher apparent capacitance, which results in a higher apparent permittivity. This effect was also found in concrete by Wang et al. [186]. The effect of fringing electric fields on the permittivity becomes higher, the bigger the capacitor plates' distance (see schematic in Figure 5.5).

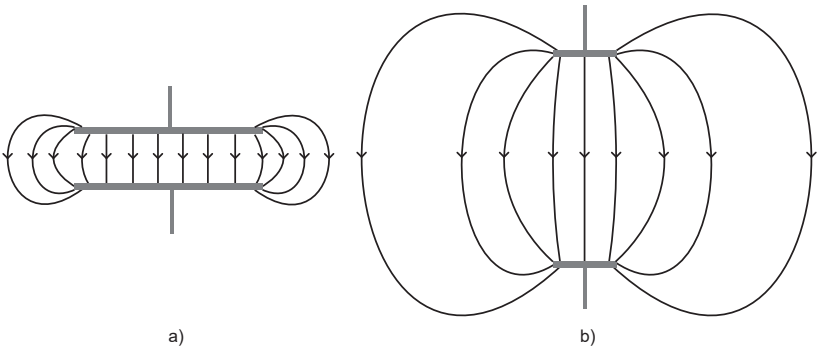

Figure 5.5: 2D schematic visualisation of the electric field of a plate capacitor for a) small plate distance and b) high plate distance

To support this theory, the relative permittivity of the material was also determined in the thickness direction of the material on specimens with 400 mm^2 area providing a significantly larger area and smaller distance. In this case, the relative permittivity calculated from capacitance measurements was approx. 6, as shown in Figure 5.6, and therefore in the range of other values found in the literature [184, 185].

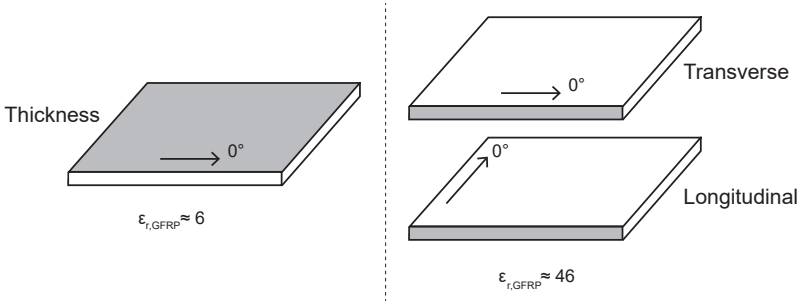

Figure 5.6: Schematic representation of contacting for relative permittivity determination in different directions

Additionally, the permittivity shows frequency-dependent behaviour increasing with lower frequency. Within this study, a low frequency of 10 kHz is used compared with the MHz or GHz used in the literature [184, 185]. However, the absolute relative permittivity value is not essential for further experiments since only the relative capacitance change is considered during tensile tests.

5.2.2 Detection of Matrix Cracks in Tensile Tests

Influence of Conductor Material

CF bundles, stranded copper wires and solid copper were used as conductors for capacitance measurements in GFRPs to gain insights into the effects of different materials and conductor compositions on the capacitance measurements and sensing abilities. Two different conductor distances were investigated for all three conductor types in order to ensure the qualitative results against a distance influence. The distances were changed only slightly between 13 mm for the narrower and 18 mm for the wider spacing. Within this subsection, the results are shown for all three materials, but the distance influence will be analysed in more detail in the following subsection, using CF bundle conductors as an example. This subsection focuses on the influence of the conductor material.
In an idealised, theoretical view, the conductors (CF, solid copper and copper strands) inside the tensile specimens can be regarded as plates of a plate capacitor. Equation (5.2) describes the capacitance of an ideal plate capacitor using the permittivity of vacuum ϵ_0, the relative permittivity of the dielectric medium ϵ_r, and the area A and distance d of the plates.

$$C = \epsilon_0 \epsilon_r \frac{A}{d} \tag{5.2}$$

The distance d is the conductor spacing. The area A is calculated as the thickness of the modified layer t_{mod} times the specimen width w. For the configurations analysing the conductor materials' influence, the modified layer thickness t_{mod} equals the 90°-layer thickness t_{90}. Using the previously determined, longitudinal relative permittivity value $\epsilon_{\mathrm{r,GFRP}}$=46 of the material, the capacitance of a single plate capacitor is calculated to 1.17 pF for a conductor distance of 13 mm. This theoretical value is in good agreement with the measurement values 1.21 ± 0.33 pF of the specimens with CF conductors. Deviations of calculation

and measurement result from divergence from the assumptions of an ideal plate capacitor.

Micro-sections of the conductors shown in Figure 5.7 reveal the limitations of the assumption of ideal plates with uniform distance and rectangular area calculated from the 90°-layer thickness and specimen width. Due to imperfect alignment of the conductive rovings in the single plies and ply movement during infusion, the distance between the conductors is non-uniform over the thickness of the 90°-layer in the case of CF and stranded copper conductors. This effect results in a significantly larger area of the conductors since the thickness of the 90°-layer is smaller than the actual length of the conductor surface in the thickness direction. On micro-scale, as shown in the schematic enlargement, the surface area of the fibrous conductors is not flat due to the geometry of the fibres resulting in a bigger conductor surface. In the case of solid copper conductors, the effects are qualitatively similar due to the circular cross-section of the conductor.

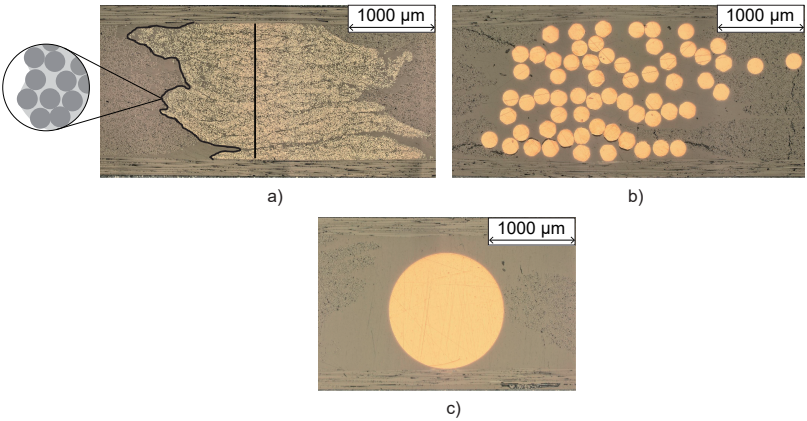

Figure 5.7: Side-view on conductors a) CF, b) stranded copper wire, c) solid copper wire

Within the tensile specimens the CF bundles are contacted to form interleaved capacitors (see Figure 5.2). Figure 5.8 shows a schematic representation of a plate capacitor and an interleaved capacitor.

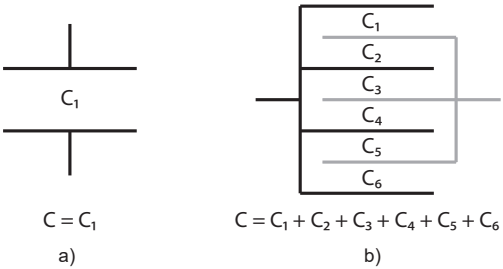

Figure 5.8: Schematic representation of a) plate capacitor and b) interleaved capacitor

The total capacitance C of an interleaved capacitor is calculated as a sum of the individual capacitances C_n according to Equation (5.3).

$$C = \sum_{n=1}^{N} C_n \tag{5.3}$$

Therefore, the interleaved capacitor has a higher total capacitance than the measurement on single, individual capacitors. As measuring small capacitances usually requires expensive measuring equipment and is prone to measurement deviations due to small external influences, connection as interleaved capacitors allows for more stable measurements. Furthermore, the contacting as interleaved capacitor offers the possibility of monitoring a larger area with a single measurement.

Before the analysis of the capacitance measurements, the influence of the three conductor types on the mechanical properties of the tensile specimens is analysed. Comparing the mean tensile strength values of the specimens with the three conductor configurations and both spacings with non-modified reference specimens, a slight decrease of maximum 6% in the case of the stranded copper conductors is visible (see Figure 5.9). However, the decrease is not pronounced as all standard deviations overlap. The outer 0°-layers mainly determine the tensile strength. Hence, the replacement of single CF rovings in the 90°-layer of the CP specimens does not significantly change the material's tensile strength.

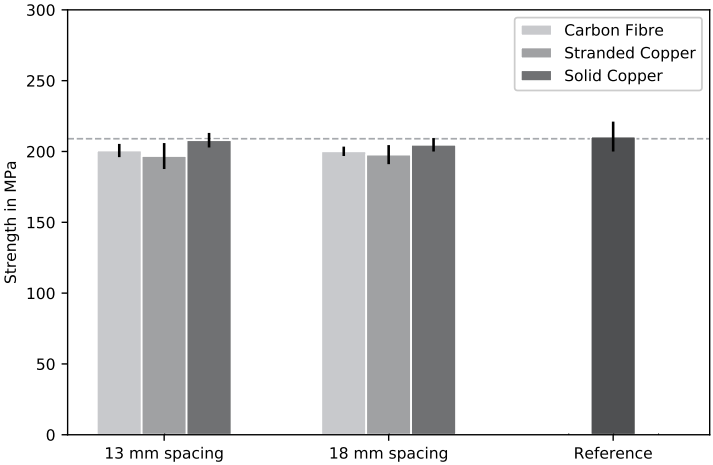

Figure 5.9: Strength of the $[0/90_4]_s$ GFRP specimens in MPa for different conductor configurations (CF, stranded copper, solid copper) and distances (13 mm and 18 mm) compared with reference specimens without conductors

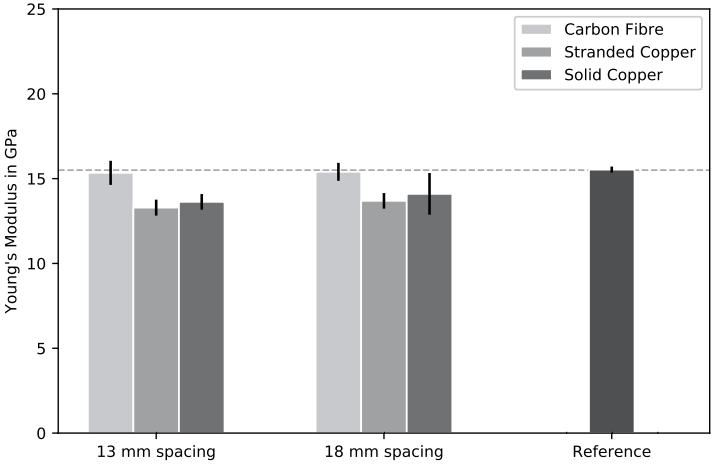

Figure 5.10: Young's modulus of the $[0/90_4]_s$ GFRP specimens in MPa for different conductor configurations (CF, stranded copper, solid copper) and distances (13 mm and 18 mm) compared with reference specimens without conductors

The Young's modulus of the specimens is shown in Figure 5.10. The integration of the CF conductors does not significantly impact Young's modulus. There is a slight decrease of 1.21% for 13 mm spacing and 0.79% for 18 mm spacing. In the case of the stranded and solid copper conductors, Young's modulus is lowered between 9.21% and 14.44%. The micro-sections of the conductors in Figure 5.7 show that resin-rich regions are present around the copper conductors. These resin-rich regions result in a lower fibre volume fraction and hence a lower Young's modulus.

Figure 5.11 shows representative results of quasi-static tensile tests on specimens with all conductor types. Mechanically, all configurations have similar stress-strain curves and exhibit a clear stiffness decrease between 0.3% and 0.4% strain - visible as knee point. The knee point clearly correlates with crack initiation and the rapid development of matrix cracks. With increasing strain, fewer cracks develop.

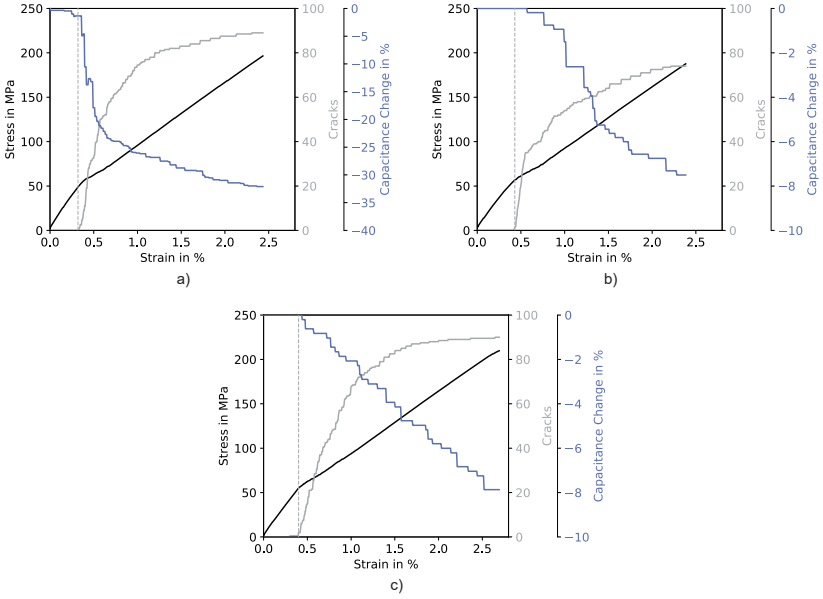

Figure 5.11: Plots showing stress in MPa, capacitance change in % and counted cracks over strain for tensile tests on specimens with a) CF conductors, b) stranded copper conductors, c) solid copper conductors

The crack development in two segments of a CF conductor specimen with 18 mm conductor spacing for 0.5% strain, 0.7% strain, and 1.5% strain is depicted in Figure 5.12. In the pictures with 0.5% and 0.7% strain, individual cracks are easily recognisable as solid black lines and mostly span the whole specimen width. For higher strains, the crack pattern is more diffuse. Cracks are no longer visible as clear black lines but as grey shadows, which are sometimes difficult to distinguish from the yarn. It is also noticeable that many cracks no longer span the entire specimen width. These effects lead to a possible underestimation of counted cracks.

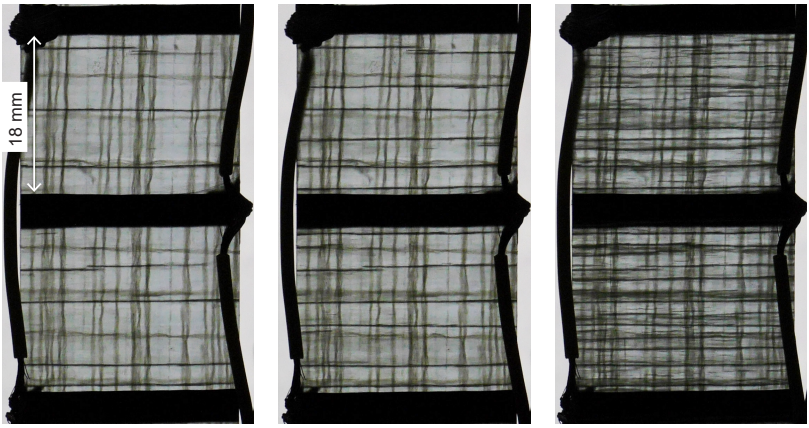

Figure 5.12: Crack evolution in specimen with CF conductors at a) 0.5% strain, b) 0.7% strain, c) 1.5% strain

The in-situ capacitance measurements show different behaviour for the three conductor types (see Figure 5.11). Therefore, the y-axes' scales of the capacitance change vary for the single subplots. The capacitance change ΔC in percent is calculated according to formula (5.4) using the current capacitance C and the initial capacitance C_0. The percentage-wise capacitance change is independent of the number of contacted rovings forming the capacitor walls of the interleaved capacitor.

$$\Delta C = \frac{C - C_0}{C_0} 100 \tag{5.4}$$

In the specimens with CF conductors, the measured capacitance starts to decrease strongly during rapid crack growth. The decrease slows down with the

formation of fewer new cracks reaching a maximum value of 32%. There is a strong correlation between the counted transverse cracks and the capacitance change. Therefore, the development of cracks is assumed to be the major effect influencing the capacitance change. Furthermore, no debonding of CFs and the surrounding resin is visible in the micro-sections of tested specimens (see Figure 5.7).

The capacitance decrease in tensile tests with specimens with stranded copper conductors is overall a little delayed compared to the crack evolution (see Figure 5.11). The capacitance does not decrease directly after crack initiation but stays constant for some additional strain. The gradient of the capacitance decrease continues to decrease as the tensile test progresses. However, the capacitance does not decrease as much with crack formation as visible for the CF conductors. The maximum capacitance decrease is around 8% and thus approximately four times smaller than in specimens with CF conductors. In the micro-sections in Figure 5.7, a debonding of some copper strands from the surrounding matrix is visible.

For solid copper conductors, the point of capacitance change crack initiation can precisely be detected as a slope change in the capacitance decrease. Before crack initiation, no capacitance change is visible. After crack initiation, a linear decrease of the capacitance change is visible. However, the slope of the capacitance change is not changing until the end of the test. Faster or slower crack evolution has no measurable effect on the capacitance decrease. The maximum capacitance change is around 7.5%, similar to the stranded copper conductors. No debonding of the solid copper conductors and the surrounding matrix is visible in the micro-sections (see Figure 5.7).

The CF conductors show the highest sensitivity to capacitance changes due to cracks comparing the quantitative amount and qualitative shape of the measured capacitance change. Micro-sections of the conductors (see Figure 5.7) show that in the case of CF conductors, no resin-rich area is present between the conductor and the surrounding GFRP. For stranded copper conductors, a resin-rich area between the single strands and around the conductors is observable. An even bigger resin-rich area is visible around the solid copper conductors. The CF conductors are formed of eight integrated 6K rovings consisting of CFs with a nominal diameter of 7 µm. Stranded copper conductors consist of 64 copper strands with a diameter of 186 µm. The single solid copper wire has a diameter of 1319 µm. The total surface area of the CFs in contact with the

matrix is factor 28.2 higher than for the stranded copper wires and factor 255 higher than for the solid copper. The fibrous nature of the conductors leads to a higher sensitivity of capacitance change to crack formation. The CF and stranded copper conductors both show a regressive drop in capacitance with a progressive increase in cracks, whereas only a linear drop can be measured for the solid copper wires. Another reason for the sensitivity difference could be the material difference between carbon and copper. CF conductors show a four times larger total capacitance change than both copper conductor configurations.

Force-controlled step-wise tensile tests on CF and solid copper conductor specimens have been performed to understand the reversibility of the capacitance decrease and other influences as time-dependency and closing of cracks during unloading.

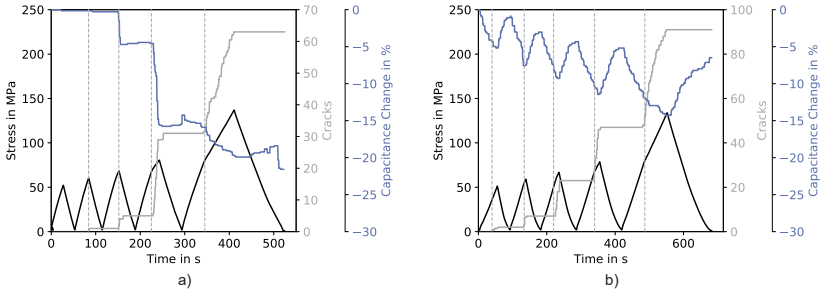

Figure 5.13: Stress in MPa, capacitance change in % and counted cracks over time for step-wise tensile tests on specimens with a) CF conductors b) solid copper conductors

Figure 5.13 includes representative results for CF and solid copper conductors. Since the stranded copper conductors have shown a qualitatively similar but delayed and less sensitive capacitance decrease than the CF conductors in quasi-static tests up to failure, the results of step-wise tests on stranded copper conductors are not further analysed. The step-wise tests on specimens with CF conductors allow for similar conclusions as the quasi-static tensile tests up to failure. The capacitance decrease is mainly crack-driven and corresponds well to the counted cracks (compare vertical dashed lines), and stiffness decrease visible as knee point. A smaller increase in crack count results in a smaller capaci-

tance decrease. More sudden development of cracks leads to a faster capacitance decrease. Furthermore, the capacitance decrease due to cracks appears to be mostly irreversible. For higher strain, the capacitance increases slightly during unloading, followed by a decrease with a similar slope during re-loading until new cracks develop. This effect results from a distance change of the CF bundles due to strain as well as opening and closing of existing cracks and hence gets stronger with higher strain and crack number. The influence of the distance change resulting from strain on the capacitance decrease is small, as the highest applied strains are approximately 1.5% in the last loading step. In general, step-wise tensile tests on CF conductor specimens show that the mostly irreversible capacitance change due to cracks enables a crack state evaluation with initial and current capacitance value without knowing the complete capacitance curve. For solid copper conductors, the capacitance change shows a step-wise behaviour with maxima and minima opposing the force curve. The capacitance change during the single load steps seems to be mostly distance-driven. However, the percentage change in capacitance is larger than expected from a pure distance change of the conductors resulting from the applied strain. The crack evolution is not visible in the capacitance change with equal sensitivity as for the CF conductors. Nevertheless, the influence of cracks on the capacitance is also evident with solid copper conductors. The non-reversible global reduction of the individual maximum capacitance values in the unloaded state between the individual force steps is crack-driven. This effect was verified using a step-wise test with four 3400 N force steps followed by one 6800 N force step. Some cracks developed during the first load step, and the maximum capacitance after the first load step was smaller than the initial capacitance. Almost no new cracks formed in the remaining three load steps with equal force than the first step. Therefore, the individual maxima of the capacitance remained almost constant after the force steps. The higher force in the last step led to additional crack formation, and the maximum capacitance value after this load step was smaller than after the previous load steps. Capacitance measurements on integrated solid copper conductors enable a conclusion about the damage state of the GFRP. But in order to make a statement about the current state of damage without knowing the full capacitance curve, the specimen must be measured in the same load condition as during the initial capacitance measurement due to the strong influence of the strain. CF conductors beyond the higher sensitivity have the advantage that a correlation of the capacitance measurements and the state of damage is

possible even without knowledge about the loading history. The origin of the different behaviour of the capacitance decrease for the conductor types remains an open point for further investigations. Due to the beneficial sensing abilities and the neglectable influence of the CF bundles on Young's modulus, only CF conductors will be analysed from this point onwards.

Analytical Modelling

In order to further evaluate the correlation of the cracks and the capacitance change, an analytical model of the capacitance decrease using the number of cracks inside the specimen is developed, considering the conductors as plates of an ideal plate capacitor with a uniform electric field. As described for the relative permittivity determination, the distance between the conductors is assumed to be uniform over the thickness of the 90°-layer and the area of the conductors is calculated as rectangular area A determined from the thickness of the modified layer t_{mod} and the specimen width w. Initially, there is only GFRP as a dielectric medium between the plates. The elongation of the specimen results in a distance change of the conductors. The pure distance change leads to a linear capacitance decrease proportional to the introduced strain. However, the appearance of cracks introduces air as a second dielectric medium between the conductors. Figure 5.14 shows a schematic of the idealised capacitor in the specimen with the assumption of uniform rectangular cracks and a plate capacitor with two dielectrics.

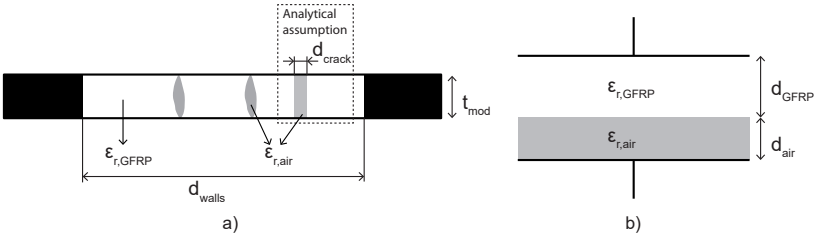

Figure 5.14: Schematic of idealised plate capacitor formed between CF conductors in 90°-layer of the specimen including cracks and theoretic view as parallel plate capacitor for analytical modelling

Thus, after crack initiation, Equation (5.2) changes to Equation (5.5), which considers the different permittivities of GFRP $\epsilon_{\mathrm{r,GFRP}}$ and air $\epsilon_{\mathrm{r,air}}$.

$$C = \epsilon_0 A \frac{\epsilon_{\mathrm{r,GFRP}} \epsilon_{\mathrm{r,air}}}{d_{\mathrm{GFRP}} \epsilon_{\mathrm{r,air}} + d_{\mathrm{air}} \epsilon_{\mathrm{r,GFRP}}} \tag{5.5}$$

The distance of the GFRP d_{GFRP} is defined as the unstrained distance of the walls d_{walls}, and the thickness of the dielectric air d_{air} is calculated from the counted number of cracks n_{cracks} and the crack opening d_{crack}. Furthermore, the previously in Section 5.2.1 determined, apparent, longitudinal relative permittivity $\epsilon_{\mathrm{r,GFRP}}$ of 46 and the relative permittivity of air $\epsilon_{\mathrm{r,air}}$ 1.0006 are used for calculation. In enclosed damages that do not extend to the specimens' edges, the medium could also be vacuum. However, as the relative permittivities of air and vacuum are very similar, the dielectric medium inside the damage will be referred to as air in the further course of this thesis. Including the assumptions, Equation (5.5) is modified to Equation (5.6). Capacitance change in percent is calculated similarly to the experimental capacitance change according to Equation (5.4).

$$C = \epsilon_0 w t_{90} \frac{\epsilon_{\mathrm{r,GFRP}} \epsilon_{\mathrm{r,air}}}{d_{\mathrm{walls}} \epsilon_{\mathrm{r,air}} + n_{\mathrm{cracks}} d_{\mathrm{crack}} \epsilon_{\mathrm{r,GFRP}}} \tag{5.6}$$

Equation (5.6) does not include a straining of the material before crack onset. However, the straining of the material prior to cracking results in a distance change of the bundles that influences the capacitance. Therefore, the distance of the walls d_{walls} in Equation (5.6) is substituted by the strained distance of the walls before crack onset $d_{\mathrm{walls,\ strain}}$ that is defined according to Equation (5.7), using the strain at crack onset s_{crack1} in %,

$$d_{\mathrm{walls,strain}} = d_{\mathrm{walls}} \left(1 + \frac{s_{\mathrm{crack1}}}{100}\right) - n_{\mathrm{cracks}} d_{\mathrm{crack}} \tag{5.7}$$

For ease of calculation, only one plate capacitor is used for modelling. Therefore, the total counted cracks are divided by the total number of counted segments of the interleaved capacitor resulting in decimal numbers of counted cracks. Microsections of the cracked specimens showed crack openings between 5 µm and 15 µm in the unloaded specimens. The crack opening varies from crack to crack and within a single crack, depending on surrounding fibre arrangement and resin distribution. Therefore, crack opening is non-uniform over the thickness and width of the specimen. During the load application, the crack opening is bigger than in the unloaded specimens. The crack opening varies in the course of the

tensile test. The first transverse crack develops when the stress in the 90°-layers is higher than its strength. After the first crack's development, the 0°-layers have to withstand additional stress. Load transfer between the longitudinal and transverse plies is governed by the shear stress at the interface. The crack opens further with a higher load until additional transverse cracks develop when the stress transferred into the transverse ply exceeds the strength again. As a result of the crack formation, local stresses are reduced so that the crack opening of the surrounding cracks is decreased. Crack saturation is reached when the transferred stress in the 90°-layer does not exceed its strength anymore. The additional strain applied until fracture of the 0°-layers leads to crack opening of all transverse cracks. Nevertheless, a uniform, load-independent crack opening is assumed for all cracks in the analytical modelling.

Figure 5.15 shows the analytical capacitance decreases for two different crack openings with and without the influence of straining before crack onset compared to the measured capacitance decrease for a representative specimen with 18 mm conductor spacing. The darker blue lines depict the analytical results including the strain before crack onset and the lighter blue lines demonstrate the analytical modelling without considering the strain before crack development. The dashed lines show the analytical results for a crack opening of 10 µm, which resembles the average of the crack openings measured in the micro-sections of the unloaded specimens and therefore a lower estimate of the actual crack opening. Additionally, the dotted lines show the analytical capacitance decrease for 15 µm crack opening. This value is chosen to represent the higher crack opening under load and shows how the crack opening influences the analytical modelling. The actual crack opening varies in the range of these two values.
The modelled and measured capacitance decreases are similar in shape. For lower strains and few cracks, all analytical calculations are in good agreement with the experimental capacitance decrease. In general, taking the strain into account, results in a slightly bigger capacitance change than solely considering the influence of the cracks. The effect has the same size as the applied strain. Thus, the distance between the modellings with and without consideration of the strain increases linearly towards the end of the test. From 0.45% strain onwards, the measurement shows a higher capacitance decrease than the analytical modellings with a 10 µm crack opening. For a crack opening of 15 µm, both modelling approaches - including the influence of cracks and additionally

considering the effect of the strain - qualitatively and quantitatively match the experimental results. The modelling for a crack opening of 15 µm with consideration of the strain fits extremely well at the end of the test. However, in the region between approximately 0.75% and 1.75% strain, the calculations without strain effect show a better fit.

The observations are in good agreement with the results of the step-wise tests (see Figure 5.13) that showed a first small capacitance increase with unloading after the third load step resembling 0.5% strain. For lower strains and a small number of cracks, the static crack opening determined from the micro-sections is suitable to describe the capacitance change since no significant effect of crack opening and closing is observed. Afterwards, the influence of the applied strain and the crack opening on the capacitance decrease increases. The crack opening under load is higher than the static crack opening. Therefore, in particular, for higher strains and when fewer cracks develop, the analytical modelling for the higher crack opening of 15 µm better reflects the experimental results. The part-wise slight overestimation and slight underestimation of the capacitance decrease for the higher crack opening enhance the assumption of a dynamic crack opening during the tensile tests. The influence of the strain is small and mostly neglectable but results in a better fit when cracks reach saturation towards the end of the test.

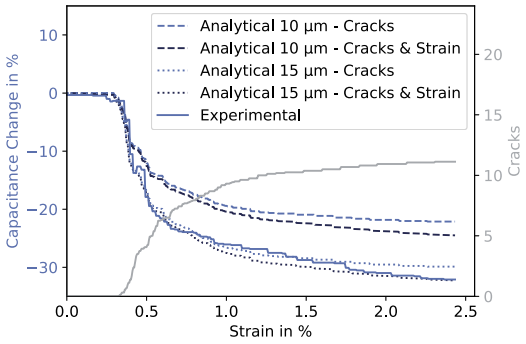

Figure 5.15: Measured capacitance decrease of a CF conductor specimen compared with analytical modelling as ideal plate capacitor with dielectric property change due to air introduced by cracks (lighter blue lines) for crack openings of 10 µm (dashed lines) and 15 µm (dotted lines) and additional distance change due to strain before crack onset (darker blue lines)

With assumptions regarding the crack opening, an analytical determination of the number of cracks and hence the damage state of the material is possible based on the measured capacitance decrease. In the manufactured specimens, some of the assumptions for an ideal plate capacitor made for simplicity of calculation (uniform electric field, uniform conductor distance, rectangular cracks with uniform opening, rectangular conductor area) are not entirely valid. However, the agreement between the theoretical and experimental values justifies the assumptions and the analytical modelling.

Influence of Conductor Thickness and Distance

The distance between the CF bundles was increased, and the number of modified plies was decreased to evaluate the influence on the measurements' sensitivity. The distance and thickness variation has no significant influence on the strength, as Figure 5.16 shows. Comparing modified specimens with different conductor distances and thicknesses, all specimens have a similar strength. All modified configurations exhibit slight strength decreases between 2.15% (46 mm, eight plies) and 6.71% (39 mm, four plies) compared to the neat GFRP specimens, but the decrease is not significant, as the standard deviations overlap, and the outer 0°-layers primarily determine the strength. Young's modulus is even less affected by the modification, as depicted in Figure 5.17. Mostly, the configurations have similar Young's modulus as neat GFRP samples with decreases between 0.23% (46 mm, four plies) and 1.21% (13 mm, eight plies). Only the configurations with 39 mm and 46 mm and eight modified plies show Young's modulus increase of approx. 6%.
Consequently, the influence of the distance and thickness modification on the mechanical properties is not significant, as likewise found for lower conductor distances.

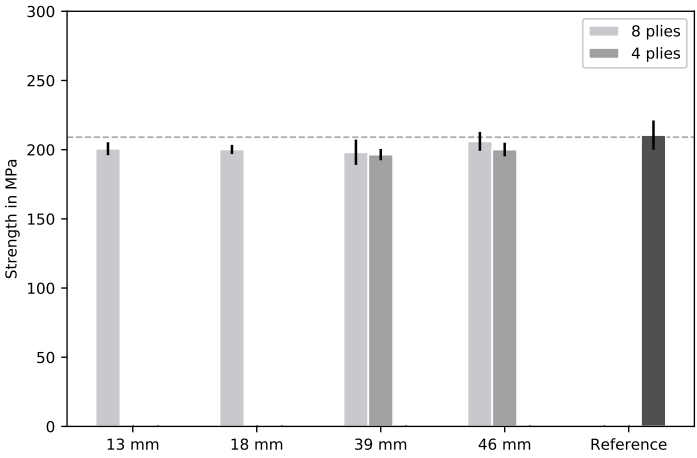

Figure 5.16: Strength of the $[0/90_4]_s$ GFRP specimens in MPa for different CF conductor distances (13 mm, 18 mm, 39 mm, and 46 mm) and conductor thicknesses (4 plies, 8 plies) compared with reference specimens without conductors

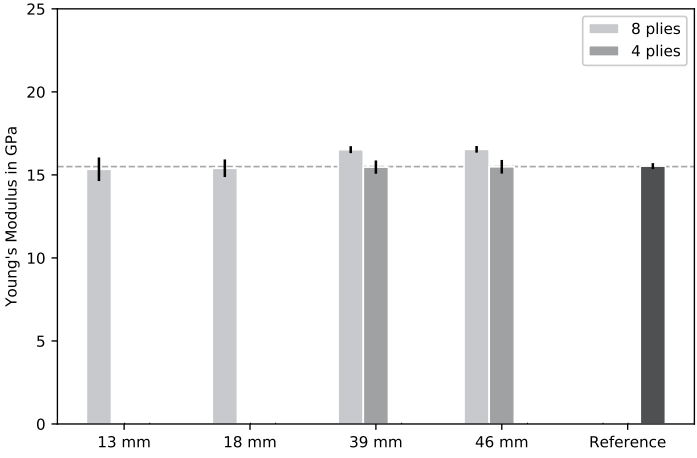

Figure 5.17: Young's modulus of the $[0/90_4]_s$ GFRP specimens in MPa for different CF conductor distances (13 mm, 18 mm, 39 mm, and 46 mm) and conductor thicknesses (4 plies, 8 plies) compared with reference specimens without conductors

Figure 5.18 shows representative results of quasi-static tensile tests on specimens with conductor distances of 39 mm and 46 mm and four and eight modified plies conductor thickness. The general trend found for the samples with 13 mm and 18 mm conductor spacing remains visible for all configurations. The specimens exhibit a clear capacitance decrease between 0.3% and 0.4% strain that correlates with fast crack development and a distinctive knee point in the stress-strain curve. All configurations show a sufficient sensitivity of the capacitance to crack initiation and growth to qualitatively monitor the stages of crack development. Crack initiation and fast crack growth result in a steep capacitance decrease in the area of the knee point, and slower crack development and growth towards the end of the test is resembled by a lower slope of capacitance decrease. Nevertheless, the sensitivity of the capacitance change concerning cracks is lower for higher conductor distances and lower thicknesses. The capacitance decrease for all configurations with 39 mm and 46 mm spacing shows a significantly more rugged course than the capacitance decrease in specimens with 18 mm conductor distance, as representatively shown in Figure 5.11a). In particular, slower crack development and minor crack growth towards the end of the test are not as precisely resembled in the capacitance decrease for specimens with higher distances. As opposed to specimens with lower spacing, no further capacitance decrease is measured above approx. 1.4% strain in specimens with 39 mm spacing and above approx. 1.1% strain in specimens with 46 mm spacing, although the number of cracks still increases slightly. A thickness decrease of conductors with equal distance leads to a further sensitivity decrease.

Depending on the sensitivity requirements, a smaller amount of CF bundle conductors can provide reliable material state evaluation with sufficient sensitivity, resulting in lower costs and manufacturing effort.

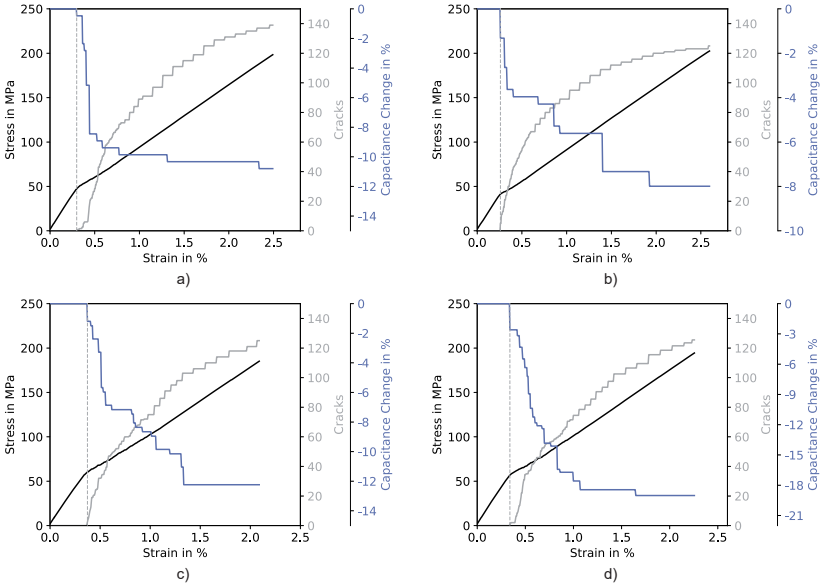

Figure 5.18: Stress in MPa, capacitance change in % and counted cracks over time for quasi-static tensile tests on specimens with a) 39 mm spacing and 4 modified plies, b) 46 mm spacing and 4 modified plies, c) 39 mm spacing and 8 modified plies, and d) 46 mm spacing and 8 modified plies

Step-wise tests show a pronounced sensitivity difference between four and eight modified plies, as displayed in Figure 5.19. In specimens with eight modified plies conductor thickness, a capacitance decrease with crack formation is measured for all tested distances during all load steps. Specimens with a smaller conductor thickness show a less significant correlation between the counted crack increase and the step-wise, irreversible capacitance decrease from the second load step (0.4% strain) onwards. In particular, the specimens with a high conductor distance of 46 mm and a small conductor thickness demonstrate almost no noticeable correlation between cracks and capacitance change from the second load step (0.4% strain) onwards. However, the crack initiation is clearly measurable in the capacitance change. Furthermore, the effect of capacitance increase as a consequence of a distance change of the CF bundles due to strain as well as closing of existing cracks during unloading, as observed for specimens with a smaller CF bundle distance (see Figure 5.13), is not measurable for the higher CF bundle spacings.

Consequently, a maximum distance and minimum thickness have to be found for specific specimen geometries and monitoring cases according to the sensitivity and monitoring requirements. Crack initiation can equally reliably be monitored with a higher conductor distance, while smaller changes towards the end of the test are more precisely monitored with a smaller spacing.

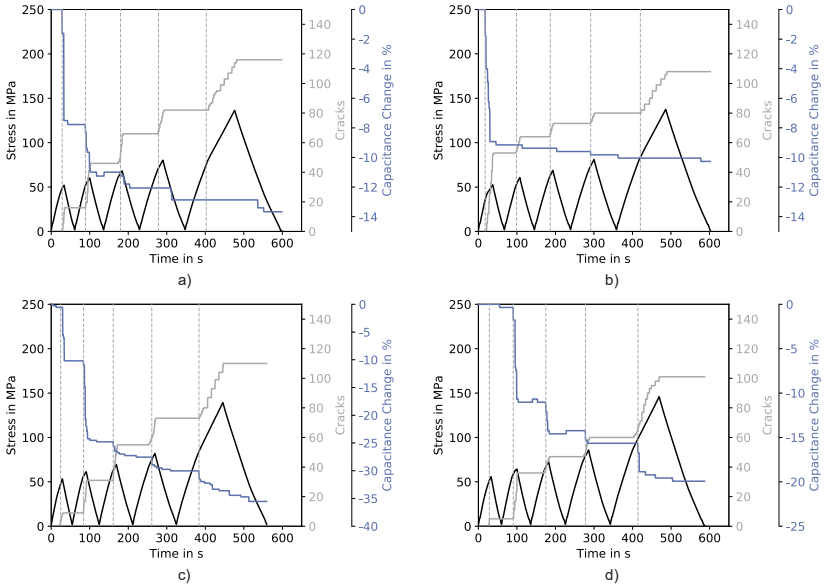

Figure 5.19: Stress in MPa, capacitance change in % and counted cracks over time for step-wise tensile tests on specimens with a) 39 mm spacing and 4 modified plies, b) 46 mm spacing and 4 modified plies, c) 39 mm spacing and 8 modified plies, and d) 46 mm spacing and 8 modified plies

Results of analytical modelling in comparison with the experimental measurements of a 46 mm with eight plies conductor thickness support the observations. Modelling and experimental results show a close agreement for crack openings of 10 µm up to around 1.1% strain or the fourth load step, respectively. For higher strains, the analytical modelling tends to overestimate the capacitance decrease. Further crack development is not detected in the measured capacitance change due to the lower sensitivity. Because of the lower sensitivity, the strain influence on the distance between the conductors is also not detected in the measurements and therefore likewise neglected in the evaluation of the ana-

lytical modelling. The analytical modelling is performed according to Equation (5.6). Specimens with smaller spacing and therefore higher sensitivity showed a good correlation until the end of the test (compare Figure 5.15).

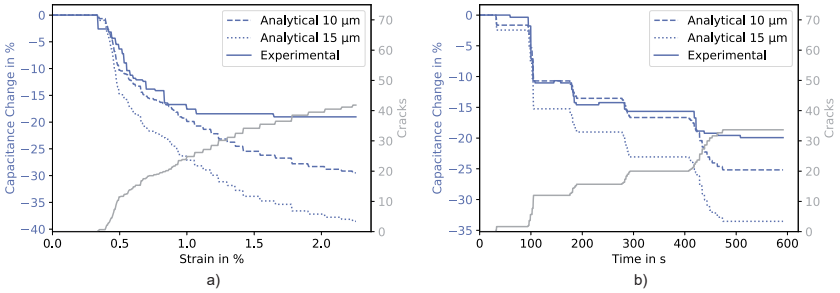

Figure 5.20: Measured capacitance decrease of a CF conductor specimen compared with analytical modelling as ideal plate capacitor with dielectric property change due to air introduced by cracks for crack openings 10 µm (dashed line) and 15 µm (dotted line) and distance change due to strain for tensile tests on specimens with 46 mm conductor spacing and 8 plies conductor thicknesses - a) quasi-static test and b) step-wise test

To improve the cost-efficiency, the required amount of CF rovings can be reduced while maintaining a crack sensing ability for higher conductor distance and lower conductor thickness. However, especially towards the end of the tensile tests, where a more diffuse crack pattern is present, the sensitivity decreases for higher distance and lower thickness. Hence, reasonable limits have to be defined according to the sensing requirements, material setup, specimen geometry, and LCR meter's sensitivity. A higher width of the integrated bundles increases the overall capacitance according to Equation (5.2). Therefore, a higher distance or lower thickness of the bundles might be achievable while retaining the sensing capability of the LCR meter. Most likely, more sensitive measurement equipment allows for larger conductor spacing and lower conductor thickness.

Influence of Layer Orientation

As discussed, matrix cracks in the 90°-layer of a GFRP CP composite are clearly detectable by capacitance measurements between integrated CF bundles. CF bundles are integrated in a $[90_2/0/45_2]_s$ composite to exploit the monitoring potential further. Two specimen configurations, including CF bundles with a

distance of 18 mm, either integrated in the 90°- or 45°-plies are manufactured. Figure 5.21 shows the results of tensile tests on most representative specimens of both configurations within the same diagram. The representative specimens were chosen according to the mechanical behaviour, crack development and capacitance decrease. The difficulty was to find samples that were qualitatively and quantitatively representative for all three criteria at once. The best compromise is depicted in Figure 5.21 - focusing more on qualitative than quantitative representativeness. Greater attention was paid to the crack initiation and initial crack development than to the final failure, as the measuring system is intended to reliably monitor the crack development since safety factors are applied during the design of structural parts, and final failure is undesired. Mechanically, the chosen representative specimens with different CF bundle orientations behave overall similarly, except in the final region, as the overlay of the stress-strain curves shows.

However,the fracture strain and strength of the two shown specimens resemble the upper and lower limits of the standard deviation within each configuration. The average fracture strain and strength values of both configurations are similar. Up to 2.5% strain (the final failure of the depicted specimen with bundles in 90°-direction), the chosen specimens have a representative mechanical behaviour.

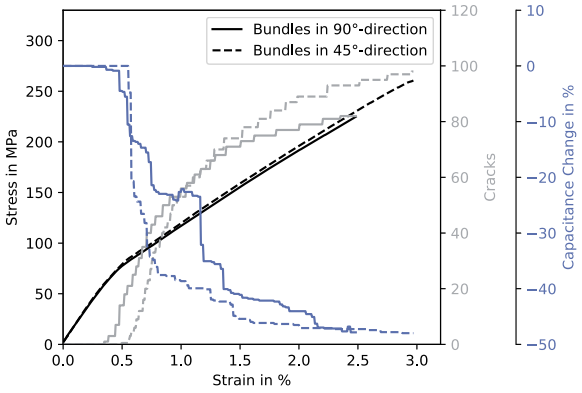

Figure 5.21: Plots showing stress in MPa, capacitance change in % and counted cracks over strain for tensile tests on specimens with $[90_2/0/45_2]_s$-lay-up and conductors either in the 90°-layers or the 45°-layer

Figures 5.22 and 5.23 show photographs of specimens of both configurations at three different times - at the beginning of the tensile test (0 MPa, the start of matrix cracking in the 90°-layers, and the start of matrix cracking in the 45°-layer. The cracks in the monitored areas are marked with blue lines for better visibility. The monitored area in both representative specimens consists of interleaved capacitors composed of five CF bundles. The images demonstrate a similar crack evolution in representative specimens of both configurations. The CF bundles' orientation thus does not significantly influence the failure behaviour. First matrix cracks in the 90°-layers of both configurations initiate at about 55 MPa and 0.32% strain. The crack onset of the matrix cracks in the 45°-layer is at approximately 80 MPa and 0.5% strain. The gray lines in Figure 5.21 resemble the cracks counted between the contacted CF bundles. As the crack development and spacing is similar in the two configurations, the solid crack curve of the samples with CF bundles in the 90°-layers shows only the counted 90°-matrix cracks, whereas the dashed crack curve presents the counted matrix cracks in the 45°-direction. The first increase of the dashed line, which represents the crack initiation in the 45°-layer, is thus delayed compared to the solid curve.

Since the mechanical behaviour up to shortly before failure and the crack initiation and development are similar for both configurations independent of the conductor orientation, an overlay of the results is reasonable, and the capacitance decreases can also be compared (see Figure 5.21). The principal course of the measured capacitance changes is similar to the capacitance decreases found in $[0/90_4]_s$ specimens. Samples with CF bundles in 90°-layers show a measurable capacitance decrease from approx. 0.32% strain onwards. On the other hand, in samples with a 45°-conductor direction, the measurable capacitance decrease starts only from approx. 0.5% strain onwards. With crack initiation in the respective layer, the capacitance starts decreasing. The comparatively late capacitance decrease in the samples with 45°-conductor direction can be explained by the fact that there is a later crack initiation in the 45°-layer due to the laminate structure. An integration of CF bundles in specific layers allows distinct crack monitoring.

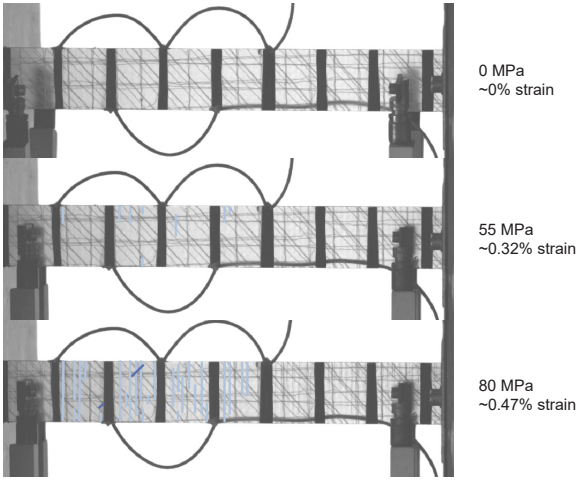

Figure 5.22: Crack evolution in a representative $[90_{C2}/0/45_2]_s$ specimen with conductors in the 90°-layers

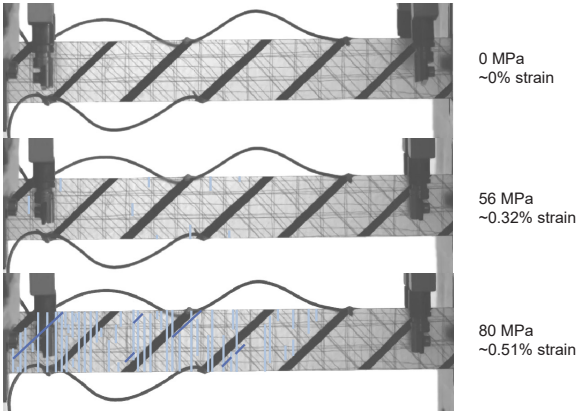

Figure 5.23: Crack evolution in a representative $[90_2/0/45_{C2}]_s$ specimen with conductors in the 45°-layers

The developed analytical model is also applicable to specimens with 45°-conductor orientation using the respective geometrical parameters. As the influence of strain on the distance between the conductors is negligibly small and not resolved by the measurements in step-wise tests, the analytical modelling only

includes the developed cracks according to Equation (5.6). As shown in Figure 5.24, the analytical modelling and the measured capacitance decrease correspond well. The shape of the measured capacitance decrease is similar to the calculated prediction from the analytical model. As for specimens with 90°-CF bundles with 18 mm spacing, the capacitance decrease is measurable over the whole course of the tests. No saturating effect is visible as found for specimens with higher conductor distances. The crack development results in a measurable decrease in capacitance during the whole course of the test. The analytical modelling thus corresponds approximately to the experimental decrease during the entire test. Crack openings between 10 µm and 15 µm result in realistic analytical modelling, considering the standard deviations of the capacitance decrease measured in various samples. Figure 5.24b) displays fewer steps in the capacitance decrease in step-wise tests on specimens with 45°-conductor orientation than found in specimens with 90°-conductor orientation (compare Figure 5.20). As the crack initiation in the 45°-layer starts around 0.5% strain, no cracks and therefore no capacitance decrease is present during the first three load steps.

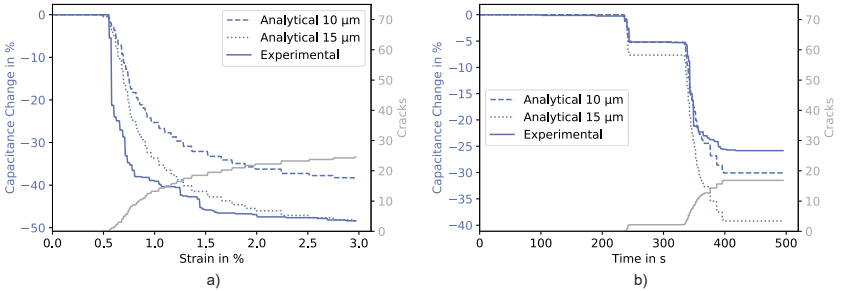

Figure 5.24: Measured capacitance decrease of a CF conductor specimen compared with analytical modelling as ideal plate capacitor with dielectric property change due to air introduced by cracks for crack openings 10 µm (dashed line) and 15 µm (dotted line) and distance change due to strain for tensile tests on $[90_2/0/45_2]_s$ specimens with conductors in the 45°-layer - a) quasi-static test and b) step-wise test

In theory, a simultaneous in-situ measurement of bundles in different layers is possible as long as an insulating layer is present such that the conductors do not have a conductive connection. However, a superposition effect of the measurement devices must be avoided. Using two non-synchronised Peaktech® P 2170 LCR meters for simultaneous capacitance measurements on integrated 90°- and

45°-CF bundles within the same sample led to undesired sinusoidal interference oscillations superimposing the measurements due to an influence of the LCR meters on each other. The effects can be eliminated using one device suitable for multi-channel measurements.
Nevertheless, the overlay of measurements performed on samples with equal lay-up and different conductor orientations proves the potential of localised damage monitoring in individual laminate layers and thus damage evolution monitoring of composites. The flexible integration of CF bundles in various distances, layers, and orientations offers high design freedom and allows for tailored SHM.

5.2.3 Detection of Impact Damage

The previous sections have proven the detectability of matrix cracks in GFRPs during tensile tests using capacitance measurements on integrated CF bundles. Within this section, the method is evaluated regarding the detection of impact damages. Impact damages are critical for composite materials, as they might lead to extensive delaminations, which often cannot be detected by visible inspection of painted parts.
Figure 5.25 shows representative impacted specimens' scans for the three impact energies 7 J, 11 J, and 16 J. The impact results in delaminations and matrix cracks in the 90°- and 0°-directions in the delaminated areas. The determined delamination sizes for different impact energies are depicted in Figure 5.26, including standard deviations. The standard deviations overlap slightly, but the scans in Figure 5.25 and the bar plot in Figure 5.26 still show a clear increase of delamination area with increasing impact energy. The delamination areas mostly remain in between the two CF conductors. However, for impact energies of 16 J, the delaminations tend to span into the CF conductors in some samples.

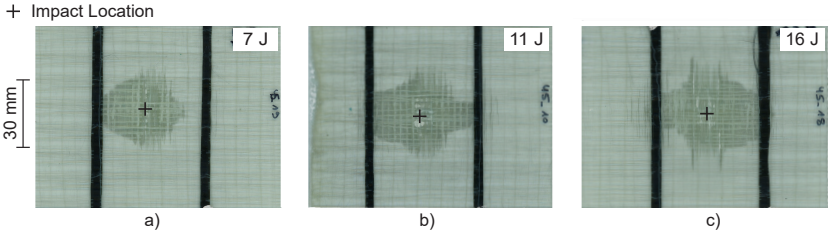

Figure 5.25: Three representative damaged specimens for impact energies of a) 7 J, b) 11 J, and c) 16 J

Similar to the tensile specimens, an undamaged sample's idealised theoretical capacitance can be calculated as 1.18 pF using the standard formula of a plate capacitor (compare Equation (5.2)), the respective geometrical values and the measured relative permittivity $\epsilon_{\mathrm{r,GFRP}}$ of 46 as described in Section 5.2.1. The calculated value is in good agreement with the mean measured value of 1.3 pF. The deviations can be attributed to variations of the real test specimen from the idealised theory as discussed for the tensile specimens.

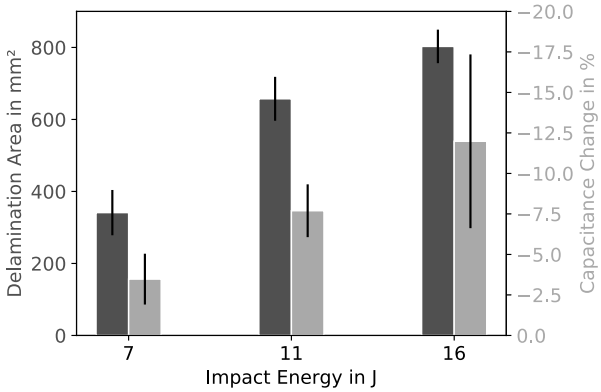

Figure 5.26: Bar plot with resulting delamination area and capacitance change for three impact energies

As no in-situ measurements were possible during the impact, the capacitance change ΔC in percent is calculated by comparing the mean value of the five measurements before the impact $C_{\mathrm{m},0}$ with the mean of the five measurements after the impact C_{m} for each specimen according to Equation (5.8).

$$\Delta C = \frac{C_{\mathrm{m}} - C_{\mathrm{m},0}}{C_{\mathrm{m},0}} 100 \tag{5.8}$$

The capacitance decreases resulting from the impacts are also shown in the bar plot in Figure 5.26 using the second y-axis. The values on this axis are negative - a higher decrease is depicted by a higher bar. A direct comparison proves the same trends for delamination area and capacitance change. A qualitative correlation is clearly possible - higher damage area leads to higher capacitance decrease. For the lowest impact energy of 7 J, the capacitance decrease is the lowest, with a value of $-3.48 \pm 1.36\%$. The second-largest change in capacitance

is found for the samples with an impact energy of 11 J. Here, the capacitance change is $-7.7 \pm 1.40\%$. For the highest energy of 16 J, the largest value of the capacitance change is obtained with an average value of $-12 \pm 4.88\%$. The high standard deviation of the capacitance change for the highest impact energy can be attributed to the delaminations extending into the CF conductors and even further in some samples. The standard deviations of capacitance change overlap slightly for 11 J and 16 J. However, a clear distinction can be made between 7 J and 11 J impacts as well as between 7 J and 16 J impacts when comparing the capacitance decrease.

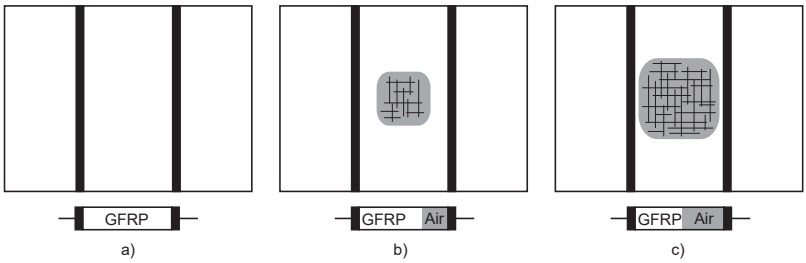

Figure 5.27: Schematic explanation for capacitance decrease resulting from delaminations - a) undamaged specimen, b) specimen with low impact energy, and c) specimen with higher impact energy

As for the tensile specimens, the capacitance decrease resulting from the impacts is caused by a permittivity change of the material due to the damage. Figure 5.27 shows the influence of the delamination area and crack propagation on the composition of the dielectric and the resulting overall relative permittivity. In the undamaged sample - shown in Figure 5.27a) - the relative permittivity of the GFRP fully determines the permittivity between the CF bundles. The capacitance can be calculated according to Equation (5.5). The delaminations and cracks caused by an impact result in air as a second dielectric medium between the CF bundles as depicted in Figure 5.27b). The bigger the delamination area and the more cracks inside the GFRP, the higher the amount of air inside the plate capacitor (see Figure 5.27c)). In theory, as discussed before, the capacitance of a plate capacitor with two dielectric media can be calculated according to Equation (5.5). An analytical relationship between matrix crack number and capacitance change during tensile tests was established using idealised rectangular cracks spanning the whole thickness and width (see Figure 5.14).

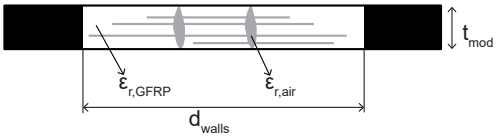

Figure 5.28: Schematic of an idealised plate capacitor formed between CF conductors in 90°-layer of an impact specimen including delaminations and matrix cracks

In the case of impacts, the respective theoretical distances of the dielectrics between the bundles d_{GFRP} and d_{air} are hard to derive since the delaminations do not span the whole laminate thickness and tend to reach different widths between certain laminate layers, as shown in Figure 5.28. However, all existing damages - delaminations and cracks in 90°- and 0°-directions - influence the measured capacitance decrease. Indeed, no clear quantitative correlation between delamination size and theoretical capacitance was possible with the simple formula for a plate capacitor with two dielectric media given in Equation (5.5).
Nevertheless, the results show that a size estimation of impact damages is possible via the amount of capacitance decrease. With further improvements of the measurements, a more precise correlation might be possible. Although all measurements in this study were taken before and after the impacts due to safety requirements, in practice, in-situ measurements are possible, as the tensile tests showed. In-situ measurements provide the advantage that they are not influenced by disconnecting and reconnecting of the measurement system. The influences were eliminated as far as possible; nevertheless, some effects on the results might be present and could result in a higher scatter.

5.2.4 Layout Suggestions and Further Applications

The presented results show that the bundle layout has to be defined according to the sensing requirements. Therefore, some layout suggestions will be presented and discussed.
In general, CF bundles can be integrated for global monitoring of a whole part or locally in areas where damages are expected e.g. due to stress concentrations. Different measurement patterns like interleaved or individual capacitors reveal more information about damage severity and location. Figure 5.29 shows an ex-

emplary schematic of a part including many CF bundles. For simplicity reasons, the bundles are integrated into only one layer and direction.

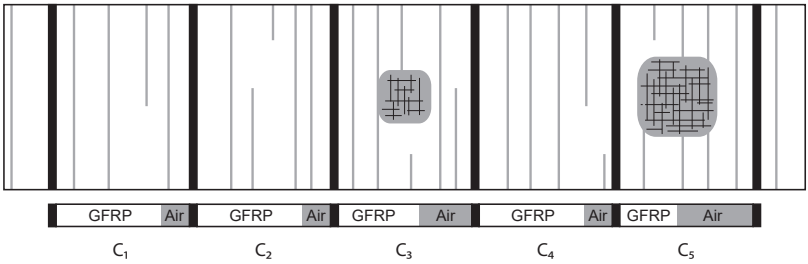

Figure 5.29: Schematic of a specimen including various damages and CF bundles

Global monitoring of a part can be performed by single measurements on many bundles contacted as an interleaved capacitor. The contacting as interleaved capacitor was used for the tensile specimens and discussed in Section 5.2.2. The capacitance decrease measured with an interleaved capacitor determines an accumulation of all damages between the contacted bundles and therefore an average damage severity. Additional measurements on individual capacitors allow for damage localisation. As shown within this work, impact damages result in capacitance decreases within the range of capacitance decreases measured during crack evolution of matrix cracks. Nevertheless, a distinction between matrix crack saturation and extensive delaminations is desired. Such a distinction could e.g. be achieved by comparing the average capacitance decrease measured in the interleaved capacitor and separate measurements on every single capacitor. The measurements between two CF bundles which include delaminations due to impact damage will exhibit a higher capacitance decrease than the average capacitance decrease resulting from the interleaved measurements. For the example illustrated in Figure 5.29, the capacitance decreases ΔC_1, ΔC_2, and ΔC_4 are lower than the average decrease measured in the interleaved capacitor. In contrast, the capacitors C_3 and C_5 show a higher decrease due to the higher amount of enclosed air. Therefore, it can be concluded that further damage exists in the areas of C_3 and C_5, which depending on the severity of the capacitance decrease and the defined thresholds may require further investigations or actions.

Furthermore, Forintos et al. [67] showed that resistance measurements along

integrated CF bundles allow for in-situ deformation and load monitoring of GFRPs. The lower elongation at break of the CF bundles offers the possibility to predict the failure of a GFRP component via detection of CF bundle fracture in electrical measurements. In practice, such different measurements can be achieved using specific electric circuits including multiplexers, and therefore do not require a complex wire routing.

An integration of bundles in differently oriented layers enables further damage evolution monitoring and an assessment of the damage severity. Since matrix cracks in the 90°-layers are mostly a first tolerable form of damage, while matrix cracks, known as splitting, in the 0°-layers usually occur shortly before the laminate fails, a capacitance decrease measured in the 90°-layer is less alarming than a capacitance decrease in the 0°-layer that indicates an imminent failure. By monitoring various layers, threshold values can be set according to more conditions.

The proposed SHM method evaluates permittivity changes within the material to evaluate damage evolution. In general, all effects affecting the material's permittivity can be monitored. Various researchers have found an influence of moisture on the relative permittivity of (filled) polymers and GFRPs [102, 187–189]. Impedance measurements and electrical impedance spectroscopy have successfully been used for moisture monitoring in FRPs [44, 101, 102, 190]. Salas et al. [112] showed moisture monitoring in epoxy and FRPs using commercial integrated capacitive sensors. Therefore, the integrated CF bundles are also suitable for moisture uptake monitoring. With integration in different layers, a moisture progression into the material might be measurable.

5.3 Conclusion

The presented, novel method of SHM using capacitance measurements on integrated conductors in GFRPs provides the means for in-situ damage state monitoring without significantly influencing the mechanical properties. Therefore, the working hypothesis of this chapter is clearly fulfilled.

The local integration of electrically conductive fibres enables in-situ damage detection in GFRPs.

The initiation and evolution of matrix cracks in GFRPs clearly correlate with the in-situ capacitance measurements on integrated CF conductors, as demonstrated in tensile tests. The stiffness decrease due to the matrix cracks visible as knee point in the stress-strain curve can precisely be detected by a drastic capacitance decrease. The capacitance decreases more severely when many matrix cracks form, and less the more saturated the cracks are in the specimen. The capacitance decrease can be explained by the resulting permittivity change due to the lower relative permittivity of air within the formed cracks compared to intact GFRPs. Step-wise tests confirm that the capacitance decrease due to cracks is mostly irreversible during unloading. Consequently, the presented method is capable of in-situ damage monitoring as well as damage state estimation with knowledge of capacitance decrease at specific points during the lifetime.
A high surface area of the conductors, as given in the case of CF conductors, shows beneficial results for crack detection sensitivity compared to stranded and solid copper conductors. Solid copper conductors mainly exhibit a distance-driven linear effect with a lower irreversible change due to cracks. Both copper conductors show a significant loss of Young's modulus due to resin-rich areas. Therefore, CF conductors are the most suitable and material-conforming conductor choice.
Analytical modelling of the experimental values is possible with assumptions of an ideal plate capacitor, considering the distance change of the capacitor plates and the permittivity changes caused by the formation of cracks.
A higher distance or lower thickness of the conductors results in a lower sensitivity towards the end of the test, when a more diffuse crack pattern is present. Reasonable limits have to be defined following the trade-off between sensitivity requirements and cost-efficiency as a consequence of fewer CF rovings.

Integration of conductors in layers with different orientations proves the potential of localised damage monitoring in individual laminate layers. The capacitance decrease correlates with matrix crack development in the respective layers. Hence, the damage evolution of composites can precisely be monitored by a suitable conductor layout and contacting pattern.
Furthermore, a detection and size estimation of impact damages in GFRPs can be achieved. The formation of delaminations results in a capacitance decrease as the material's permittivity changes due to the enclosed air. Higher impact energies lead to larger delamination areas and higher capacitance decreases. Therefore, a correlation between capacitance decrease and delamination area can be established. Consequently, size estimation of the impact damages is possible. In general, all effects influencing the material's permittivity can be detected using the presented SHM method. Therefore, the method should also be suitable for moisture absorption detection in GFRPs as water intrusion significantly alters the material's permittivity [102, 189].
Overall, the method provides a cheap and easy way of in-situ damage monitoring in GFRPs that can be applied in large composite structures and inaccessible locations. The integration of CF bundles offers considerable design freedom and can be carried out locally in highly loaded areas or large parts of the structure. Different contacting patterns provide various damage monitoring and localisation possibilities. Fabrics with the desired amount and distance of CF rovings can industrially be produced and used in standard infusion processes. By embedding the conductors at different locations, layers, and material depths, the proposed method enables localised SHM within the structure. The method does not require large or expensive measuring equipment, as the used LCR meter shows. In practice, small, inexpensive LCR measurement boards could be used, which can be attached to the components without a large weight increase or extensive space requirements. Higher accuracy and sensitivity of the results might be obtained by using a measuring device tuned to the exact, monitored capacitance range.

6 Summary and Conclusion

The presented results provide novel, valuable insights into the electrical SHM of non-conductive GFRP composites. The results of this work clearly confirm the following research hypothesis:

Real-time damage detection and evaluation of GFRP structures can be achieved using in-situ electrical measurements.

Two different methods for damage detection and assessment of GFRPs have been presented. The first method shows a local matrix modification using pre-cured CNT/epoxy thin-films as fully-integrated strain and damage sensors. The second approach is based on a local replacement of glass fibre rovings by conductive fibres. Both approaches allow highly tailored SHM and damage detection in GFRPs without mechanical property loss.

The fully-integrated CNT/epoxy thin-film sensors exhibit a piezoresistive effect that allows a correlation of stress or strain and electrical resistance change. The high sensor design freedom enables monitoring of GFRPs over large material sections or selectively in highly loaded areas. Various tests proved mostly insignificant or even positive effects on the mechanical properties for different load cases and lay-ups. The pre-cured CNT/epoxy films sufficiently bond with the surrounding matrix and do not act as separators or delamination initiators.
In general, tensile strains result in a strain-proportional resistance increase. In contrast, compressive stresses lead to a resistance decrease which is anti-proportional to the applied stress. Step-wise tests showed that the resistance change is mostly reversible for specimens without induced damage. Damages as matrix cracks that result in remaining local strains lead to irreversible resistance changes during unloading. A strong resistance increase towards the end of tensile tests on CP samples can clearly be attributed to crack opening after crack saturation, as DIC images proved.

The sensor films can reliably monitor areas with local stress concentrations, e.g. around the holes in OHT tests. The sensitivity of the measurements can be improved by adapting the shape of the sensors to the expected stress concentration area. Integrating the sensor films between different layers provides information about the failure process, including developing delaminations.
First durability studies with applied cyclic tension-tension fatigue loads showed promising results. The film sensors do not fail prematurely, and a resistance increase is measurable until final specimen failure. The applied load level influences the maximum resistance shortly before final failure. Further studies are necessary with combined quasi-static and fatigue loads as well as different load levels.
Crippling tests on a GFRP stringer with applied compressive load and integrated sensor films demonstrated the ability to detect critical buckling in larger components. Buckling results in an increasing resistance curve during compression as likewise found for compressive specimens on coupon level.
Consequently, the presented, fully-integrated, pre-cured CNT/epoxy thin-film sensors have comprehensively proven to fulfil the following sub-research hypothesis:

The local matrix modification with fully-integrated sensor films allows strain and damage monitoring in GFRPs by electrical measurements.

The second approach presents a novel method of SHM in GFRPs using integrated fibrous conductors as capacitor walls for in-situ damage detection by means of capacitance change. The damage state monitoring is based on capacitance changes due to damage-induced material permittivity changes. Material damages with enclosed air result in a capacitance decrease due to lower relative permittivity of air compared to intact GFRPs.
In-situ capacitance measurements on integrated CF conductors correlate with the initiation and evolution of matrix crack during tensile tests. A drastic capacitance decrease resembles the rapid crack development directly after crack initiation, which correlates with a stiffness drop visible as knee point in the stress-strain curve. Slower crack development results in a moderate capacitance decay. Step-wise tests confirm that the capacitance decrease is mostly irreversible during unloading.
An analytical model with the assumptions of an ideal plate capacitor is suitable to reliably model the capacitance drop as a function of the number of matrix

cracks. Therefore, damage state assessment is possible using the measured capacitance decrease.
CF bundles are a material-conforming conductor choice as they show a sufficient bonding with the surrounding epoxy matrix and do not significantly alter the composite's mechanical properties when integrated in 90°-layers. Stranded and solid copper conductors induce significantly smaller sensitivity and a reduced Young's modulus due to resin-rich areas in the conductors' vicinity.
A higher distance or lower thickness of the CF conductors results in a lower sensitivity of the capacitance decrease, especially for higher crack saturation with more diffuse crack patterns. Consequently, a suitable conductor pattern has to be defined regarding sensitivity requirements and cost-efficiency. The integration of the CF bundles with the desired distances can be carried out directly during the industrial manufacturing process of glass fibre fabrics.
Integration of conductors in differently oriented laminate layers allows monitoring of the crack development within the respective layers. Therefore, the damage evolution within the whole composite can be monitored and evaluated with a suitable conductor and contacting pattern.
Additionally, damage detection and size estimation of impact damages are also possible with this method. Similar to matrix cracks, air enclosed in the delaminations results in a capacitance decrease. Larger delaminations with more enclosed air lead to a bigger capacitance drop.
Consequently, in-situ capacitance measurements enable the detection of various critical damage modes. In general, the method is suitable for monitoring all effects that influence the material's relative permittivity, including e.g. moisture absorption.
In summary, the experimental results clearly verify the following sub-research hypothesis:

The local integration of electrically conductive fibres enables in-situ damage detection in GFRPs.

Both developed sensing approaches allow for real-time, in-situ SHM without significantly altering the mechanical properties. No foreign body effect is present as the sensors are chemically similar and compatible materials. The methods allow for highly tailored SHM and do not require large or expensive measurement equipment. The manufacturing is easily automatable and can be applied in established, industrial large-scale processes. Therefore, the presented approaches

fulfil the numerous requirements for SHM systems (compare Chapter 1). The advances in electrical SHM presented within this thesis enable safer and more efficient use of GFRP components.

Prior to industrial application, further investigations are advisable. Long-term tests under combined load cases and varying environmental conditions might provide meaningful results regarding the stability and accuracy of the sensors. Especially, the consequences of superposition of different damage modes and environmental influences on the electrical measurements and sensing results should be the subject of further research. Different sensor designs and contacting patterns have proven to affect the sensitivity significantly. Therefore, further sensitivity studies on bigger parts are beneficial for effective use. In addition, contacting possibilities in large components should also be comprehensively studied in order to provide straightforward and reliable electrical contacting.
In theory, an advantageous combination of both sensor types is possible as long as an isolating glass fibre or resin layer separates the sensors, such that no conductive connection exists. However, the sensing abilities and influencing effects when combing the sensor types have to be investigated and evaluated.

Bibliography

[1] M. Kupke, K. Schulte, and R. Schüler. “Non-destructive testing of FRP by d.c. and a.c. electrical methods”. In: *Composites Science and Technology* 61.6 (2001), pp. 837–847. ISSN: 0266-3538. DOI: 10.1016/S0266-3538(00)00180-9.

[2] L. Böger, M. H. G. Wichmann, L. O. Meyer, and K. Schulte. “Load and health monitoring in glass fibre reinforced composites with an electrically conductive nanocomposite epoxy matrix”. In: *Composites Science and Technology* 68.7 (2008), pp. 1886–1894. ISSN: 0266-3538. DOI: 10.1016/j.compscitech.2008.01.001.

[3] E. T. Thostenson and T.-W. Chou. “Real-time in situ sensing of damage evolution in advanced fiber composites using carbon nanotube networks”. In: *Nanotechnology* 19.21 (2008), p. 215713. DOI: 10.1088/0957-4484/19/21/215713.

[4] I. A. Ventura, J. Zhou, and G. Lubineau. “Drastic modification of the piezoresistive behavior of polymer nanocomposites by using conductive polymer coatings”. In: *Composites Science and Technology* 117 (2015), pp. 342–350. ISSN: 0266-3538. DOI: 10.1016/j.compscitech.2015.07.007.

[5] S. W. Doebling, C. R. Farrar, M. B. Prime, and D. W. Shevitz. *Damage identification and health monitoring of structural and mechanical systems from changes in their vibration characteristics: A literature review*. 1996. DOI: 10.2172/249299.

[6] K. Worden and J. M. Dulieu-Barton. “An Overview of Intelligent Fault Detection in Systems and Structures”. In: *Structural Health Monitoring* 3.1 (2004), pp. 85–98. DOI: 10.1177/1475921704041866.

[7] C. R. Farrar and K. Worden. “An introduction to structural health monitoring”. In: *Philosophical transactions. Series A, Mathematical, physical, and engineering sciences* 365.1851 (2007), pp. 303–315. ISSN: 1364-503X. DOI: 10.1098/rsta.2006.1928.

[8] K. Schulte and Ch. Baron. “Load and failure analyses of CFRP laminates by means of electrical resistivity measurements”. In: *Composites Science and Technology* 36.1 (1989), pp. 63–76. ISSN: 0266-3538. DOI: 10.1016/0266-3538(89)90016-X.

[9] J. C. Abry, S. Bochard, A. Chateauminois, M. Salvia, and G. Giraud. “In situ detection of damage in CFRP laminates by electrical resistance measurements”. In: *Composites Science and Technology* 59.6 (1999), pp. 925–935. ISSN: 0266-3538. DOI: 10.1016/S0266-3538(98)00132-8.

[10] K. Takahashi and H. T. Hahn. “Towards practical application of electrical resistance change measurement for damage monitoring using an addressable conducting network”. In: *Structural Health Monitoring* 11.3 (2012), pp. 367–377. DOI: 10.1177/1475921711424519.

[11] T. Augustin, D. Grunert, H. H. Langner, V. Haverkamp, and B. Fiedler. “Online monitoring of surface cracks and delaminations in carbon fiber/epoxy composites using silver nanoparticle based ink”. In: *Advanced Manufacturing: Polymer & Composites Science* 3.3 (2017), pp. 110–119. DOI: 10.1080/20550340.2017.1362508.

[12] C. Buggisch, D. Gibhardt, N. Felmet, Y. Tetzner, and B. Fiedler. “Strain sensing in GFRP via fully integrated carbon nanotube epoxy film sensors”. In: *Composites Part C: Open Access* 6.8 (2021), p. 100191. ISSN: 26666820. DOI: 10.1016/j.jcomc.2021.100191.

[13] C. Buggisch, A. Gagani, and B. Fiedler. “Capacitance measurements on integrated conductors for detection of matrix cracks in GFRP”. In: *Functional Composite Materials* 2.1 (2021), p. 2. ISSN: 2522-5774. DOI: 10.1186/s42252-020-00013-x.

[14] C. Buggisch, D. Gibhardt, M. Kern, and B. Fiedler. “Impact damage detection in glass fibre reinforced polymers via electrical capacitance measurements on integrated carbon fibre bundles”. In: *Composites Communications* 30 (2022), p. 101090. ISSN: 24522139. DOI: 10.1016/j.coco.2022.101090.

[15] W. J. Staszewski, C. Boller, and G. R. Tomlinson, eds. *Health monitoring of aerospace structures: Smart sensor technologies and signal processing*. Chichester, West Sussex, England and Hoboken, NJ: J. Wiley, 2004. ISBN: 0470092831. DOI: 10.1002/0470092866.

[16] C. Boller, F.-K. Chang, and Y. Fujino, eds. *Encyclopedia of structural health monitoring*. Hoboken, NJ: Wiley Interscience, 2009. ISBN: 9780470058220. DOI: 10.1002/9780470061626.

[17] H. Czichos, ed. *Handbook of Technical Diagnostics: Fundamentals and Application to Structures and Systems*. Berlin, Heidelberg: Springer Berlin Heidelberg, 2013. ISBN: 9783642258503.

[18] K. Diamanti and C. Soutis. "Structural health monitoring techniques for aircraft composite structures". In: *Progress in Aerospace Sciences* 46.8 (2010), pp. 342–352. ISSN: 0376-0421. DOI: 10.1016/j.paerosci.2010.05.001.

[19] J. Cai, L. Qiu, S. Yuan, L. Shi, P. Liu, and D. Liang. "Structural Health Monitoring for Composite Materials". In: *Composites and Their Applications*. Ed. by N. Hu. InTech, 2012. ISBN: 978-953-51-0706-4. DOI: 10.5772/48215.

[20] V. Giurgiutiu. *Structural health monitoring of aerospace composites*. Amsterdam, Boston, and Heidelberg: Academic Press an imprint of Elsevier, 2016. ISBN: 9780124096059.

[21] H. Choi, S. Choi, and H. Cha. "Structural Health Monitoring system based on strain gauge enabled wireless sensor nodes". In: *2008 5th International Conference on Networked Sensing Systems*. 2008, pp. 211–214. DOI: 10.1109/INSS.2008.4610888.

[22] S. Tsiapoki, M. W. Häckell, T. Grießmann, and R. Rolfes. "Damage and ice detection on wind turbine rotor blades using a three-tier modular structural health monitoring framework". In: *Structural Health Monitoring* 17.5 (2018), pp. 1289–1312. DOI: 10.1177/1475921717732730.

[23] S. W. Doebling, C. R. Farrar, and M. B. Prime. "A Summary Review of Vibration-Based Damage Identification Methods". In: *The Shock and Vibration Digest* 30.2 (1998), pp. 91–105. ISSN: 0583-1024. DOI: 10.1177/058310249803000201.

[24] S. Wernitz, D. Pache, T. Griesmann, and R. Rolfes. “Damage Localization with SP2E Under Changing Conditions”. In: *Structural health monitoring 2019*. Ed. by F.-K. Chang, A. Güemes, and F. Kopsaftopoulos. Lancaster, Pennsylvania, U.S.A.: DEStech Publications Inc, 2019. ISBN: 978-1-60595-601-5. DOI: 10.12783/shm2019/32505.

[25] D. Montalvao. “A Review of Vibration-based Structural Health Monitoring with Special Emphasis on Composite Materials”. In: *The Shock and Vibration Digest* 38.4 (2006), pp. 295–324. ISSN: 0583-1024. DOI: 10.1177/0583102406065898.

[26] H. Sohn, C. R. Farrar, F. M. Hemez, and J. J. Czarnecki. “A Review of Structural Health Review of Structural Health Monitoring Literature 1996-2001”. In: *University of North Texas Libraries, UNT Digital Library* (2002). URL: https://digital.library.unt.edu/ark:/67531/metadc927238/ (visited on 02/01/2022).

[27] B. Lin and V. Giurgiutiu. “Modeling and testing of PZT and PVDF piezoelectric wafer active sensors”. In: *Smart Materials and Structures* 15.4 (2006), pp. 1085–1093. DOI: 10.1088/0964-1726/15/4/022.

[28] H. Lamb. “On waves in an elastic plate”. In: *Proceedings of the Royal Society of London. Series A, Containing Papers of a Mathematical and Physical Character* 93.648 (1917), pp. 114–128. DOI: 10.1098/rspa.1917.0008.

[29] E. Moreno and P. Acevedo. “Thickness measurement in composite materials using Lamb waves”. In: *Ultrasonics* 35.8 (1998), pp. 581–586. ISSN: 0041624X. DOI: 10.1016/S0041-624X(97)00071-1.

[30] T.-T. Wu and Y.-H. Liu. “On the measurement of anisotropic elastic constants of fiber-reinforced composite plate using ultrasonic bulk wave and laser generated Lamb wave”. In: *Ultrasonics* 37.6 (1999), pp. 405–412. ISSN: 0041624X.

[31] S. S. Kessler, S. M. Spearing, and C. Soutis. “Damage detection in composite materials using Lambwave methods”. In: *Smart Materials and Structures* 11.2 (2002), p. 269. ISSN: 0964-1726. DOI: 10.1088/0964-1726/11/2/310.

[32] R. S. Gostautas, G. Ramirez, R. J. Peterman, and D. Meggers. "Acoustic Emission Monitoring and Analysis of Glass Fiber-Reinforced Composites Bridge Decks". In: *Journal of Bridge Engineering* 10.6 (2005), pp. 713–721.

[33] R. Gutkin, C. J. Green, S. Vangrattanachai, S. T. Pinho, P. Robinson, and P. T. Curtis. "On acoustic emission for failure investigation in CFRP: Pattern recognition and peak frequency analyses". In: *Mechanical Systems and Signal Processing* 25.4 (2011), pp. 1393–1407. ISSN: 08883270.

[34] C. U. Grosse and M. Ohtsu, eds. *Acoustic Emission Testing*. Berlin, Heidelberg: Springer Berlin Heidelberg, 2008. ISBN: 9783540699729.

[35] K. Peters. "Fiber Bragg Grating Sensors". In: *Encyclopedia of structural health monitoring*. Ed. by C. Boller, F.-K. Chang, and Y. Fujino. Hoboken, NJ: Wiley Interscience, 2009. ISBN: 9780470058220. DOI: 10.1002/9780470061626.shm024.

[36] G. Meltz, W. W. Morey, and W. H. Glenn. "Formation of Bragg gratings in optical fibers by a transverse holographic method". In: *Optics letters* 14.15 (1989), pp. 823–825. ISSN: 0146-9592. DOI: 10.1364/ol.14.000823.

[37] M. Majumder, T. K. Gangopadhyay, A. K. Chakraborty, K. Dasgupta, and D. K. Bhattacharya. "Fibre Bragg gratings in structural health monitoring—Present status and applications". In: *Sensors and Actuators A: Physical* 147.1 (2008), pp. 150–164. ISSN: 0924-4247. DOI: 10.1016/j.sna.2008.04.008.

[38] N. Takeda. "Characterization of microscopic damage in composite laminates and real-time monitoring by embedded optical fiber sensors". In: *International Journal of Fatigue* 24.2 (2002), pp. 281–289. ISSN: 0142-1123. DOI: 10.1016/S0142-1123(01)00083-4.

[39] M. Kreuzer. *Strain measurement with fiber Bragg grating sensors*. 2006.

[40] T. Mizutani, Y. Okabe, and N. Takeda. "Quantitative evaluation of transverse cracks in carbon fiber reinforced plastic quasi-isotropic laminates with embedded small-diameter fiber Bragg grating sensors". In: *Smart Materials and Structures* 12.6 (2003), pp. 898–903. DOI: 10.1088/0964-1726/12/6/006.

[41] S. Laflamme and F. Ubertini. *Back-to-Basics: Self-Sensing Materials for Nondestructive Evaluation*. 2019.

[42] R. Vargas-Bernal and M. Tecpoyotl-Torres. “Nanocomposites for Space Applications”. In: *Diverse applications of organic-inorganic nanocomposites*. Ed. by Gabriele Clarizia and Paola Bernardo. Advances in mechatronics and mechanical engineering (AMME) book series. Hershey, Pennsylvania: IGI Global, 2020, pp. 191–222. ISBN: 9781799815303. DOI: 10.4018/978-1-7998-1530-3.ch008.

[43] A. A. Eddib and D. D. L. Chung. “First report of capacitance-based self-sensing and in-plane electric permittivity of carbon fiber polymer-matrix composite”. In: *Carbon* 140 (2018), pp. 413–427. ISSN: 00086223. DOI: 10.1016/j.carbon.2018.08.070.

[44] R. Sorrentino, L. Di Palma, M. Inverno, and P. Vernillo. “An Impedance Measurement Technique for Composite Materials Moisture Level Detection Devoted to Health Monitoring in Aeronautics”. In: *Journal of Composites Science* 3.3 (2019), p. 76. DOI: 10.3390/jcs3030076.

[45] J. C. Abry, Y. K. Choi, A. Chateauminois, B. Dalloz, G. Giraud, and M. Salvia. “In-situ monitoring of damage in CFRP laminates by means of AC and DC measurements”. In: *Composites Science and Technology* 61.6 (2001), pp. 855–864. ISSN: 0266-3538. DOI: 10.1016/S0266-3538(00)00181-0.

[46] F. Carmona, R. Canet, and P. Delhaes. “Piezoresistivity of heterogeneous solids”. In: *Journal of Applied Physics* 61.7 (1987), pp. 2550–2557. ISSN: 0021-8979. DOI: 10.1063/1.337932.

[47] H. Zhang, E. Bilotti, and T. Peijs. “The use of carbon nanotubes for damage sensing and structural health monitoring in laminated composites: a review”. In: *Nanocomposites* 1.4 (2015), pp. 167–184. DOI: 10.1080/20550324.2015.1113639.

[48] T. Xiao, C. Qian, R. Yin, K. Wang, Y. Gao, and F. Xuan. “3D Printing of Flexible Strain Sensor Array Based on UV–Curable Multiwalled Carbon Nanotube/Elastomer Composite”. In: *Advanced Materials Technologies* 6.1 (2021), p. 2000745. ISSN: 2365-709X. DOI: 10.1002/admt.202000745.

[49] Z.-H. Tang, Y.-Q. Li, P. Huang, H. Wang, N. Hu, and S.-Y. Fu. “Comprehensive evaluation of the piezoresistive behavior of carbon nanotube-based composite strain sensors”. In: *Composites Science and Technology* 208 (2021), p. 108761. ISSN: 0266-3538. DOI: 10.1016/j.compscitech.2021.108761.

[50] M. Kupke, H.-P. Wentzel, and K. Schulte. "Electrically conductive glass fibre reinforced epoxy resin". In: *Materials Research Innovations* 2.3 (1998), pp. 164–169. ISSN: 1432-8917. DOI: 10.1007/s100190050079.

[51] E. T. Thostenson and T.-W. Chou. "Carbon Nanotube Networks: Sensing of Distributed Strain and Damage for Life Prediction and Self Healing". In: *Advanced Materials* 18.21 (2006), pp. 2837–2841. ISSN: 09359648. DOI: 10.1002/adma.200600977.

[52] L. Gao, E. T. Thostenson, Z. Zhang, and T.-W. Chou. "Sensing of Damage Mechanisms in Fiber-Reinforced Composites under Cyclic Loading using Carbon Nanotubes". In: *Advanced Functional Materials* 19.1 (2009), pp. 123–130. ISSN: 1616301X. DOI: 10.1002/adfm.200800865.

[53] L. Gao, E. T. Thostenson, Z. Zhang, J.-H. Byun, and T.-W. Chou. "Damage monitoring in fiber-reinforced composites under fatigue loading using carbon nanotube networks". In: *Philosophical Magazine* 90.31-32 (2010), pp. 4085–4099. ISSN: 1478-6435. DOI: 10.1080/14786430903352649.

[54] S. Wu, R. B. Ladani, A. R. Ravindran, J. Zhang, A. P. Mouritz, A. J. Kinloch, and C. H. Wang. "Aligning carbon nanofibres in glass-fibre/epoxy composites to improve interlaminar toughness and crack-detection capability". In: *Composites Science and Technology* 152 (2017), pp. 46–56. ISSN: 0266-3538. DOI: 10.1016/j.compscitech.2017.09.007.

[55] N. D. Alexopoulos, C. Bartholome, P. Poulin, and Z. Marioli-Riga. "Structural health monitoring of glass fiber reinforced composites using embedded carbon nanotube (CNT) fibers". In: *Composites Science and Technology* 70.2 (2010), pp. 260–271. ISSN: 0266-3538. DOI: 10.1016/j.compscitech.2009.10.017.

[56] B. R. Loyola, K. J. Loh, and V. La Saponara. "Static and dynamic strain monitoring of GFRP composites using carbon nanotube thin films". In: *Sensors and Smart Structures Technologies for Civil, Mechanical, and Aerospace Systems 2011*. Ed. by M. Tomizuka. SPIE Proceedings. SPIE, 2011, p. 798108. DOI: 10.1117/12.881006.

[57] B. Pinto, S. Kern, J. J. Ku-Herrera, J. Yasui, V. La Saponara, and K. J. Loh. "A comparative study of a self strain-monitoring carbon nanotube film and carbon fibers under flexural loading by electrical resistance

changes". In: *Journal of Physics: Conference Series* 628 (2015), p. 012098. DOI: 10.1088/1742-6596/628/1/012098.

[58] B. R. Loyola. "14 - In situ sensing in glass fiber-reinforced polymer composites via embedded carbon nanotube thin films". In: *Innovative Developments of Advanced Multifunctional Nanocomposites in Civil and Structural Engineering*. Ed. by K. J. Loh and S. Nagarajaiah. Oxford: Woodhead Publishing, 2016, pp. 327–352. ISBN: 978-1-78242-326-3. DOI: 10.1016/B978-1-78242-326-3.00014-2.

[59] K. Aly, A. Li, and P. D. Bradford. "In-situ monitoring of woven glass fiber reinforced composites under flexural loading through embedded aligned carbon nanotube sheets". In: *Journal of Composite Materials* 52.20 (2018), pp. 2777–2788. DOI: 10.1177/0021998317754128.

[60] G. Yang, X. Feng, W. Wang, Q. OuYang, L. Liu, and Z. Wu. "Graphene and carbon nanotube-based high-sensitive film sensors for in-situ monitoring out-of-plane shear damage of epoxy composites". In: *Composites Part B: Engineering* 204 (2021), p. 108494. ISSN: 13598368. DOI: 10.1016/j.compositesb.2020.108494.

[61] P. Dharap, Z. Li, S. Nagarajaiah, and E. V. Barrera. "Nanotube film based on single-wall carbon nanotubes for strain sensing". In: *Nanotechnology* 15.3 (2004), pp. 379–382. DOI: 10.1088/0957-4484/15/3/026.

[62] P. Dharap, Z. Li, S. Nagarajaiah, and E. V. Barrera. "Flexural strain sensing using carbon nanotube film". In: *Sensor Review* 24.3 (2004), pp. 271–273. ISSN: 0260-2288. DOI: 10.1108/02602280410545399.

[63] I. Kang, M. J. Schulz, J. H. Kim, V. Shanov, and D. Shi. "A carbon nanotube strain sensor for structural health monitoring". In: *Smart Materials and Structures* 15.3 (2006), pp. 737–748. DOI: 10.1088/0964-1726/15/3/009.

[64] B. R. Loyola, V. La Saponara, and K. J. Loh. "In situ strain monitoring of fiber-reinforced polymers using embedded piezoresistive nanocomposites". In: *Journal of Materials Science* 45.24 (2010), pp. 6786–6798. ISSN: 0022-2461. DOI: 10.1007/s10853-010-4775-y.

[65] B. M. Lee, S. Gupta, K. J. Loh, and S. Nagarajaiah. "Strain sensing and structural health monitoring using nanofilms and nanocomposites". In: *Innovative Developments of Advanced Multifunctional Nanocompos-*

ites in Civil and Ctructural Engineering. Ed. by K. J. Loh and S. Nagarajaiah. Woodhead Publishing series in civil and structural engineering. Duxford, UK: Elsevier Woodhead Publishing, 2016, pp. 303–326. ISBN: 9781782423263. DOI: 10.1016/B978-1-78242-326-3.00013-0.

[66] D. Zymelka, K. Togashi, and T. Kobayashi. "Carbon-based printed strain sensor array for remote and automated structural health monitoring". In: *Smart Materials and Structures* 29.10 (2020), p. 105022. DOI: 10.1088/1361-665x/aba81c.

[67] N. Forintos, T. Sarkadi, and T. Czigany. "Electric resistance measurement–based structural health monitoring with multifunctional carbon fibers: Predicting, sensing, and measuring overload". In: *Composites Communications* 28 (2021), p. 100913. ISSN: 24522139. DOI: 10.1016/j.coco.2021.100913.

[68] N. Wiegand and E. Mäder. "Multifunctional Interphases: Percolation Behavior, Interphase Modification, and Electro-Mechanical Response of Carbon Nanotubes in Glass Fiber Polypropylene Composites". In: *Advanced Engineering Materials* 18.3 (2016), pp. 376–384. ISSN: 14381656. DOI: 10.1002/adem.201500447.

[69] M. T. Müller, H. F. Pötzsch, U. Gohs, and G. Heinrich. "Online Structural-Health Monitoring of Glass Fiber-Reinforced Thermoplastics Using Different Carbon Allotropes in the Interphase". In: *Materials (Basel, Switzerland)* 11.7 (2018). ISSN: 1996-1944. DOI: 10.3390/ma11071075.

[70] J. Sebastian, N. Schehl, M. Bouchard, M. Boehle, L. Li, A. Lagounov, and K. Lafdi. "Health monitoring of structural composites with embedded carbon nanotube coated glass fiber sensors". In: *Carbon* 66.3 (2014), pp. 191–200. ISSN: 00086223. DOI: 10.1016/j.carbon.2013.08.058.

[71] S.-L. Gao, R.-C. Zhuang, J. Zhang, J.-W. Liu, and E. Mäder. "Glass Fibers with Carbon Nanotube Networks as Multifunctional Sensors". In: *Advanced Functional Materials* 20.12 (2010), pp. 1885–1893. ISSN: 1616301X. DOI: 10.1002/adfm.201000283.

[72] H. Zhang, M. Kuwata, E. Bilotti, T. Peijs, and N. M. Huang. "Integrated Damage Sensing in Fibre-Reinforced Composites with Extremely Low Carbon Nanotube Loadings". In: *Journal of Nanomaterials* 2015 (2015), p. 785834. ISSN: 1687-4110. DOI: 10.1155/2015/785834.

[73] S. Nag-Chowdhury, H. Bellegou, I. Pillin, M. Castro, P. Longrais, and J. F. Feller. "Non-intrusive health monitoring of infused composites with embedded carbon quantum piezo-resistive sensors". In: *Composites Science and Technology* 123 (2016), pp. 286–294. ISSN: 0266-3538. DOI: 10.1016/j.compscitech.2016.01.004.

[74] J. A. Rodríguez-González, C. Rubio-González, and J. A. Soto-Cajiga. "Piezoresistive Response of Spray-coated Multiwalled Carbon Nanotube/Glass Fiber/Epoxy Composites under Flexural Loading". In: *Fibers and Polymers* 20.8 (2019), pp. 1673–1683. ISSN: 1229-9197. DOI: 10.1007/s12221-019-8711-8.

[75] Y.-T. Jung, H. D. Roh, I.-Y. Lee, and Y.-B. Park. "Strain sensing and progressive failure monitoring of glass-fiber-reinforced composites using percolated carbon nanotube networks". In: *Functional Composites and Structures* 2.1 (2020), p. 015006. DOI: 10.1088/2631-6331/ab7bc4.

[76] K. Aly, A. Li, and P. D. Bradford. "Strain sensing in composites using aligned carbon nanotube sheets embedded in the interlaminar region". In: *Composites Part A: Applied Science and Manufacturing* 90 (2016), pp. 536–548. ISSN: 1359835X. DOI: 10.1016/j.compositesa.2016.08.003.

[77] O. G. Kravchenko, D. Pedrazzoli, D. Kovtun, X. Qian, and I. Manas-Zloczower. "Incorporation of plasma-functionalized carbon nanostructures in composite laminates for interlaminar reinforcement and delamination crack monitoring". In: *Journal of Physics and Chemistry of Solids* 112 (2018), pp. 163–170. ISSN: 00223697. DOI: 10.1016/j.jpcs.2017.09.018.

[78] O. G. Kravchenko, D. Pedrazzoli, V. S. Bonab, and I. Manas-Zloczower. "Conductive interlaminar interfaces for structural health monitoring in composite laminates under fatigue loading". In: *Materials & Design* 160.7 (2018), pp. 1217–1225. ISSN: 02641275. DOI: 10.1016/j.matdes.2018.10.045.

[79] A. S. Wu, W.-J. Na, W.-R. Yu, J.-H. Byun, and T.-W. Chou. "Carbon nanotube film interlayer for strain and damage sensing in composites during dynamic compressive loading". In: *Applied Physics Letters* 101.22 (2012), p. 221909. ISSN: 0003-6951. DOI: 10.1063/1.4765654.

[80] P. Slobodian, S. Lloret Pertegás, P. Riha, J. Matyas, R. Olejnik, R. Schledjewski, and M. Kovar. "Glass fiber/epoxy composites with integrated layer of carbon nanotubes for deformation detection". In: *Composites Science and Technology* 156 (2018), pp. 61–69. ISSN: 0266-3538. DOI: 10.1016/j.compscitech.2017.12.012.

[81] A. A. Nassr and W. W. El-Dakhakhni. "Damage Detection of FRP-Strengthened Concrete Structures Using Capacitance Measurements". In: *Journal of Composites for Construction* 13.6 (2009), pp. 486–497. ISSN: 1090-0268.

[82] Y. Wang and D. D. L. Chung. "Capacitance-based defect detection and defect location determination for cement-based material". In: *Materials and Structures* 126.6 (2017), pp. 192–201. ISSN: 1359-5997. DOI: 10.1617/s11527-017-1094-7.

[83] J. Yan, A. Downey, A. Cancelli, S. Laflamme, A. Chen, J. Li, and F. Ubertini. "Concrete Crack Detection and Monitoring Using a Capacitive Dense Sensor Array". In: *Sensors (Basel, Switzerland)* 19.8 (2019). DOI: 10.3390/s19081843.

[84] Y. Cheng, F. Gao, A. Hanif, Z. Lu, and Z. Li. "Development of a capacitive sensor for concrete structure health monitoring". In: *Construction and Building Materials* 149 (2017), pp. 659–668. ISSN: 0950-0618. DOI: 10.1016/j.conbuildmat.2017.05.150.

[85] Y. Cheng, A. Hanif, and Z. Li. "Development of a flexible capacitive sensor for concrete structure health monitoring". In: *Sensors and Smart Structures Technologies for Civil, Mechanical, and Aerospace Systems 2018*. Ed. by H. Sohn. Vol. 10598. SPIE, 2018, pp. 154–162. DOI: 10.1117/12.2306201.

[86] P. Hudec, C. MacInnis, and M. Moukwa. "The capacitance effect method of measuring moisture and salt content of concrete". In: *Cement and Concrete Research* 16.4 (1986), pp. 481–490. ISSN: 0008-8846. DOI: 10.1016/0008-8846(86)90085-2.

[87] A. A. Nassr, W. H. Ahmed, and W. W. El-Dakhakhni. "Coplanar capacitance sensors for detecting water intrusion in composite structures". In: *Measurement Science and Technology* 19.7 (2008), p. 075702.

[88] X. Derobert and J. Iaquinta. “Capacitive Methods for Structural Health Monitoring in Civil Engineering”. In: *Structural health monitoring*. Ed. by A. Güemes, C.-P. Fritzen, and D. Balageas. London and Newport Beach, CA: ISTE, 2006, pp. 463–490. ISBN: 9780470612071. DOI: 10.1002/9780470612071.ch7.

[89] G. Cosoli, A. Mobili, F. Tittarelli, G. M. Revel, and P. Chiariotti. “Electrical Resistivity and Electrical Impedance Measurement in Mortar and Concrete Elements: A Systematic Review”. In: *Applied Sciences* 10.24 (2020), p. 9152. DOI: 10.3390/app10249152.

[90] D. D. L. Chung. “Self-sensing concrete: from resistance-based sensing to capacitance-based sensing”. In: *International Journal of Smart and Nano Materials* 12.1 (2021), pp. 1–19. ISSN: 1947-5411. DOI: 10.1080/19475411.2020.1843560.

[91] X. Yin, D. A. Hutchins, G. G. Diamond, and P. Purnell. “Non-destructive evaluation of concrete using a capacitive imaging technique: Preliminary modelling and experiments”. In: *Cement and Concrete Research* 40.12 (2010), pp. 1734–1743. ISSN: 0008-8846. DOI: 10.1016/j.cemconres.2010.08.015.

[92] P. Chakraborty, N. B. Gundrati, C. Zhou, and D. D. L. Chung. “Effect of stress on the capacitance and electric permittivity of three-dimensionally printed polymer, with relevance to capacitance-based stress monitoring”. In: *Sensors and Actuators A: Physical* 263 (2017), pp. 380–385. ISSN: 0924-4247. DOI: 10.1016/j.sna.2017.07.008.

[93] P. Chakraborty, G. Zhao, C. Zhou, and D. D. L. Chung. “Unprecedented sensing of interlayer defects in three-dimensionally printed polymer by capacitance measurement”. In: *Smart Materials and Structures* 27.11 (2018), p. 115012. DOI: 10.1088/1361-665x/aae16e.

[94] G. G. Diamond, D. A. Hutchins, T. H. Gan, P. Purnell, and K. K. Leong. “Single-sided capacitive imaging for NDT”. In: *Insight - Non-Destructive Testing and Condition Monitoring* 48.12 (2006), pp. 724–730. ISSN: 13542575. DOI: 10.1784/insi.2006.48.12.724.

[95] X. Yin and D. A. Hutchins. “Non-destructive evaluation of composite materials using a capacitive imaging technique”. In: *Composites Part B: Engineering* 43.3 (2012), pp. 1282–1292. ISSN: 13598368. DOI: 10.1016/j.compositesb.2011.10.018.

[96] M. Morozov, W. Jackson, and S. G. Pierce. "Capacitive imaging of impact damage in composite material". In: *Composites Part B: Engineering* 113 (2017), pp. 65–71. ISSN: 13598368. DOI: 10.1016/j.compositesb.2017.01.016.

[97] S. Gupta, H. E. Kim, H. Kim, and K. J. Loh. "Planar capacitive imaging for composite delamination damage characterization". In: *Measurement Science and Technology* 32.2 (2020), p. 024010. ISSN: 0957-0233. DOI: 10.1088/1361-6501/abb484.

[98] S. Amato, D. Hutchins, X. Yin, M. Ricci, and S. Laureti. *Capacitive imaging using fused amplitude and phase information for improved defect detection*. 2021. URL: https://arxiv.org/pdf/2103.14170.

[99] R. Asmatulu, B. Venishetty, and E. Asmatulu. "Non-Destructive Testing of Fiber Reinforced Composite Materials Using a Capacitance Bridge". In: *Proceedings of the ASME International Mechanical Engineering Congress and Exposition - 2009*. New York, NY: ASME, 2010, pp. 171–177. ISBN: 978-0-7918-4384-0. DOI: 10.1115/IMECE2009-12335.

[100] R. Raihan, J.-M. Adkins, J. Baker, F. Rabbi, and K. Reifsnider. "Relationship of dielectric property change to composite material state degradation". In: *Composites Science and Technology* 105 (2014), pp. 160–165. ISSN: 0266-3538. DOI: 10.1016/j.compscitech.2014.09.017.

[101] D. G. Bekas and A. S. Paipetis. "Damage monitoring in nanoenhanced composites using impedance spectroscopy". In: *Composites Science and Technology* 134 (2016), pp. 96–105. ISSN: 0266-3538. DOI: 10.1016/j.compscitech.2016.08.013.

[102] S. A. Grammatikos, R. J. Ball, M. Evernden, and R. G. Jones. "Impedance spectroscopy as a tool for moisture uptake monitoring in construction composites during service". In: *Composites Part A: Applied Science and Manufacturing* 105 (2018), pp. 108–117. ISSN: 1359835X. DOI: 10.1016/j.compositesa.2017.11.006.

[103] P. Fazzino and K. Reifsnider. "Electrochemical Impedance Spectroscopy Detection of Damage in Out of Plane Fatigued Fiber Reinforced Composite Materials". In: *Applied Composite Materials* 15.3 (2008), pp. 127–138. ISSN: 0929-189X. DOI: 10.1007/s10443-008-9062-6.

[104] P. D. Fazzino, K. L. Reifsnider, and P. Majumdar. “Impedance spectroscopy for progressive damage analysis in woven composites”. In: *Composites Science and Technology* 69.11-12 (2009), pp. 2008–2014. ISSN: 0266-3538. DOI: 10.1016/j.compscitech.2009.05.007.

[105] L. Lampani, F. Sarasini, J. Tirillò, and P. Gaudenzi. “Analysis of damage in composite laminates with embedded piezoelectric patches subjected to bending action”. In: *Composite Structures* 202 (2018), pp. 935–942. ISSN: 02638223. DOI: 10.1016/j.compstruct.2018.04.073.

[106] C. Tuloup, W. Harizi, Z. Aboura, and Y. Meyer. “Integration of piezoelectric transducers (PZT and PVDF) within polymer-matrix composites for structural health monitoring applications: new success and challenges”. In: *International Journal of Smart and Nano Materials* (2020), pp. 1–27. ISSN: 1947-5411. DOI: 10.1080/19475411.2020.1830196.

[107] I. M. de Rosa and F. Sarasini. “Use of PVDF as acoustic emission sensor for in situ monitoring of mechanical behaviour of glass/epoxy laminates”. In: *Polymer Testing* 29.6 (2010), pp. 749–758. ISSN: 01429418. DOI: 10.1016/j.polymertesting.2010.04.006.

[108] S. Masmoudi, A. El Mahi, R. El Guerjouma, and S. Turki. “Mechanical behaviour and identification of damage by acoustic emission of smart composites”. In: *Multidiscipline Modeling in Materials and Structures* 10.1 (2014), pp. 2–17. ISSN: 1573-6105. DOI: 10.1108/MMMS-11-2012-0023.

[109] H. P. Konka. “Embedded Piezoelectric Fiber Composite Sensors for Applications in Composite Structures”. Dissertation. Louisiana: Louisiana State University, 2011.

[110] N. A. Chrysochoidis and E. Gutiérrez. “Evaluation of the sensitivity and fatigue performance of embedded piezopolymer sensor systems in sandwich composite laminates”. In: *Smart Materials and Structures* 24.2 (2015), p. 025032. DOI: 10.1088/0964-1726/24/2/025032.

[111] C. Tuloup, W. Harizi, Z. Aboura, Y. Meyer, K. Khellil, and R. Lachat. “On the use of in-situ piezoelectric sensors for the manufacturing and structural health monitoring of polymer-matrix composites: A literature review”. In: *Composite Structures* 215 (2019), pp. 127–149. ISSN: 02638223. DOI: 10.1016/j.compstruct.2019.02.046.

[112] M. Salas, M. Hübner, M. Borysov, M. Koerdt, M. Rennoch, A. S. Herrmann, and W. Lang. "Measuring Material Moisture in Fiber Reinforced Polymers by Integrated Sensors". In: *IEEE Sensors Journal* 18.9 (2018), pp. 3836–3843. ISSN: 1558-1748. DOI: 10.1109/JSEN.2018.2815029.

[113] M. Loos. *Carbon nanotube reinforced composites: CNR polymer science and technology*. First edition. Plastics Design Library. Oxford, England and Waltham, Massachusetts: Elsevier, 2015. ISBN: 9781455731961.

[114] I. Balberg, C. H. Anderson, S. Alexander, and N. Wagner. "Excluded volume and its relation to the onset of percolation". In: *Physical Review B* 30.7 (1984), pp. 3933–3943. ISSN: 1098-0121. DOI: 10.1103/PhysRevB.30.3933.

[115] B. Fiedler, F. H. Gojny, M. H. G. Wichmann, M. C. M. Nolte, and K. Schulte. "Fundamental aspects of nano-reinforced composites". In: *Composites Science and Technology* 66.16 (2006), pp. 3115–3125. ISSN: 0266-3538. DOI: 10.1016/j.compscitech.2005.01.014.

[116] H. Meeuw, C. Viets, W. V. Liebig, K. Schulte, and B. Fiedler. "Morphological influence of carbon nanofillers on the piezoresistive response of carbon nanoparticle/epoxy composites under mechanical load". In: *European Polymer Journal* 85.21 (2016), pp. 198–210. ISSN: 00143057. DOI: 10.1016/j.eurpolymj.2016.10.027.

[117] S. Iijima. "Helical microtubules of graphitic carbon". In: *Nature* 354.6348 (1991), pp. 56–58. ISSN: 0028-0836. DOI: 10.1038/354056a0.

[118] H. Dai, J. Kong, C. Zhou, N. Franklin, T. Tombler, A. Cassell, S. Fan, and M. Chapline. "Controlled Chemical Routes to Nanotube Architectures, Physics, and Devices". In: *The Journal of Physical Chemistry B* 103.51 (1999), pp. 11246–11255. ISSN: 1520-6106. DOI: 10.1021/jp992328o.

[119] H. Dai. "Carbon nanotubes: opportunities and challenges". In: *Surface Science* 500.1-3 (2002), pp. 218–241. ISSN: 00396028. DOI: 10.1016/S0039-6028(01)01558-8.

[120] H. Dai. "Carbon nanotubes: synthesis, integration, and properties". In: *Accounts of chemical research* 35.12 (2002), pp. 1035–1044. ISSN: 0001-4842. DOI: 10.1021/ar0101640.

[121] M. S. Dresselhaus, G. Dresselhaus, and P. C. Eklund. "C60-Related Tubules and Spherules". In: *Science of fullerenes and carbon nanotubes*. Ed. by M. S. Dresselhaus. San Diego: Academic Press, 1996, pp. 756–869. ISBN: 9780122218200. DOI: 10.1016/B978-012221820-0/50019-8.

[122] R. Saito, M. Fujita, G. Dresselhaus, and M. S. Dresselhaus. "Electronic structure of chiral graphene tubules". In: *Applied Physics Letters* 60.18 (1992), pp. 2204–2206. ISSN: 0003-6951. DOI: 10.1063/1.107080.

[123] S. J. Tans, M. H. Devoret, H. Dai, A. Thess, R. E. Smalley, L. J. Geerligs, and C. Dekker. "Individual single-wall carbon nanotubes as quantum wires". In: *Nature* 386.6624 (1997), pp. 474–477. ISSN: 0028-0836. DOI: 10.1038/386474a0.

[124] T. W. Odom, J.-L. Huang, P. Kim, and C. M. Lieber. "Atomic structure and electronic properties of single-walled carbon nanotubes". In: *Nature* 391.6662 (1998), pp. 62–64. ISSN: 0028-0836. DOI: 10.1038/34145.

[125] J. W. G. Wilder, L. C. Venema, A. G. Rinzler, R. E. Smalley, and C. Dekker. "Electronic structure of atomically resolved carbon nanotubes". In: *Nature* 391.6662 (1998), pp. 59–62. ISSN: 0028-0836. DOI: 10.1038/34139.

[126] H. Hiura, T. W. Ebbesen, J. Fujita, K. Tanigaki, and T. Takada. "Role of sp3 defect structures in graphite and carbon nanotubes". In: *Nature* 367.6459 (1994), pp. 148–151. ISSN: 0028-0836. DOI: 10.1038/367148a0.

[127] H. Dai, E. W. Wong, and C. M. Lieber. "Probing Electrical Transport in Nanomaterials: Conductivity of Individual Carbon Nanotubes". In: *Science* 272.5261 (1996), pp. 523–526. DOI: 10.1126/science.272.5261.523.

[128] C. Li, E. T. Thostenson, and T.-W. Chou. "Effect of nanotube waviness on the electrical conductivity of carbon nanotube-based composites". In: *Composites Science and Technology* 68.6 (2008), pp. 1445–1452. ISSN: 0266-3538. DOI: 10.1016/j.compscitech.2007.10.056.

[129] D. Stauffer and A. Aharony. *Introduction To Percolation Theory*. Taylor & Francis, 2018. ISBN: 9781482272376. DOI: 10.1201/9781315274386.

[130] Alamusi, N. Hu, H. Fukunaga, S. Atobe, Y. Liu, and J. Li. "Piezoresistive strain sensors made from carbon nanotubes based polymer nanocomposites". In: *Sensors (Basel, Switzerland)* 11.11 (2011), pp. 10691–10723. DOI: 10.3390/s111110691.

[131] B. E. Kilbride, J. N. Coleman, J. Fraysse, P. Fournet, M. Cadek, A. Drury, S. Hutzler, S. Roth, and W. J. Blau. "Experimental observation of scaling laws for alternating current and direct current conductivity in polymer-carbon nanotube composite thin films". In: *Journal of Applied Physics* 92.7 (2002), pp. 4024–4030. ISSN: 0021-8979. DOI: 10.1063/1.1506397.

[132] M. H. G. Wichmann, J. Sumfleth, F. H. Gojny, M. Quaresimin, B. Fiedler, and K. Schulte. "Glass-fibre-reinforced composites with enhanced mechanical and electrical properties – Benefits and limitations of a nanoparticle modified matrix". In: *Engineering Fracture Mechanics* 73.16 (2006), pp. 2346–2359. ISSN: 0013-7944. DOI: 10.1016/j.engfracmech.2006.05.015.

[133] J.-M. Park, D.-S. Kim, S.-J. Kim, P.-G. Kim, D.-J. Yoon, and K. L. DeVries. "Inherent sensing and interfacial evaluation of carbon nanofiber and nanotube/epoxy composites using electrical resistance measurement and micromechanical technique". In: *Composites Part B: Engineering* 38.7-8 (2007), pp. 847–861. ISSN: 13598368. DOI: 10.1016/j.compositesb.2006.12.004.

[134] F. Nanni, G. Ruscito, D. Puglia, A. Terenzi, J. M. Kenny, and G. Gusmano. "Effect of carbon black nanoparticle intrinsic properties on the self-monitoring performance of glass fibre reinforced composite rods". In: *Composites Science and Technology* 71.1 (2011), pp. 1–8. ISSN: 0266-3538. DOI: 10.1016/j.compscitech.2010.08.015.

[135] A. Celzard, E. McRae, C. Deleuze, M. Dufort, G. Furdin, and J. F. Marêché. "Critical concentration in percolating systems containing a high-aspect-ratio filler". In: *Physical review. B, Condensed matter* 53.10 (1996), pp. 6209–6214. ISSN: 0163-1829. DOI: 10.1103/physrevb.53.6209.

[136] J. K. W. Sandler, J. E. Kirk, I. A. Kinloch, M. S. P. Shaffer, and A. H. Windle. "Ultra-low electrical percolation threshold in carbon-nanotube-epoxy composites". In: *Polymer* 44.19 (2003), pp. 5893–5899. ISSN: 00323861. DOI: 10.1016/S0032-3861(03)00539-1.

[137] M. B. Bryning, M. F. Islam, J. M. Kikkawa, and A. G. Yodh. "Very Low Conductivity Threshold in Bulk Isotropic Single-Walled Carbon Nanotube-Epoxy Composites". In: *Advanced Materials* 17.9 (2005), pp. 1186–1191. ISSN: 09359648. DOI: 10.1002/adma.200401649.

[138] J. Z. Kovacs, B. S. Velagala, K. Schulte, and W. Bauhofer. "Two percolation thresholds in carbon nanotube epoxy composites". In: *Composites Science and Technology* 67.5 (2007), pp. 922–928. ISSN: 0266-3538. DOI: 10.1016/j.compscitech.2006.02.037.

[139] J. N. Israelachvili. "Solvation, Structural, and Hydration Forces". In: *Intermolecular and Surface Forces*. Ed. by J. N. Israelachvili. Saint Louis: Elsevier Science, 2015, pp. 341–380. ISBN: 9780123751829. DOI: 10.1016/B978-0-12-375182-9.10015-6.

[140] W. B. Russel, D. A. Saville, and W. R. Schowalter. *Colloidal Dispersions*. Cambridge University Press, 2012. ISBN: 9780521426008. DOI: 10.1017/CBO9780511608810.

[141] J. Z. Kovacs, R. E. Mandjarov, T. Blisnjuk, K. Prehn, M. Sussiek, J. Müller, K. Schulte, and W. Bauhofer. "On the influence of nanotube properties, processing conditions and shear forces on the electrical conductivity of carbon nanotube epoxy composites". In: *Nanotechnology* 20.15 (2009), p. 155703. DOI: 10.1088/0957-4484/20/15/155703.

[142] R. J. Hunt and W. P. Johnson. "Pathogen transport in groundwater systems: contrasts with traditional solute transport". In: *Hydrogeology Journal* 25.4 (2017), pp. 921–930. ISSN: 1431-2174. DOI: 10.1007/s10040-016-1502-z.

[143] J. Sandler, M. S. P. Shaffer, T. Prasse, W. Bauhofer, K. Schulte, and A. H. Windle. "Development of a dispersion process for carbon nanotubes in an epoxy matrix and the resulting electrical properties". In: *Polymer* 40.21 (1999), pp. 5967–5971. ISSN: 00323861. DOI: 10.1016/S0032-3861(99)00166-4.

[144] Y.-H. Liao, O. Marietta-Tondin, Z. Liang, C. Zhang, and B. Wang. "Investigation of the dispersion process of SWNTs/SC-15 epoxy resin nanocomposites". In: *Materials Science and Engineering: A* 385.1-2 (2004), pp. 175–181. ISSN: 09215093. DOI: 10.1016/j.msea.2004.06.031.

[145] H. Meeuw, J. Körbelin, D. von Bernstorff, T. Augustin, W. V. Liebig, and B. Fiedler. "Smart dispersion: Validation of OCT and impedance spectroscopy as solutions for in-situ dispersion analysis of CNP/EP-composites". In: *Materialia* 1.9 (2018), pp. 185–197. ISSN: 25891529. DOI: 10.1016/j.mtla.2018.06.002.

[146] J. C. Fisher and I. Giaever. "Tunneling Through Thin Insulating Layers". In: *Journal of Applied Physics* 32.2 (1961), pp. 172–177. ISSN: 0021-8979. DOI: 10.1063/1.1735973.

[147] J. G. Simmons. "Generalized Formula for the Electric Tunnel Effect between Similar Electrodes Separated by a Thin Insulating Film". In: *Journal of Applied Physics* 34.6 (1963), pp. 1793–1803. ISSN: 0021-8979. DOI: 10.1063/1.1702682.

[148] J. G. Simmons. "Low–Voltage Current–Voltage Relationship of Tunnel Junctions". In: *Journal of Applied Physics* 34.1 (1963), pp. 238–239. ISSN: 0021-8979. DOI: 10.1063/1.1729081.

[149] J. G. Simmons and G. J. Unterkofler. "Potential Barrier Shape Determination in Tunnel Junctions". In: *Journal of Applied Physics* 34.6 (1963), pp. 1828–1830. ISSN: 0021-8979. DOI: 10.1063/1.1702693.

[150] J. G. Simmons. "Electric Tunnel Effect between Dissimilar Electrodes Separated by a Thin Insulating Film". In: *Journal of Applied Physics* 34.9 (1963), pp. 2581–2590. ISSN: 0021-8979. DOI: 10.1063/1.1729774.

[151] C. Li, E. T. Thostenson, and T.-W. Chou. "Dominant role of tunneling resistance in the electrical conductivity of carbon nanotube–based composites". In: *Applied Physics Letters* 91.22 (2007), p. 223114. ISSN: 0003-6951. DOI: 10.1063/1.2819690.

[152] Y. Yu, G. Song, and L. Sun. "Determinant role of tunneling resistance in electrical conductivity of polymer composites reinforced by well dispersed carbon nanotubes". In: *Journal of Applied Physics* 108.8 (2010), p. 084319. ISSN: 0021-8979. DOI: 10.1063/1.3499628.

[153] F. Du, C. Guthy, T. Kashiwagi, J. E. Fischer, and K. I. Winey. "An infiltration method for preparing single-wall nanotube/epoxy composites with improved thermal conductivity". In: *Journal of Polymer Science Part B: Polymer Physics* 44.10 (2006), pp. 1513–1519. ISSN: 0887-6266. DOI: 10.1002/polb.20801.

[154] J. Li, P. C. Ma, W. S. Chow, C. K. To, B. Z. Tang, and J.-K. Kim. "Correlations between Percolation Threshold, Dispersion State, and Aspect Ratio of Carbon Nanotubes". In: *Advanced Functional Materials* 17.16 (2007), pp. 3207–3215. ISSN: 1616301X. DOI: 10.1002/adfm.200700065.

[155] G. D. Seidel and D. C. Lagoudas. "A Micromechanics Model for the Electrical Conductivity of Nanotube-Polymer Nanocomposites". In: *Journal of Composite Materials* 43.9 (2009), pp. 917–941. DOI: 10.1177/0021998308105124.

[156] M. Park, H. Kim, and J. P. Youngblood. "Strain-dependent electrical resistance of multi-walled carbon nanotube/polymer composite films". In: *Nanotechnology* 19.5 (2008), p. 055705. DOI: 10.1088/0957-4484/19/05/055705.

[157] G. T. Pham. "Characterization And Modeling Of Piezo-Resistive Properties Of Carbon Nanotube-Based Conductive Polymer Composites". PhD thesis. Florida State University, 2008. URL: http://purl.flvc.org/fsu/fd/FSU_migr_etd-1965 (visited on 02/01/2022).

[158] W. Obitayo and T. Liu. "A Review: Carbon Nanotube-Based Piezoresistive Strain Sensors". In: *Journal of Sensors* 2012 (2012), pp. 1–15. ISSN: 1687-725X. DOI: 10.1155/2012/652438.

[159] N. Hu, Y. Karube, C. Yan, Z. Masuda, and H. Fukunaga. "Tunneling effect in a polymer/carbon nanotube nanocomposite strain sensor". In: *Acta Materialia* 56.13 (2008), pp. 2929–2936. ISSN: 13596454. DOI: 10.1016/j.actamat.2008.02.030.

[160] M. H. G. Wichmann, S. T. Buschhorn, J. Gehrmann, and K. Schulte. "Piezoresistive response of epoxy composites with carbon nanoparticles under tensile load". In: *Physical Review B* 80.24 (2009), p. 667. ISSN: 1098-0121. DOI: 10.1103/PhysRevB.80.245437.

[161] K. J. Loh, J. P. Lynch, B. S. Shim, and N. A. Kotov. "Tailoring Piezoresistive Sensitivity of Multilayer Carbon Nanotube Composite Strain Sensors". In: *Journal of Intelligent Material Systems and Structures* 19.7 (2008), pp. 747–764. ISSN: 1045-389X. DOI: 10.1177/1045389X07079872.

[162] T. C. Theodosiou and D. A. Saravanos. "Numerical investigation of mechanisms affecting the piezoresistive properties of CNT-doped polymers using multi-scale models". In: *Composites Science and Technology* 70.9

(2010), pp. 1312–1320. ISSN: 0266-3538. DOI: 10.1016/j.compscitech.2010.04.003.

[163] Z. Wang and X. Ye. "An investigation on piezoresistive behavior of carbon nanotube/polymer composites: II. Positive piezoresistive effect". In: *Nanotechnology* 25.28 (2014), p. 285502. DOI: 10.1088/0957-4484/25/28/285502.

[164] F. Panozzo, M. Zappalorto, and M. Quaresimin. "Analytical model for the prediction of the piezoresistive behavior of CNT modified polymers". In: *Composites Part B: Engineering* 109 (2017), pp. 53–63. ISSN: 13598368. DOI: 10.1016/j.compositesb.2016.10.034.

[165] C. Li and T.-W. Chou. "Modeling of damage sensing in fiber composites using carbon nanotube networks". In: *Composites Science and Technology* 68.15-16 (2008), pp. 3373–3379. ISSN: 0266-3538. DOI: 10.1016/j.compscitech.2008.09.025.

[166] N. Hu, Y. Karube, M. Arai, T. Watanabe, C. Yan, Y. Li, Y. Liu, and H. Fukunaga. "Investigation on sensitivity of a polymer/carbon nanotube composite strain sensor". In: *Carbon* 48.3 (2010), pp. 680–687. ISSN: 00086223. DOI: 10.1016/j.carbon.2009.10.012.

[167] F. Avilés, A. I. Oliva-Avilés, and M. Cen-Puc. "Piezoresistivity, Strain, and Damage Self-Sensing of Polymer Composites Filled with Carbon Nanostructures". In: *Advanced Engineering Materials* 20.7 (2018), p. 1701159. ISSN: 14381656. DOI: 10.1002/adem.201701159.

[168] K. Ke. "Piezoresistive Behavior of Carbon Nanotube based Poly(vinylidene fluoride) Nanocomposites towards Strain Sensing Applications". Dissertation. Dresden: Technischen Universität Dresden, 2016.

[169] A. I. Oliva-Avilés, F. Avilés, and V. Sosa. "Electrical and piezoresistive properties of multi-walled carbon nanotube/polymer composite films aligned by an electric field". In: *Carbon* 49.9 (2011), pp. 2989–2997. ISSN: 00086223. DOI: 10.1016/j.carbon.2011.03.017.

[170] B. Fiedler and K. Schulte. "6.8 Carbon Nanotube-Based Composites". In: *Comprehensive composite materials II*. Ed. by C. H. Zweben and P. W. R. Beaumont. Amsterdam, Netherlands: Elsevier, 2018, pp. 201–229. ISBN: 9780081005347. DOI: 10.1016/B978-0-12-803581-8.10012-8.

[171] DIN EN ISO 527-4. *Plastics - Determination of tensile properties - Part 4: Test conditions for isotropic and anisotropic fibre-reinforced plastic composites*. 1997.

[172] DIN EN ISO 14125. *Fibre-reinforced plastic composites - Determination of flexural properties*. 2011.

[173] ASTM D3410. *Standard Test Method for Compressive Properties of Polymer Matrix Composite Materials with Unsupported Gage Section by Shear Loading*. West Conshohocken, PA.

[174] ASTM D2344 / D2344M-16. *Test Method for Short-Beam Strength of Polymer Matrix Composite Materials and Their Laminates*. West Conshohocken, PA, 2016. DOI: 10.1520/D2344_D2344M-16.

[175] ASTM D5766/ D5766M-11. *Test Method for Open-Hole Tensile Strength of Polymer Matrix Composite Laminates*. West Conshohocken, PA, 2018. DOI: 10.1520/D5766_D5766M-11R18.

[176] H. Meeuw, V. K. Wisniewski, U. Köpke, A. S. Nia, A. R. Vázquez, M. R. Lohe, X. Feng, and B. Fiedler. "In-line monitoring of carbon nanoparticle epoxy dispersion processes". In: *Production Engineering* 13.3-4 (2019), pp. 373–390. ISSN: 0944-6524. DOI: 10.1007/s11740-019-00884-5.

[177] G. R. Higson. "Recent advances in strain gauges". In: *Journal of Scientific Instruments* 41.7 (1964), p. 405. ISSN: 0950-7671. DOI: 10.1088/0950-7671/41/7/301.

[178] G. Yin, N. Hu, Y. Karube, Y. Liu, Y. Li, and H. Fukunaga. "A carbon nanotube/polymer strain sensor with linear and anti-symmetric piezoresistivity". In: *Journal of Composite Materials* 45.12 (2011), pp. 1315–1323. DOI: 10.1177/0021998310393296.

[179] S. M. Vemuru, R. Wahi, S. Nagarajaiah, and P. M. Ajayan. "Strain sensing using a multiwalled carbon nanotube film". In: *The Journal of Strain Analysis for Engineering Design* 44.7 (2009), pp. 555–562. ISSN: 0309-3247. DOI: 10.1243/03093247JSA535.

[180] M. D. Rein, O. Breuer, and H. D. Wagner. "Sensors and sensitivity: Carbon nanotube buckypaper films as strain sensing devices". In: *Composites Science and Technology* 71.3 (2011), pp. 373–381. ISSN: 0266-3538. DOI: 10.1016/j.compscitech.2010.12.008.

[181] L. P. Mortensen, D. H. Ryu, Y. J. Zhao, and K. J. Loh. "Rapid Assembly of Multifunctional Thin Film Sensors for Wind Turbine Blade Monitoring". In: *Key Engineering Materials* 569-570 (2013), pp. 515–522. DOI: 10.4028/www.scientific.net/KEM.569-570.515.

[182] A. R. Santos, L. Amorim, J. P. Nunes, A. F. Silva, and J. C. Viana. "Aligned Carbon Nanotube-Based Sensors for Strain Monitoring of Composites". In: *IEEE Sensors Journal* 21.13 (2021), pp. 14718–14725. ISSN: 1558-1748. DOI: 10.1109/JSEN.2021.3070927.

[183] J. R. Bautista-Quijano, F. Avilés, J. O. Aguilar, and A. Tapia. "Strain sensing capabilities of a piezoresistive MWCNT-polysulfone film". In: *Sensors and Actuators A: Physical* 159.2 (2010), pp. 135–140. ISSN: 0924-4247. DOI: 10.1016/j.sna.2010.03.005.

[184] R. Zoughi and B. Zonnefeld. "Permittivity Characteristics of Kevlar, Carbon Composites, E-Glass, and Rubber (33% Carbon) at X-Band (8–12 GHZ)". In: *Review of Progress in Quantitative Nondestructive Evaluation: Volume 10B*. Ed. by Donald O. Thompson and Dale E. Chimenti. Boston, MA: Springer US, 1991, pp. 1431–1436. ISBN: 978-1-4615-3742-7. DOI: 10.1007/978-1-4615-3742-7_38.

[185] V. I. Sokolov, S. I. Shalgunov, I. G. Gurtovnik, L. G. Mikheeva, and I. D. Simonov-Emelyanov. "Dielectric Characteristics of Glass Fibre Reinforced Plastics and Their Components". In: *International Polymer Science and Technology* 32.7 (2005), pp. 62–67. DOI: 10.1177/0307174X0503200715.

[186] Y. Wang and D.D.L. Chung. "Effect of the fringing electric field on the apparent electric permittivity of cement-based materials". In: *Composites Part B: Engineering* 126 (2017), pp. 192–201. ISSN: 13598368. DOI: 10.1016/j.compositesb.2017.05.080.

[187] A. M. Maffezzoli, L. Peterson, J. C. Seferis, J. Kenny, and L. Nicolais. "Dielectric characterization of water sorption in epoxy resin matrices". In: *Polymer Engineering and Science* 33.2 (1993), pp. 75–82. ISSN: 0032-3888. DOI: 10.1002/pen.760330204.

[188] A. Fukuda, H. Mitsui, Y. Inoue, and K. Goto. "The influence of water absorption on dielectric properties of cycloaliphatic epoxy resin". In: *Proceedings of 5th International Conference on Properties and Applications*

of Dielectric Materials. 1997, 58–61 vol.1. DOI: 10.1109/ICPADM.1997.617527.

[189] A. N. Fraga, E. Frullloni, O. de La Osa, J. M. Kenny, and A. Vázquez. "Relationship between Water Absorption and Dielectric Behavior of Glass Fiber Reinforced Unsaturated Polyester Resin". In: *Journal of Composite Materials* 41.4 (2007), pp. 393–402. DOI: 10.1177/0021998306063789.

[190] Y. Shimamura, T. Urabe, A. Todoroki, and H. Kobayashi. "Electrical impedance change method for moisture absorption monitoring of CFRP". In: *Advanced Composite Materials* 13.3-4 (2004), pp. 297–310. ISSN: 0924-3046. DOI: 10.1163/1568551042580145.